

# Biomass burning events measured by lidars in EARLINET. Part I. Data analysis methodology.

Mariana Adam<sup>1</sup>, Doina Nicolae<sup>1</sup>, Iwona S. Stachlewska<sup>2</sup>, Alexandros Papayannis<sup>3</sup>, Dimitris Balis<sup>4</sup>

<sup>1</sup>National Institute for R&D in Optoelectronics, Magurele, 077225, Romania

<sup>2</sup>Institute of Geophysics, [Faculty of Physics](#), University of Warsaw, 02093, Poland

<sup>3</sup>National Technical University of Athens, Department of Physics, Athens, 15780, Greece

<sup>4</sup>Laboratory of Atmospheric Physics, Aristotle University of Thessaloniki, Thessaloniki, 54124, Greece

*Correspondence to:* Mariana Adam ([mariana.adam@inoe.ro](mailto:mariana.adam@inoe.ro))

**Abstract.** The methodology of analysing the biomass burning events recorded in the database of the European Aerosol Research Lidar Network in the frame of Aerosol Cloud and Trace Gases Research Infrastructure is presented. The period of 2008-2017 was chosen to analyse all of the events stored in the database under Forest Fire category for a number of 14 stations available. The data provided ranged from complete data sets (particle backscatter, extinction and linear depolarization ratio profiles) to single profiles (particle backscatter coefficient profile). Smoke layers geometry was evaluated and the mean optical properties within each layer were computed. The backtrajectories technique was used to double check the source of all pollution layers. The biomass burning layers were identified taking into account the presence of the fires along the backtrajectory. The biomass burning events are analysed by the means of the intensive parameters. The analysis was structured in three directions: I) common biomass burning source (fire) recorded by at least two stations, II) long-range transport from [NNorth](#) America, III) analysis over four geographical regions (SE Europe, NE Europe, Central Europe and SW Europe). Based on backtrajectories calculations and fires' location, the lidar measurements can be labelled either as measurements of 'single fire' or 'mixed fires' (case I), measurements of [NNorth](#) America fires or measurements of mixed [NNorth](#) America and local fires (case II). The histogram of the fires' location reveals the smoke sources for each region. For each region, statistics on intensive parameters is performed. The sources' origin of the intensive parameters is categorized based on the continental origin of the air-mass (European, African, Asian, [NNorth](#) American or a combination of them). The methodology presented here is meant to provide a perspective to explore large amount of lidar data and deliver novel approaches to analyse the intensive parameters based on the assigned biomass burning sources. A thorough consideration of all potential fires' sources reveals that most of the time the lidar measurements characterise the smoke from a mixture of fires. A comprehensive discussion over all results (based on the intensive parameters and the sources' location), will be given in a companion paper submitted to ACP EARLINET special issue.

## 1 Introduction

Biomass burning (BB) represents one of the major sources of atmospheric particles (aerosols). The sources of BB are both natural (wild fires) and anthropogenic (controlled fires). The direct effect on radiative transfer can be both negative and positive as a consequence of the opposite effects of the two main components: black carbon (absorption, positive effect) and organic carbon (scattering, negative effect) (Fiebig et al, 2002; Bond et al., 2013; Myhre et al., 2013) with a general radiative forcing close to zero ([https://www.ipcc.ch/site/assets/uploads/2018/02/WG1AR5\\_Chapter08\\_FINAL.pdf](https://www.ipcc.ch/site/assets/uploads/2018/02/WG1AR5_Chapter08_FINAL.pdf), IPCC, 2013, last access 20200203).

As indirect effect, BB can act as cloud condensation nuclei (e.g. Yu, 2000) or ice nuclei (e.g. Prenni et al, 2012). At ground level or within the Planetary Boundary Layer (PBL), strong pollution events produce a large reduction of the visibility over various regions (e.g. Adam et al., 2004), which can affect the traffic and more importantly can cause serious

10 health issues for humans (e.g. Pahlow et al., 2005; Sapkota et al., 2005, Alonso-Blanco et al., 2018). Numerous wild forest fires events occur each year in Europe (refer to annual reports from European Commission on “Forest Fires in Europe, Middle

15 East and North Africa YYYY” at <http://effis.jrc.ec.europa.eu/reports-and-publications/annual-fire-reports/> available since 2000, where YYYY represents the year; last access 20191126). Therein, the studies report the impact of forest fires in Europe,

providing the number of fires and burnt area by country. The 2017 report (San-Miguel-Ayanz et al, 2018) shows that the

15 number of fires was higher as compared with the average over 2000-2017 period while the burnt area was even larger, especially for Portugal. For the Southern States (Portugal, Spain, France, Italy and Greece), most effected by fires, the highest

number of fires occurred in Portugal (44%) and Spain (29%) while the largest burn area occurred in Portugal (59%) and then Spain (19%) and Italy (18%). As mentioned in the report, climate change affects forest fires through the weather conditions,

and through its effects on vegetation and fuel (combustible material). Besides the European fires which can act locally or

20 through short range transport within continent, Europe is also affected by long range transport, the most common being the smoke transported from Russia or even from North America (aged smoke). Note that over Poland the BB is the most important

source of long range transported particles even in boundary layer (e.g. Wang et al., 2019). In a recent study by Nicolae et al. (2019) it was shown that the smoke is the most predominant aerosol type in Europe for long-range transport, as revealed by

25 lidar measurements over 2008-2018 period over 17 stations equipped with multiwavelength lidars. The inventory of fires is provided by European Commission through EFFIS (European Forest Fire Information System) at European level and by NASA

through FIRMS (Fire Information for Resource Management System) at global level (<https://firms.modaps.eosdis.nasa.gov/>, last access 20191126) (Davies et al., 2009). Both databases are based on MODIS (Moderate Resolution Imaging

Spectroradiometer) satellite data.

Lidars provide measurements of the smoke aerosol being able to deliver the boundaries of the smoke layers as well as the

30 optical properties of the smoke aerosol in the layers. Both layers geometry and optical properties can be used as a validation of the transport models (e.g. van Drooge et al., 2016). For a detailed analysis of the data requirements by models, see Benedetti et al., 2018 and references herein. Referring to BB aerosol, the study mentions the usefulness of lidar retrieval of the plume

height. Layer geometry can also be used to constrain specific satellite profiles retrievals which, as known, have less sensitivity

towards the ground (e.g. Bond et al., 2013). The optical properties can be used (closure studies) to model the microphysical properties of the aerosol (e.g. Fiebig et al., 2002; Fiebig et al., 2003). Regarding the impact of BB aerosol on weather forecast, the study by Zhang et al. (2016) suggests that the BB' effect is seen for AOD (aerosol optical depth) at 550nm larger than 1. Ultimately the researchers try to establish the BB effect on the radiative forcing (e.g. Fiebig et al., 2002; Lolli et al., 2019; 5 Markowicz et al., 2016).

Within these applications, the EARLINET (European Aerosol Research Lidar Network) can provide spatial and temporal coverage of the BB transport over Europe. EARLINET is part of Aerosol Cloud and Trace Gases Research Infrastructure (ACTRIS) (<http://actris.nilu.no/>, last access 20191126), which provides ground-based, insitu or remote sensing. EARLINET provides measurements of the biomass burning aerosol with first lidar profiles dating from 2002. More systematic 10 measurements over the network can be seen after 2012 (closely related with the increase of the number of stations in the network). A review of the lidar studies over BB will be given at a later stage in this paper.

The current study envisages the research on the biomass burning aerosol as measured by 14 stations in EARLINET over the period 2008-2017. This paper presents the methodology of data analysis, whereas a companion paper (submitted to ACP, EARLINET special issue) focuses in detail on the discussion of the outcome. The EARLINET is shortly presented in Section 15 2. In Section 3 we briefly discuss the extra undertaken data quality checks. Data analyses follows in Section 4. The data interpretation (Section 5) is based on aerosol intensive parameters (lidar ratio - LR, extinction Ångström exponent - EAE, backscatter Ångström exponent - BAE, linear particle depolarization ratio - PDR). Examples are given for the following research directions: I) fires events (same source) as observed by two lidar systems, II) long range transport (LRT) from ~~North~~ America, III) study based on four geographical measurements regions including the histogram of the fire sources locations for 20 each region. Summary and conclusions follow in Section 6. A short introduction to the present methodology was given at ILRC29 (Adam et al., 2019). [A list of acronyms used in the current work is given in the Supplement \(Table S1\).](#)

## 2 EARLINET database

The EARLINET database consists currently (October 2019) of 30 lidar stations covering most of Europe and one location outside Europe (Dushanbe, Tajikistan). There are three other non-permanent stations as well as six newly joining stations. 25 Twelve stations are not active (<https://www.earlinet.org/index.php?id=105>, last access 20191126). A review of the EARLINET network is given by Pappalardo et al. (2014). The data submitted to the database belongs to one or more of the following categories: climatology (measurements taken at specific times on Mondays and Thursdays), Calipso (measurements taken during Calipso overpasses), Saharan dust (measurements taken during Saharan dust intrusions), volcanic eruptions (measurements taken during volcanic eruptions), forest fires (measurements taken during forest fires events), diurnal cycles 30 (measurements taken continuously over the whole day), Cirrus (measurements of Cirrus clouds), photosmog (measurements during photosmog episodes), rural/urban (measurements taken under rural or urban environments) and stratosphere (measurements at stratospheric levels). Most of the measurements are taken under Climatology category followed by Calipso

and Saharan dust categories (Pappalardo et al. 2014). The largest data set regarding the optical properties was submitted by each station following its own retrieval procedure. Note that while Climatology and Calipso measurements are mandatory in the network, all the other categories are built based on voluntary bases. Currently it is envisaged the use of Single Calculus Chain (SCC) developed in EARLINET for all raw data submitted by each station (see D'Amico et al, 2015; D'Amico et al, 5 2016; Mattis et al, 2016). There are two types of files submitted to the database for the optical properties: b-files (containing particles backscatter coefficient) and e-files (containing particles extinction coefficient and sometimes particles backscatter coefficient retrieved using both elastic and Raman channel). Other variables may be reported as well (see Pappalardo et al., 2014). For systems with depolarization capability, the retrieval of the particles linear depolarization ratio (PDR) is recorded in b-files except Warsaw (“wa”), which records it in both b-files and e-files.

## 10 2.1 EARLINET Forest Fire category

For the present study, the data submitted under Forest Fire (FF) category was considered. Over the period 2008-2017 (when most of the data was submitted), a number of 3759 b-files and e-files were available at 20 stations corresponding to the emission wavelengths 355, 532 and 1064 nm. Another 256 files were submitted at different emission wavelengths (313, 351, 510 and 694 nm). In addition, the Hysplit (Hybrid Single-Particle Lagrangian Integrated Trajectory model) model was available since 15 September 2007 (Stein et al., 2015; Rolph et al., 2017). Hysplit model is used to double check the origin of the aerosols from various layers (as discussed later on). We also considered only the data whose emission wavelength was at 355, 532 and 1064 nm as these are the most used in the lidar community and allows the direct intercomparing of the optical properties. After preliminary quality control checks (discussed in chapter 3), 14 stations were selected over 2008-2017 period, delivering 2341 files (~ 650 % of total), quality checked. The geographical location of the stations is shown in Fig. 1. Also shown, the four 20 geographical regions analysed separately further on (section 5.3). An overview over the number of stations reporting data for FF category as compared with their total number of files submitted (as for March 2018), reveal that the following. FF category represented ~ 40% of the total measurements for Thessaloniki, Athens and Warsaw, ~ 20 % for Minsk and ~ 10% for Bucharest and Granada.

Several stations (Athens, Barcelona, Bucharest, Potenza, Observatory Hohenpeissenberg, Thessaloniki, Warsaw“at”, “ba”, 25 “bu”, “le”, “po”, “oh”, “th”, “wa”) were committed to send either reprocessed data or to process additional data using SCC, which were not yet included yet in EARLINET (most of them for 2017) as for March 2018. Currently (20200625) all the data are uploaded in Earlinet database. Within these circumstances, the number of files increased to 3589 (QC for 2341 files already on EARLINET database). The diagram of the methodology is shown in Fig. 2. Following I<sup>st</sup> step in methodology (Fig. 2), the number of input files (b-files and e-files) for each station is shown in Fig. 3 and Table 1. As a first remark, we can observe that 30 we handle a large variety of lidar systems. Thus, we have one system with 3b+2e+2d (Warsaw “wa”), three systems with 3b+2e+1d (Bucharest, Observatory Hohenpeissenberg and Potenza“bu”, “oh” and “po”), five systems with 3b+2e (Athens, Cabauw, Evora, Granada, and Thessaloniki“at”, “ea”, “ev”, “gr”, and “th”), four systems with 3b (Barcelona, Belsk, Leipzig and Minsk“ba”, “be”, “le” and “mi”) and one system with 1b (Sofia“sf”). The total number of b-files and e-files is shown in

Table 1. The total number of particles backscatter coefficient, extinction coefficient and linear depolarization ratio after the first quality checks (EARLINET checks) is: # $\beta$ p355=969, # $\beta$ p532=864, # $\beta$ p1064=830, # $\kappa$ e $\beta$ p355=524, # $\kappa$ e $\beta$ p532=503, # $\text{PDR}_{\delta p}$ 355=131 and # $\text{PDR}_{\delta p}$ 532=320 (total of 4141 profiles). The distribution by stations follows closely Fig. 3. The stations with the largest contribution for Forest Fire category are Athens, Bucharest, Granada, Thessaloniki and Warsaw.

5 Note that the number of particle extinction coefficient profiles equals the number of “e” files while the number of particles backscatter coefficient at 1064nm equals the number of b1064 files. In the case of particles backscatter coefficient at 355nm and 532nm, their number can be larger than the number of “b” files as retrievals of backscatter coefficient is reported also in “e” files, employing the use of Raman channel in the retrieval of backscatter coefficient (using either Raman method or aerosol backscattering ratio method). As seen in Table 1, this is the case for the stations Bucharest, Granada, Potenza and Warsaw  
10 “bu”, “gr”, “po” and “wa”. For the same time stamp, the profile from “e” file is kept. The reason behind is that the backscatter coefficient will be further used to calculate the lidar ratio, and the same spatial resolution as the extinction coefficient is desirable. The occurrence in time of the retrievals is shown in Fig. 4. Only the cases for which the layers have a fire origin are shown (smoke layers). As observed, there are sporadic measurements reported for the years 2008-2011. Starting with 2012, more stations started reporting biomass burning pollution events. The total number of time stamps for which we have at least  
15 one profile with an optical property is shown in the last column of Table 1.

## 2.2 Overview of the metadata

Metadata refers to those parameters which give information about the instrument and site location, data processing or analysing, and are saved as general attributes in the “e” and “b” netCDF files. The fixed parameters refer to the measurement position, system name, emission and detection wavelengths. The dynamic parameters change in time and space: date and time

20 of measurement, raw resolution, time resolution (shots averaged), detection mode, final resolution, evaluation method. Another two parameters (Input Parameters and Comments) can give additional information (e.g. values used for Rayleigh calibration). Detection mode (type of data acquisition) can be analog, photon counting or both (glued signal). Evaluation method (approach used to retrieve the optical properties) can be Fernald-Klett method (used in b-files to calculate particle backscatter coefficient), Raman method (used in e-files to determine particles extinction coefficient), aerosol backscatter ratio to obtain particles  
25 backscatter coefficient using a combination of both elastic and Raman channels (recorded in e-files). The information for parameters is provided in a free style comment format and we could not perform the quantification for all parameters (e.g. we could not determine which was the final spatial resolution nor the method used for smoothing and error calculation). In general, there are three approaches reported: 1) keep the errors within an established threshold and thus vary the spatial resolution, 2) maintain a fine spatial resolution (with high statistical errors), 3) perform variable smoothing (e.g. lower spatial resolution  
30 above PBL). As expected, the backscatter profiles are less smooth than the extinction profiles.

The summary of the statistics (based on entire dataset input) over the Detection mode, Evaluation method, Raw resolution, Shots averaged and Zenith angle for each backscatter and extinction coefficient is given in Table S2 (Fig. 2, stage III in Methodology). The main features are the following. For b355 and b532 files, the detection mode the most employed is the

glued signal, while for b1064 it is the analog signal. For e-files, the detection mode the most employed is the photon counting. The most used evaluation approach for b-files is Klett-Fernald (for particles backscatter coefficient) while for e-files is Raman (for particles extinction coefficient). Please note that there are 139 cases reported for b1064 which uses as evaluation method Raman ([Warsaw “wa”](#) station). The station used a PollyXT system and the algorithm employed to calculate the particles backscatter coefficient at 1064 nm involves the extinction coefficient determined at 607 nm from the Raman signal (no reference is available). Concerning the raw resolution, most of the stations used 3.75 m for backscatter and 60 m for extinction. The zenith angle was mostly 0. The shots averaged were in general of tens thousands. This overview shows that we deal with a variety of approaches to compute the mean profile and associated uncertainty.

### 3 Data quality control

10 The first check on data quality consisted of verifying the data which passed the quality control a.t. EARLINET criteria (Fig. 2, stage II in Methodology). The description of the checks can be found on EARLINET website (<https://www.earlinet.org/index.php?id=125>, last access 20191126). Basically, there are two types of checks. First check consists on technical checks on the raw data submitted (applied on-fly since June 2018). Here the conformity of the file content is checked w.r.t. EARLINET file structure and quality control (QC) procedures. With on fly version, an automatic feedback is provided to the Data Originator reporting all the problems incurred for each rejected file, fostering the prompt resubmission of the data (see 20180614 report on <https://www.earlinet.org/index.php?id=293>, last access 20191126). Also, the files not providing the associated error are eliminated. The second check (physical), applied off-line, first verifies if the data was submitted to the right category. Then, the errors are checked for negative values occurrence. Specific checks on backscatter and extinction coefficients are performed (e.g. if larger than a threshold, if integrated quantities such as AOD are within 15 common limits) as well as on intensive variables (where possible), such as LR. The current short description corresponds to the documents issued by 14 June 2018. Three text files are generated with the name of the files rejected by technical criteria (QC\_0.0.txt) or passing technical criteria but failing physical criteria (QC\_1.0), the files passing both tests being shown in the file QC\_2.0. After the EARLINET QC tests, there were 2341 out of 3579 initial files (available from 14 stations) that there were passing both tests from (i.e. ~ ~~650~~ %). After adding reprocessed data/newly processed data, the total number of input 20 files increased to 3589.

25 Several in house checks (most of them manually performed) were further applied for the selection of good quality data. Recall that the additional and revised profiles sent by several stations were not on-fly QC by the EARLINET procedures. Note that the additional quality checks are performed along various steps during data analysis and are briefly discussed here. The off-line QC was manually performed for each profile before applying the algorithm for the layers’ detection (section 4.1). Thus, 30 profiles showing atypical behaviour (biased towards negative values, unrealistically increasing above a certain altitude, with PDR outside the [0 1] range) were dismissed. Sometimes, there were profiles which did not show a clearly defined layer and thus they were eliminated (section 4.1.). The profiles for which no fire was found along the backtrajectory were also eliminated

(section 4.3). The optical properties in a specific layer were dismissed if the number of available points were less than 90%, and thus, no mean value was calculated (section 4.4). Values of the mean optical properties for which SNR was less than 2 were also dismissed (section 4.4). Finally, the values of the intensive parameters with  $\text{SNR} < 2$  and outside the imposed limits are also excluded (section 4.4).

## 5 4 Data analysis

### 4.1 Calculation of the aerosol layers boundaries

Prior to evaluation of the layers' boundaries (Fig.2, stage IV in Methodology), a manual QC of the profiles of the optical properties was performed. Thus, a number of optical properties profiles which did not show expected realistic behaviour were eliminated. The most common behaviours of the profiles being eliminated are:

- Profiles showing a large range of negative values due to a systematic error resulting in a bias towards negative values.
- Profiles displaying an increase above a certain altitude, most probably due to a non-accurate calibration region.
- Depolarization profiles displaying values outside  $[0, 1]$  region.
- To noisy profiles ( $\text{SNR} < 1$ ).

~~The following approach was considered to calculate the boundaries of the aerosol layers. The order of selecting the optical profile to determine the boundaries of the aerosol layers is the following:  $\beta p1064$ ,  $\beta p532$ ,  $\beta p355$ ,  $\kappa p532$ ,  $\kappa p355$ . In other words, when available, use  $\beta p1064$ . When  $\beta p1064$  is not available, use  $\beta p532$ . If the latter is not available either, use  $\beta p355$  and so on. Note that for the times when none of the profiles showed a pollution layer, all profiles for that specific time were excluded.~~

~~Once the optical profile (including the associated error profile) and the corresponding altitude profile are available, the algorithm developed to determine the aerosol layers boundaries is run. The steps of the algorithm are the following:~~

- ~~— Perform a smoothing of the optical profile. The number of bins used for smoothing depends on the input resolution. Thus, for a resolution of 3.75 m, we applied moving average over 23 bins. For a resolution of 7.5 m, 15 m, 30 m, 60 m, we used 11 bins, 9 bins, 7 bins and 3 bins, respectively. For the particular cases of "ea" and "oh" systems, we applied a number of bins of 15 and 19, respectively (as the signals were very noisy). The corresponding errors were propagated.~~
- ~~— Employ the function `findpeaks` from Matlab ([www.mathworks.com](http://www.mathworks.com), last access 20191126) to find the maxima, with the following options: the minimum distance between peaks is 300 m (`MinPeakDistance`) and the minimum peak height (`MinPeakHeight`) is as follows: 1e-7 for  $\beta p1064$ , 1.5e-7 for  $\beta p532$ , 3e-7 for  $\beta p355$ , 1e-6 for  $\kappa p532$  and 3e-6 for  $\kappa p355$ . The value of the minimum distance between peaks was chosen as in Nicolae et al. (2018). If no peaks are found, the routine returns the message no layers with maximum above `MinPeakHeight`.~~

— Employ the function *findpeaks* to find the minima, with the following option: the minimum distance between peaks is 300 m (*MinPeakDistance*)

— eliminate adjacent maxima if the “prominence width” (<https://www.mathworks.com/help/signal/ug/prominence.html>, last access 20191126) overpasses the position of the adjacent maxima

5 — eliminate small maxima / minima peaks which are smaller than 10% of the maximum / minimum peak

— a maximum peak should be bordered by two minima; when the first or the last minimum is missing, a criterion is used to add the missing minimum; thus, the minimum is chosen at a location ( $> 300$  m from the first or the last maximum peak) where the optical property has the minimum value

— the boundaries of a layer are determined by two minima with the condition that there is a maximum between them

10 Following the criteria discussed, there can be cases when it is not possible to find any aerosol layer. Consequently, those profiles were dismissed. Additionally, a manual check was performed and for the cases with non accurate estimation of the boundaries, the boundaries were manually corrected (~ 40 % of the cases) and sometimes, we added layers which had a maximum below the threshold of the minimum peak height. Thus, we cope with a semi automatic algorithm. Table 3 shows the number of time stamps when it was possible to determine a layer and at least one optical property could be calculated

15 (column 3). Recall that many profiles were dismissed manually through quality check before we apply the algorithm for layer boundary evaluation and this explain most of the “missed” cases (difference between second and third columns). The initial total number of layers, with at least one optical property (column 4) is greater than the time series (column 3) as most of the times we have more than one layer within a profile. The other columns are discussed in the next section. Overall, we were able to determine 1901 layers for 960 time stamps (out of 1138 in total).

20 Various authors use different criteria to estimate the layer boundaries. In most of the papers examined, the authors do not describe how they determined the boundaries of the layers. However, the boundaries can be easily identified visually (a common practice when investigating one or few cases). In a few studies it is mentioned the gradient method (Giannakaki et al., 2015; Mattis et al., 2008; Ortiz Amescua et al., 2017; Preißler et al., 2013). When intensive parameters are available (e.g. EAE or LR), one can determine the boundaries based on intensive parameters being nearly constant in the layer (e.g. Samaras et al., 2015) or based on the ratio of elastic to Raman profiles (Vaughan et al., 2018). In situations when a few layers are visible, one can choose them as a single large layer (e.g. Ansmann et al., 2009). Our approach provides the layers boundaries in line with those shown by Ansmann et al. (2009), Janicka et al. (2017), Hu et al. (2018), Veselovskii et al. (2018).

25 The algorithm to describe the layers boundaries is described in Section 2 of the Supplement.

A few examples of boundaries estimation of the (smoke) pollution layers are shown in Fig. S15 in Supplement. All the optical properties profiles are shown (left - particle backscatter coefficients, middle - particle extinction coefficients, left - particle linear depolarization ratio), in order to get a glimpse of how the layers look like for all profiles. First plots (a-e) show examples of automatic selection of the layers based on developed algorithm. First four are based on b1064 signal, while the fifth is based on b355 signal. The next plots (f-i) show examples where one or more boundaries are manually modified. The last plot is based

on b532 signal. In example f) a layer automatically selected around 6500 m was dismissed (considered as not substantial) while in example g) the uppermost layer was manually added. The layers are shown by the grey areas.

Most of the layers detected are situated between 1000 and 5000 m altitude (typically above PBL). However, the minimum layer bottom was found at 257.5 m while the highest layer top was found at 19,8 km. Minimum, maximum and the mean layer thickness were 300, 6862.5 and 1337.5 m. Please note that not all the layers shown here have BB origin (as this check is not performed yet).

~~The optical profiles shown in Fig. S1 to illustrate the layer estimation show also various questionable patterns for different optical variables. Our quality checks were meant to eliminate profiles (or parts of profiles) where suspicions arise. The examples shown in a), b) and h) were eliminated as they were considered of non-BB origin (as discussed later). For the profiles in c), all layers have BB origin. Various QC did not allow the estimation of the IPs based on non-reliable backscatter coefficient at 355 nm for second and third layer while PDR@355 was dismissed as well. For d) case, both layers have BB origin. QC did not allow the retrieval of various IPs based on non-reliable backscatter coefficient at 355 nm. For g) case, the first layer was considered as having BB origin. QC did not allow the computation of the mean PDR in the layers. For i) case, all three layers have BB origin. However, the QC allowed the estimation of both LR and EAE for first layer and only EAE for the second layer.~~

## 4.2 Calculation of the back-trajectories

Even if the lidar data were stored within Forest Fires category in EARLINET/ACTRIS database, in many cases there are situations when several aerosol layers are present and not all of them have a BB origin. Thus, we would like to differentiate these cases and eliminate the non-smoke layers from analysis.

Matlab and Python routines were used to automatically obtain the back-trajectories using Hysplit. The settings for Hysplit backward run are the following: input altitude (middle of the layer) is provided about sea level (a.s.l.), run time is 240 h, meteorological model is GDAS at 0.5° resolution, vertical motion is chosen as Model vertical velocity (Fig.2, stage V in Methodology). The terrain height is saved in the output txt file. For 23 cases (during August 2010, 2012 and 2013), the GDAS meteorology was not available at 0.5° resolution and thus, a manual run was performed using a resolution of 1°. For the situations when more than three layers were available for a profile, Hysplit was run more than one time. There were 75 such cases. We performed 1036 Hysplit runs for 1901 layers corresponding to 960 time stamps.

Hysplit backtrajectory is the most used tool to track the airmass origin. For the literature review on BB, 30 papers made use of Hysplit (references 5, 6, 10-12, 14-21, 23, 24, 28-44, 46 on S2 Table), whereas five studies use Flexpart (refs. 2-4, 24, 26 on S2 Table). The running time used in Hysplit simulations reported in literature varies from two to ten days.

## 4.3 Layers identification based on back-trajectories and fires emissions

The output from the Hysplit text files and the information about fires taken from FIRM MODIS (<https://firms.modaps.eosdis.nasa.gov/>, last access 20191126) were used to produce the combined plots containing information

about both the fires' presence and the back-trajectory (Fig. 2, stage VI in Methodology). The fires are represented on the plots as a function of their fire radiative power (FRP), using different colours and sizes (see legend). The location of the trajectory, each 24 h backwards, is shown by the number of hours. The lower plot shows the altitude a.s.l. of each back-trajectory versus time. The fires are chosen within 100 km and within  $\pm 1$  h around trajectory points (backtrajectory data are available at 1 h temporal resolution). In other words, we assume that those fires are more likely to contribute to the transported smoke, recorded by the lidars. When no fire is recorded along a trajectory, we catalogue that layer as of non-biomass burning origin (dismissed from further analysis). As a consequence of this criterion, a number of 283 time stamps were considered as having layers with non-BB origin. For many cases, for the same time stamp, there were equally layers of BB origin and non-BB origin. We obtained a number of 678 Hysplit-FIRMS plots (one for each time stamp). Note that the Hysplit-FIRMS plot (corresponding to a time stamp) contains all available layers with fires detected along trajectory. Examples of such plots are given at a later stage, when discussing specific events (Figs. 12 and 14). Based on these criteria, the number of time stamps and corresponding number of layers with BB origin are shown in columns 5 and 6 in Table 3 (compare with columns 3 and 4).

It is worth mentioning that the Hysplit model does not provide the uncertainty. In order to get a possible uncertainty of an individual trajectory, a trajectory ensemble is suggested (Rolph et al., 2017). We may assume that high uncertainties in the airmass location may occur particularly over long periods of time (e.g. ten days), which in conjunction with fires location may mean a missed fire or a fire detection that was not contributing to the measurement. Drexler (<https://www.arl.noaa.gov/hysplit/hysplit-frequently-asked-questions-faqs/faq-hg11/>, last access 20191126) mentions that the uncertainty is between 15% and 30%. On the other hand, FIRMS may miss some fires (especially during cloudy atmosphere). According to Giglio et al. (2016), the collection 6 MODIS has a smaller commission error (false alarm) as compared with Collection 5 (1.2% versus 2.4% respectively). The probability of fire detection (regionally) increased by 3% in boreal ~~North~~<sup>N</sup> America, while staying almost the same in regions as Europe or ~~North~~<sup>N</sup> Africa. We have been using fires with a confidence level larger than 70%. We did not investigate the injection height based on FRP in order to estimate if the smoke of a particular fire reached indeed the altitude of the backtrajectory. We would like to emphasize that due to the satellites polar orbit, the same geographical location can be seen four times a day at the equator and more times as the latitude increases (due to orbits overlap). Thus, we may miss a certain number of fires (which burn less than few hours, between the two orbits). However, we may consider those short life fires as not significant in smoke production.

FIRMS database was used in several studies to identify the BB origin. However, all fires occurring over certain periods (for which the backtrajectories were calculated) are typically accounted for. Thus, there were reported fires occurring over the whole day (e.g. Nicolae et al., 2013; Stachlewska et al., 2018; Janicka et al., 2017), or several days (e.g. Mylonaki et al., 2017; Heese and Wiegner, 2007; Tesche et al., 2011). By contrast, our novel approach accounts only for those fires which were occurring around backtrajectory (100 km radius) at the time of air masses passage ( $\pm 1$  h).

#### 4.4 Calculation of the mean optical properties and intensive parameters inside the layers

After determining the aerosol layers and their boundaries (sections 4.1 – 4.3), the mean value of the optical properties is computed for each layer (Fig. 2, stage VII in Methodology). Note that the first and last 50 m of each layer were not considered for the calculation (cf. Nicolae et al., 2018). The uncertainty for each mean value was computed following the error

5 propagation. The mean value in the layer was calculated if there were at least 90% of the points available (the ratio between the layer depth and the resolution in the layer). There were many cases for which the extinction coefficient or the linear particle depolarization ratio could not be calculated as typically their profiles have a shorter extend than that of a backscatter coefficient. A visual check is performed as well, and thus, where the profiles were suspicious, the mean values in the layers were manually set to NaN.

10 The signal to noise ratio (SNR) was computed as the ratio of the mean value to its uncertainty (e.g. Nicolae et al., 2018). The values of each optical property for which  $\text{SNR} < 2$  were dismissed. In Table 3 (columns 7 and 8), we show the number of the time stamps and the layers with a good SNR for optical properties. As a result of this criterium, only one time stamp was dismissed (Athens~~“at”~~) and three layers (one for each of “at”, “bu” and “oh” Athens, Bucharest and Observatory Hohenpeißenberg). Please keep in mind that the number of dismissed optical properties in layers is larger than the number of

15 dismissed layers, as one layer is dismissed only when all optical properties in the layers are discharged.

Figure 6S2 shows an example (for “at”Athens) of the number of layers selected and the corresponding number of optical properties evaluated in each layer. For this example, we have 171 / 172 time-stamps from which we could determine 250 layers. It was just one layer for which we could not determine the optical properties due to SNR constraint (see columns 5-8 in Table 3).

20 An example of the mean optical properties computed in the layers (versus measurement time) is given in Fig. 7 for Bucharest~~“bu”~~ station. The range of values taken by different variables is large. Another aspect is the lower number of values reported or retrieved for extinction and depolarization (these features are specific to all stations). The figures for all the stations will be shown in the companion paper. Systematic measurements and more intensive parameters were available for Athens, Bucharest, Thessaloniki and Warsaw “at”, “bu”, “th” and “wa” stations while over the entire analysed period, systematic

25 measurements were provided by Athens, Bucharest and Thessaloniki “at”, “bu” and “th”.

Once the mean optical properties were calculated, the intensive parameters were determined (where possible) (Fig. 2, stage VIII in Methodology). All the IPs have  $\text{SNR} > 2$ . The imposed limits (data filtering) for IPs are the following:  $\text{LR}@355 = [20$  150] sr,  $\text{LR}@532 = [20$  150] sr,  $\text{EAE} = [-1$  3],  $\text{BAE}@355/532 = [-1$  3],  $\text{BAE}@532/1064 = [-1$  3],  $\text{PDR}@355 = [0$  0.3] and  $\text{PDR}@532 = [0$  0.3] (following closely Burton et al., 2012; Nicolae et al., 2018). The figures representing the intensive 30 parameters for all the stations will be shown in the companion paper. The collected records about intensive parameters found in literature (46 reference values from 39 cited papers) are shown in Fig. S34 and Table S34 in supplement. Table S42 shows the cited references. The extreme values for  $\text{LR}@355$  are 21 sr (Müller et al. 2005) and 130 sr (Tesche et al. 2011) while for  $\text{LR}@532$  are 26 sr (Müller et al. 2005) and 147 sr (Mariano et al. 2010). For  $\text{EAE}355/532$  we have 0 (Müller et al. 2005) and

2.4 (Giannakaki et al., 2016). For BAE@355/532 we found 0.35 (Tesche et al., 2011) and 2.8 (Giannakaki et al., 2010) while for BAE@532/1064 we found 0.29 (Tesche et al., 2011) and 2.85 (Gross et al., 2013). For PDR@355 the extreme values were 1% (Janicka et al., 2019) and 31% (Vaughan et al., 2018) while for PDR@532 the extreme values were 0.3% (Stachlewska et al., 2018) and 20% (Hu et al., 2018). Figure 8S4 shows an example (for Athens<sup>“at”</sup>) of the number of layers selected and the corresponding number of intensive parameters retrieved. One can compare with Fig. S26 over the difference between available number of optical properties and the final number of intensive parameters. An example for the intensive parameters is shown in Fig. S29 for Warsaw<sup>“wa”</sup> station. For Warsaw site, all profiles for extinction and backscatter were calculated using the classical Raman evaluation (Ansmann et al., 1992). The lines in magenta and cyan represent the minimum and the maximum as reported in literature. ~~Several values outside the literature range are observed for EAE, both BAE and PDR@355.~~

In general, LR, EAE, both BAE and PDR are spread well within the reported limits, although the latter is rather in its lower range. Lower PDR may be explained as due to specific location of Warsaw being much closer to BB sources in Ukraine, Belarus and Russia than other EU countries, and therefore much more exposed to faster and more direct BB transport to this site. In such case, differences of properties with respect to other measurement sites in Europe are expected and revealed within our work. Moreover, Warsaw is much less exposed to mineral dust intrusions, in comparison with many EU sites at which the BB measurements are more likely to be affected by slight contamination of dust, e.g. Spanish sites. On the other hand, Warsaw is an urban site, thus for BB observed in layers at lower ranges a slight contamination of the BB with the local urban pollution is possible. For higher layers, industrial pollution from Silesia region in Poland (Stachlewska et al. 2018) or Ruhr region in Germany (e.g. case here on 20160704 at 07:30) is possible. This can explain a few values outside the literature range observed in Warsaw, i.e. for EAE (2 values), for both BAE (33 values) and for PDR355 (8 values). The extreme values for EAE observed on 20160704 07:30 and 20170619 20:30 (2.6 and 2.8 respectively along with  $CR_{LR} < 1$ ) correspond to fires in Germany / Belgium and United Kingdom respectively. The fires occurred in less than 40 h before smoke measurements and thus we can consider the smoke relatively fresh.

The mean, median, minimum and maximum values taken by the intensive parameters for all the stations providing at least one parameter (all stations but Sofia<sup>“sf”</sup>) are discussed in the companion paper. The final number of selected layers and the corresponding time stamps are shown in Table 3, columns 9 and 10. The range of values taken by a specific parameter is large. The number of outliers dismissed based on predefined ranges of acceptable values for each intensive parameter is small (3.7% per total). For each IP we have the following numbers: 8/305 (2.6%) for LR@355nm, 8/253 (3.2%) for LR@532nm, 18/243 (7.4%) for EAE~~355/532~~, 39/642 (6.1%) for BAE355/532, 21/706 (3%) for BAE532/1064, 0/132 (0%) for PDR@355 and 0/242 (0%) for PDR@532. Please note that a thorough investigation of the outliers was not performed. Conversely, we focused on a semi-automatic evaluation by applying different criteria for outliers' elimination (filtering). One can draw three possible reasons for the presence of outliers: a) the smoothing applied on the Raman signals, which induces a very smooth profile for extinction coefficients, b) a shift of the profile towards higher altitude (most probably due to non-accurate calibration range) and, c) a slight difference between the peaks of the backscatter versus extinction or a small difference in the slope (most

probably related with the smoothing of the Raman signals). All values of the intensive parameters will be shown in the companion paper. After outliers' elimination we start the data (IP) interpretation.

## 5 Data interpretation

~~We have focused on several directions to investigate and interpret the measurements by means of the intensive parameters.~~

5 ~~Here we show examples for each direction, while the comprehensive analysis will be performed in the following paper.~~  
~~According to Müller et al. (2005, 2007, 2016), effective radius of BB particles increases with time (distance), most probably due to coagulation and aggregation of the particles (Reid et al., 2005). On the contrary, EAE decreases with time (distance). While the heaviest particles will sediment during transport, the particles reaching measurement site are still larger than the emitted ones. It was shown that for aged BB particles  $LR@532 > LR@355$  (e.g. Wandinger et al., 2002; Murayama et al., 10 2004; Müller et al., 2005; Sugimoto et al., 2010; Nicolae et al., 2013). Measurements and retrieved values of effective radius of BB particles showed that the fresh particles have a mean radius around 150 nm, while the aged particles have a radius around 300–400 nm (Müller et al., 2007). Particle size depends on many factors such as the combustion type in fires (in flame or smouldering) or type of vegetation while the smoke aerosol undergoes different physical chemical processes in atmosphere. (Reid and Hobbs, 1998). Differences between smoke properties in different regions were also found. Thus, smoke particles 15 from Brazil absorb more and scatter less the solar radiation as compared with smoke in N America (Reid and Hobbs, 1998). Müller et al. (2005) observed differences between N America and Siberian smoke over Germany; particles from N America showed smaller size and higher EAE. Veselovskii et al. (2015) tried to relate BAE with EAE and showed that while EAE depends mainly on particle size, BAE depends both on particle size and refractive index, being very sensitive to the latter (see their Fig. 20). In specific conditions, for the region of 0.5–1.5 for EAE,  $BAE@532/1064$  decreases ( $BAE@355/532$  increases) 20 with increasing EAE (see their Figs. 20 and 22). However, in different conditions for particles size, refractive index and fine mode fraction, both BAE can increase with increasing EAE (see their Fig. 19). On the other hand, Su et al. (2008) showed few scenarios for the relationship between  $BAE@532/1064$  and  $EAE@553/855$ , which depend on RH and the contribution of the fine mode fraction. While for a high fine mode fraction in the smoke composition and  $RH < 85\%$ ,  $BAE@532/1064$  increases with increasing  $EAE@553/855$  ( $EAE > 2$ ), for a dominant coarse mode and  $RH < 85\%$   $BAE@532/1064$  decreases with 25 increasing  $EAE@553/855$  ( $EAE < 0.5$ ) (see their Fig. 8). According to Veselovskii et al. (2018),  $PDR532$  decreases with increasing EAE. In general,  $LR532$  increases with increasing  $LR355$  (e.g. Nicolae et al., 2018). Similarly,  $PDR532$  increases with increasing  $PDR355$  (e.g. Stachlewska et al., 2018).  
Concluding the findings so far, we expect a colour ratio (CR) for  $LR > 1$  for aged smoke ( $LR@355$  decreases and  $LR@532$  increases with aging smoke) and EAE decreasing with time (distance).  $PDR@532$  increases with time (while EAE decreases). 30 The studies showed no straightforward pattern for  $CR_{BAE}$  and  $CR_{PDR}$  evolution with time.  
~~We have focused on several directions to investigate and interpret the measurements by means of the intensive parameters.~~  
~~Here we show examples for each direction, while the comprehensive analysis will be performed in the following paper.~~~~

The following results were found in literature regarding the IPs values versus travel distance (time travel):

- effective radius: According to Müller et al. (2005, 2007, 2016), the effective radius of the BB particles increases with time (distance), most probably due to coagulation and aggregation of the particles (Reid et al., 2005). Measurements and retrieved values of effective radius of BB particles showed that the fresh particles have a mean radius around 150 nm, while the aged particles have a radius around 300 - 400 nm (Müller et al., 2007). Particle size depends on many factors such as the combustion type in fires (in-flame or smouldering) or type of vegetation while the smoke aerosol undergoes different physical-chemical processes in atmosphere. (Reid and Hobbs, 1998). While the heaviest particles will sediment during transport, the particles reaching measurement site are still larger than the emitted ones.
- EAE decreases with time (distance) (e.g. Müller et al., 2005, 2007, 2016)
- Lidar ratio: It was shown that for aged BB particles (big travel time)  $LR@532 > LR@355$  (e.g. Wandinger et al., 2002, Murayama et al., 2004; Müller et al., 2005; Sugimoto et al., 2010, Nicolae et al., 2013). Thus, the colour ratio (CR) for LR, i.e.  $CR_{LR} > 1$  for aged smoke ( $LR@532$  increases more with aging smoke)
- $PDR@532$  decreases with time (Nisantzi et al., 2014).

The general correlations between IPs were shown:

- In general,  $LR532$  increases with increasing  $LR355$  (e.g. Nicolae et al., 2018; Janicka and Stachlewska, 2019).
- In general,  $PDR532$  increases with increasing  $PDR355$  (e.g. Stachlewska et al., 2018; Janicka and Stachlewska, 2019).

The following differences between smoke properties in different regions were reported:

- smoke particles from Brazil absorb more and scatter less the solar radiation as compared with smoke in North America (Reid and Hobbs, 1998).
- differences between North America and Siberian smoke over Germany: particles from North America showed smaller size and higher EAE (Müller et al., 2005)

The following studies showed different behaviour of BAE versus EAE:

- Veselovskii et al. (2015) tried to relate BAE with EAE and showed that while EAE depends mainly on particle size, BAE depends both on particle size and refractive index, being very sensitive to the latter (see their Fig. 20). On one hand, when the real part of the refractive index increases, the imaginary part is constant, the effective radius for coarse mode and the high fine mode fraction are constant while the effective radius of the fine particles decreases,  $BAE@532/1064$  decreases ( $BAE@355/532$  increases) with increasing EAE (over  $\sim 0.5 - 1.5$  region) (see their Figs. 20 and 22). On the other hand, for a constant refractive index, a fixed effective radius for coarse mode and an increase of the fine mode fraction, both BAE increase with increasing EAE (over  $\sim 0.5 - 1.5$  region). This is visible for different effective radius for the fine particles (see their Fig. 19).
- Su et al. (2008) showed few scenarios for the relationship between  $BAE@532/1064$  and  $EAE@553/855$ , which depend on RH (relative humidity) and the contribution of the fine mode fraction. For a high fine mode fraction in the smoke composition and  $RH < 85\%$ ,  $BAE@532/1064$  increases with increasing  $EAE@553/855$  ( $EAE > 2$ ). For a dominant coarse mode and  $RH < 85\%$   $BAE@532/1064$  decreases with increasing  $EAE@553/855$  ( $EAE < 0.5$ ) (see

their Fig. 8). For  $RH > 85$  there is no clear pattern of BAE with respect to EAE (BAE increasing and then decreasing with increasing EAE).

Concluding the findings so far, we expect  $CR_{LR} > 1$ , small values of EAE ( $< 1.4$ ) and smaller  $PDR@532$  for aged smoke (especially for long range transport from North America). The studies showed no straightforward pattern for  $CR_{BAE}$  and  $CR_{PDR}$  evolution with time. Studies by Veselovskii et al. (2015) and Su et al. (2008) may help interpreting the scatter plots between BAE and EAE. We did not investigate the RH field though.

## 5.1 Fire events seen by several stations. Example for Bucharest and Thessaloniki stations.

Over the ten years period, we have found five events (with retrieved intensive parameters) recorded at two stations which have the same smoke origin (Fig. 2, stage IX in Methodology). The events belong to local fires in Europe. Two events are seen by

10 Athens and Thessaloniki stations “at” and “th” (2014 and 2017) and one event is seen by Bucharest and Thessaloniki “bu” and “th” (2014), Minsk and Warsaw “mi” and “wa” (2015), Atens and Observatory Hohenpeißenberg “at” and “oh” (2016) stations. Unfortunately, we did not obtain common intensive parameters for all events. Only two events had one common intensive parameter (BAE@532/1064). One event is shortly presented below, emphasizing the methodology.

15 The event was recorded during 20140909-20140910 at Bucharest and Thessaloniki “bu” and “th” stations (see time frame and altitude on Fig. 7 a\_Fig. 10 upper right plot). The backtrajectories revealed the same fire origin. Figure 844 shows the air backtrajectories for the layers detected at the two stations. The fires’ location (within 100 km and +/- 1h) is shown as well. The colour and size of the fires correspond to their FRP (see legend). The Hysplit back trajectories in Fig. 844 show that the main smoke source was the fires over eastern Ukraine. Figure 8 a) 44, left (Bucharest “bu” station) indicates as second smoke source from the fires over eastern Romania (~ 72 h back) and North Ukraine (~ 144 h back). The smoke particles were 20 transported from Ukraine to Bucharest station over a period of five days descending from approximately 4200 m on 2014/09/04 to 3000 m on 2014/09/09. For the Thessaloniki station the main source was the fires over southwestern Ukraine (Fig. 8 b44, right). The smoke particles were identified on 2014/09/10 around 2100 m. Note that for Thessaloniki “th” case, the ‘common fire’ was detected at ~ 3500 m. In Fig. 7 a-b10, the first two left plots we show the location of the fires which contributes to 25 all measurements on 9 - 10<sup>th</sup> of September and their histogram occurrence on 1x1 grids. From such histograms we pick the grids where we have fires contributing to both stations. See grid which has both colours, between 36 and 37 E and 47 and 48 N (also marked by a square on the upper plot). The location (longitude and latitude) of these fires from the “common” grid are shown versus fires occurrence time as well as versus measurement time at each station (Fig. 7 c-d10 lower left plots). The common fire revealed through the back-trajectory occurred at 10:39 on 4<sup>th</sup> of September (latitude = 47.537, longitude = 36.275) and it was recorded at ~ 11:00 on 9<sup>th</sup> at Bucharest “bu” and at ~11:00 on 10<sup>st</sup> of September at Thessaloniki “th” (lower layer left). Two layers were detected at Thessaloniki “th” station (where one corresponds to the common fire) and one in 30 Bucharest “bu” station. We analysed if there were other fires contributing to the same measurement as in general, along backtrajectories, we encounter many fires at several locations. In the case of Bucharest “bu” there were 24 other fires (detected 46 times) contributing, located in Ukraine as well as in NE Romania (occurring during 3<sup>rd</sup>, 4<sup>th</sup> and 6<sup>th</sup> of September). For

Thessaloniki “th” we counted 35 other fires (detected 66 times), located at E Ukraine (occurring during 2<sup>nd</sup> and 4<sup>th</sup> of September). See Fig. 8 b)lower plot of Fig. 10. Please note that function of the air trajectory, one fire can be seen more than once (e.g. during a cyclone or anticyclone) or due to slow air motion (spatial-temporal stationarity over the 100 km area and 1 hour).

5 We can conclude that we have a mixed smoke recorded in both Bucharest and Thessaloniki “bu” and “th”. However, the mixtures are different for Bucharest and Thessaloniki ‘bu’ and ‘th’ stations.

Figure 740 right plots shows the layers location (marked by a square in front of the middle of the layer) and intensive parameters for the layers. Note that the retrieval of the intensive parameters was not possible at all times for all layers. The two layers detected in Bucharest and Thessaloniki “bu” and “th” were located at 3061 m and 2123 m respectively.

10 For the measurements at Bucharest“bu” (20140909 10:45 UTC) and Thessaloniki“th” (20140910 11:15 UTC) locations, which correspond to the common fire in E Ukraine (47.537 N, 36.275 E) on 20140904 10:39 (as well as other additional fires for each station), there were the following intensive parameters calculated.

Bucharest“bu”, 09/09 10:45, 3061 m:  $BAE@355/532 = 1.82 \pm 0.0001$ ,  $BAE@532/1064 = 1.32 \pm 0.0001$ ,  $PDR@532 = 6.8 \pm 0.03\%$ .

15 Thessaloniki“th”: 10/09 11:15, 2123 m:  $BAE@532/1064 = 0.51 \pm 0.02$ .

The values for  $BAE@532/1064$  were 1.32 and 0.51 for Bucharest and Thessaloniki “bu” and “th” respectively. The difference between the two values may be explained by the different mixture of smoke (originating from different fires). All the contributing fires for Thessaloniki“th” besides the common fire are located in E Ukraine while the contributing fires for Bucharest“bu” are located in E Romania, E Ukraine and NE Ukraine. According to backtrajectories for Thessaloniki“th”, the 20 other fires contributing to measurements are further located in time than the common fire. Lower value for  $BAE@532/1064$  in Thessaloniki“th” reveals a relatively larger contribution of the big particles to backscatter. On the contrary, in Bucharest“bu” the smallest particles are the most efficient in backscattering.

For the other event with common IP for the same source (20170529-20150602), the smoke was labelled as of ‘single fire’ as no other fires were identified along the backtrajectory. This event will be discussed in the subsequent paper.

25 For the other event with common IP for the same source (20170529-20170602), the smoke was labelled as of ‘single fire’ as no other fires were identified along the backtrajectory. The common fire occurred on 26<sup>th</sup> of May at midnight in Ukraine (48.171 N, 30.622 E) and it was recorded in Thessaloniki and Athens on 29/05 and 31/05 respectively.  $BAE@532/1064$  value in Thessaloniki was less than half of that in Athens, while  $BAE@355/532$  was larger for Thessaloniki. High BAE corresponds to higher backscatter at smaller wavelengths, which indicates a higher number of small particles. The values in Thessaloniki 30 correspond to a higher number of small size particles (at 355 nm) and with a higher proportion of large particles (at 1064 nm) compared with Athens.  $CR_{BAE}$  (colour ratio of the backscatter Ångström exponents) increases from Thessaloniki to Athens (0.22 to 0.78, respectively), which suggests an increase with travel distance (time). As  $CR_{LR}$  (colour ratio of the lidar ratios) and  $EAE$  (extinction Ångström exponent) were not available to characterize the smoke in terms of age, we classified the smoke as aged based on the duration of the travel time.

Overall, we conclude that the number of common events as well as the number of the common IPs is limited and, thus, no thorough examination of these events is possible. The most important feature of this analysis is that it enables us to quantify the smoke as of ‘single fire’ or ‘mixed’ and hence explain various IP values. This kind of analysis can be successfully applied in the future, when more data become available.

5

## 5.2 Long-range transport from North America. Example for Athens station.

We have identified a number of 24 events with long range transport from North America (Fig. 2, stage X in Methodology) for which we have at least one intensive parameter retrieved. The events are reported in 2009 and over 2012-2017 period. As in previous section, for each event, we plot the Hysplit trajectory and the location of the fires along it, the histogram with the 10 number of fires in each  $1^\circ \times 1^\circ$  geographical grid, the geographical location (longitude and latitude) versus occurrence time of the fires and versus measurement time at the stations(s). Last, we show the layers altitude (error bar signifies the layer’ thickness) and the intensive parameters in the layers.

We have identified eight measurements periods (events) when the smoke is arriving solely from NorthN America (“pure N America”). The other cases represent measurements of mixed smoke, where the smoke is coming from both NorthN America or 15 NorthN Africa or Middle East. Usually, during measurements period, there were also recordings of BB with other origin (Europe). For each layer we check if the smoke is coming from a single fire or more fires (count their number), and quantify the locations. We have one event when there were measurements taken at three stations and one event with measurements taken at two stations. All others cases represent measurements recorded by a single station. As the number of intensive parameters determined for 20 each station varies considerably, in general we cannot compare directly all IPs for the same event. As a consequence, a statistical analysis will be performed over entire set of parameters. Below we show one example of long range transport recorded in Athens which provided more measurements and more intensive parameters. The event recorded over three days in July 2013 will be discussed in the companion paper.

### 5.2.1 Smoke event recorded on 20170713

25 During this day we recorded several measurements in Athens (see time and layers altitude in Fig. 9 e12, upper right plot). According to backtrajectory and the fire occurrence along it, we determined three layers of NorthN America smoke origin (their location is marked with a black square at the left). As seen in the backtrajectory (Fig. 1013), the fires’ location in NorthN America is different for the three layers (different source).

The first layer of smoke origin was detected at 14:27 at  $\sim 2900$  m altitude. Our calculations show that there were different fires 30 contributing to this measurement. Thus, we have four fires (counted eight times) from which only one fire (counted twice) was of NorthN America origin. This can be seen in Fig. 9 d)12-left last panel as well as in the backtrajectory in Fig. 10 a)13-first plot where we see the fires detected in the first two days backwards (local fires, in Greece and Italy) as well as the fire found

after almost eight days back in [NorthN](#) America. The fire from [NorthN](#) America occurred at 20:14 on 5 July in the longitude by latitude grid [-111 -110] x [50 51]. The location of the fire is shown by blue arrows in Fig. [9 \(a-e\)12](#).

The second layer was measured at 18:49 at 2102 m altitude. 12 fires were found (counted 19 times) to have contributed to the measurement from which one fire (detected once) was of [NorthN](#) America origin. See Figs. [912](#) and [1013](#). The fire from [NorthN](#) America was detected at 19:16 on 6 July in the longitude by latitude grid [-84 -83] x [42 43]. The location of the fire is shown by green arrows in Fig. [9 \(a-e\)12](#).

The last layer was measured at 19:34 at 3872 m altitude. We found two fires (each detected once) of [NorthN](#) America origin. The [NorthN](#) America fires occurred at 09:47 on 6 July and were located in the longitude by latitude grid [-109 -108] x [47 48]. The location of the fire is shown by magenta arrows in Fig. [9 \(a-e\)12](#). The trajectory layer in Fig. [10 c\)13](#) is the higher one (light blue). The local fires observed in the plot are detected by the first layer (at 2012 m).

Thus, we can label the first two layers as ‘mixed’ smoke while the third one as “pure N America” smoke. We observe that for the mixed fires, the contribution from local fires is much larger as we have 6/8 and 18/19 fires counts in Europe for first and second layer respectively. The intensive parameters for the three layers are:

- layer 1 @ 14:27 2942 m, mixed:  $BAE@355/532 = 1.42 \pm 0.03$ ,  $BAE@532/1064 = 1.39 \pm 0.01$
- layer 2 @ 18:49 2102 m, mixed:  $LR@355 = 48.4 \pm 1.04$  sr,  $LR@532 = 33.7 \pm 3.5$  sr,  $BAE@355/532 = 1.72 \pm 0.05$ ,  $BAE@532/1064 = 1.85 \pm 0.02$
- layer 3 @ 19:34 3872 m, [NorthN](#) America:  $LR@355 = 58.5 \pm 2.63$  sr,  $LR@532 = 67.2 \pm 4.79$  sr,  $EAE = 1.02 \pm 0.14$ ,  $BAE@355/532 = 1.36 \pm 0.15$ ,  $BAE@532/1064 = 2.11 \pm 0.08$

We observe that  $BAE@355/532$  has the smallest value for ‘pure N America’ while  $BAE@532/1064$  is the highest. Relatively small value for EAE for the third layer corresponds to bigger (coarse mode) particles, associated with aged smoke. On the other hand, values of LR ( $LR@355 < LR@532$ ) suggest the presence of aged aerosol as well. The layer’s altitude is the highest of all three. The values of LR for the second layer ( $LR@355 > LR@532$ ) suggest fresh aerosol (of smaller size, fine mode particles). This can be supported by the contribution of the local fires (detected a few hours back). If we compare the colour ratio (CR) of BAE we obtain values of 0.98, 1.08 and 1.55 for the three layers.  $CR_{LR}$  for the second and third layers were 0.7 (fresh smoke) and 1.15 (aged aerosol). Based on all reported values in literature (Table S1), we found the following values for  $CR_{LR}$  and EAE for fresh, aged and [NorthN](#) America case (particular case of aged smoke).  $CR_{LR}$  was 0.88, 1.08 and 1.23 while EAE was 1.47, 1.2, 0.95.  $CR_{BAE}$  had the values 0.76, 0.98 and 0.98. We may speculate that  $CR_{BAE}$  may increase with time (distance).

Please note that the time difference (an hour at most) between right plots and bottom left plot comes from the fact that Hysplit back-trajectories start at sharp hours. For example, for the measurement at 18:49 the starting point on back-trajectory is 18.

Statistics over LRT from [NorthN](#) America will be shown in the companion paper. We encountered 168 measurements over the 24 periods (over 2009 – 2017 period). From these measurements, 77 have a [NorthN](#) America origin while the other 91 have a different BB origin (local). The LRT events from [NorthN](#) America is analysed differencing between ‘pure N America’ fires (sensed smoke comes solely from [NorthN](#) America) and ‘mixed’ fires (measured smoke is a mixture of [NorthN](#) America smoke and local/European smoke).

## 5.3 Analysis over geographical regions

### 5.3.1. Geographical regions

Taking into account the position of the 14 stations (Fig. 1), four geographical regions are chosen as follows: SE Europe ([Potenza](#), [Athens](#), [Thessaloniki](#), [Sofia](#), [Bucharest](#)“[po](#)”, “[at](#)”, “[th](#)”, “[sf](#)”, “[bu](#)”), SW Europe ([Granada](#), [Barcelona](#) and [Evora](#)“[gr](#)”, “[ba](#)” and “[ev](#)”), NE Europe ([Belsk](#), [Warsaw](#), [Minsk](#)“[be](#)”, “[wa](#)”, “[mi](#)”) and Central Europe ([Cabauw](#), [Leipzig](#), [Observatory Hohenpeißenberg](#)“[ea](#)”, “[le](#)”, “[oh](#)”).

This corresponds to stage XI from Methodology (Fig. 2). The statistics over the measurements for each individual station show the following. Belsk and Cabauw stations focused on LRT smoke from [NorthN](#) America with ~99 % of the measurements (1149 / 1159 and 1001 / 1013 [NorthN](#) America fires / total number of fires). Leipzig measured 86.2 % (156/181 [NorthN](#) America fires / total number of fires) LRT smoke. The others have measured mostly in Europe as follows (# fires in EU / # total fires): Athens 81.7 % (1657 / 2028), Barcelona 91 % (172 / 189), Bucharest 93.82 % (1883 / 2007 cases), Granada 68.32 % (1643 / 2405), Minsk 98.04 % (1051 / 1072), Observatory Hohenpeissenberg 74.84 % (116 / 286), Potenza 100% (142 / 142), Sofia 100% (16 / 16), Thessaloniki 87.38 % (1807 / 2068), Warsaw 85.4 % (5036 / 5897). For Evora station we encountered 44.39 % (99 / 223) fires in [NorthN](#) America and 48.43 % in Europe (108 / 223). Per regions, we have detected fires from [NorthN](#) America as 4.5 % (282 / 6261), 8.56 % (241 / 2817), 87.55 % (1181 / 1349) and 24.13 % (1961 / 8128) for SE, SW, CE and NE region respectively. The number of fires detected in Europe was the following: 87.93 % (5505 / 6261), 68.26 % (1923 / 2817), 11.34 % (153 / 1349) and 75.01 % (6097 / 8128) for SE, SW, CE and NE region respectively.

In [Fig. 14](#) we show the location of the fires seen by the stations from SE region. Note that the grid size is 1 x 1 degree latitude and longitude. The first remarks for each cluster are the following. As mentioned, for SE region, we have a number of 282 fires located in North America (4.5 %) and 5979 elsewhere (total of 6261 fires), most of them being located in East Europe (5505). The longitude region with most of the fires is between 20 E and 30 E while the latitude region is 37 - 46 N. This corresponds to the Balkan region, covering parts of Romania, Bulgaria, Macedonia, Greece. Most of the measurements were taken at [Bucharest](#), [Athens](#) and [Thessaloniki](#) “[bu](#)”, “[at](#)” and “[th](#)”.

### 5.3.2. Intensive parameters by geographical regions

A statistical investigation over the intensive parameters was performed for each geographical region in order to identify the main features. The analysis was performed by separating the intensive parameters based on their continental source origin. The following origin were considered: Europe (EU), Africa (AF), Asia (AS), [NorthN](#) America (NA) and a combination of any of them (EUAF=EU+AF, EUAS=EU+AS, EUNA=EU+NA, EUAFAS=EU+AF+AS, etc). The statistics was performed over all available cases. Here we present the results for SE region (for consistency). The other three regions will be discussed in the following paper as well as the overall assessment.

[Fig. 15](#) shows the scatter plots for some of the combinations between two IPs. Note that the number of pair points available for each combination is different. The following features are revealed (the mean values are discussed). In average, there is a

linear correlation between the two LR if we dismiss the value for NA. The mean LR@532 is slightly larger than the mean LR@355 ( $CR_{LR} > 1$ ) which suggests the presence of aged aerosol in general. For EU source region, PDR@532 is below 7% (except three values) which corresponds to a low depolarization. For EAE features, we observe low value for EUAF source region ( $\sim 0.65$ ), while the other three source regions (EU, EUAS and EUNA) have similar values, around 1.5 (based on EAE vs BAE@355/532 plot). Large value of EAE ( $\sim 1.5$ ) suggests smaller size aerosol, specific to fresh smoke particles. The values for the EUAS and EUNA mixtures suggest that the contribution of EU fires to the mixture is large. On the other hand, the small value for EUAF region (corresponding to bigger particles) may be due to the major contribution of the AF region (as the value is not close to the EU value) corresponding to relatively big smoke travel time. Further analysis will be performed in part II ([Adam et al., 2020](#)), where both  $CR_{LR}$  and EAE will be accounted for when interpreting the smoke (fresh versus aged) based on the same measurements. The scatter plots between EAE and the two BAE are opposite. While EAE increases with increasing BAE@355/532, EAE decreases with increasing BAE@532/1064 (also reported by Veselovskii et al., 2015, in special conditions). A general decreasing trend of EAE versus LR@532 is observed. The comparison between the two BAE, based on source origin, did not show a specific relationship. Based on standard deviation, we observe a big overlap among the values for all source regions. In conclusion, based on the current dataset, there is no clear separation between sources for SE region but for average values, specific trends are observed for some scatter plots.

As the dataset is limited, we cannot conclude at this stage about the existence of a clear feature with respect to the continental source origin. As mentioned on literature, EAE exhibits a decay versus time (while smoke effective radius increases with time). In the present example, for SE region we obtained quite large values for mixtures which suggest a large contribution of the European fires. On the other hand, for EUAF mixture, the value was quite small, which suggests a relatively big travel time.

Medium absorption as shown by LR for both 355 nm and 532 nm ( $\sim 50$  sr) was observed for EUAS, EUAF and EU regions. The smallest / largest value for LR@355 / LR@532 was observed for NA region, suggesting less / more absorption for small / medium size particles. The LR values for EUNA source are close to those for EU source which suggest once more the big contribution of EU fires to the mixture.

The complete analysis of IPs and CRs will be performed in the companion paper. Based on a larger IP dataset, we expect that the complete set of CR for LR, BAE and PDR, along with EAE will better characterize the measured aerosol. The statistics over all four regions will eventually bring more insights about the IPs and CRs trends versus continental source origin.

## 6. Summary and conclusions

The current study focuses on developing a methodology to analyse large amounts of biomass burning measurements by lidars. The current lidar dataset is from EARLINET database, Forest Fire category.

First, we would like to mention the current challenges when performing such analyses. Besides tackling with high amount of data, there is different data processing used by stations (using either their own algorithms or more recently SCC). The data still need quality control checks and the best way is the manual check. For more accurate results, the algorithm developed to detect

the pollution layers needs a manual check as well, and thus, the boundaries are manually corrected where required. If the investigation is based on intensive parameter results, one has to bear in mind that their number is a limited subsample of the initial data set. This is due to two main factors. First, not all of the lidar systems provide the complete sets of the intensive parameters. Second, the quality checks remove a large amount of data (more than half of the initial dataset).

5 The possible sources of uncertainty during such an analysis may be the following. A small change in the input to Hysplit may give a different output (e.g. use of altitude a.g.l. versus a.s.l., use of GDAS0.5 versus GDAS1). See for example Su et al. (2015). Various algorithms employed to estimate the layer geometry may give slightly different values over the mean values in the layers. Thus, the direct comparison with other reports over the same event should be carefully performed. Uncertainties in Hysplit backtrajectories as well as in FIRMS database are not considered. Least but not last, the imperfect data quality 10 control (including the present methodology) may contribute as well.

The current methodology (Fig. 2) describes various criteria involved in order to assure a quality-controlled dataset and the steps preceding the computation of the mean intensive parameters in the layers. The algorithm to select the layers of BB origin, employing the information from both Hysplit and FIRMS within the current criteria (*novelty*) allowed us to identify only the fires which most probably contributed to the measurements. Further, we were able to determine if the smoke measurements 15 were originating from a single fire source or from many fire sources by identifying all the fires along backtrajectory (*novelty*). Therefore, we could quantify the measurements as having a ‘single fire’ source or ‘mixed fires’ sources, having a *NorthN* America origin (‘pure N America’) or a ‘mixed origin’ (*NorthN* America and Europe). The number of fires occurring along a backtrajectory as well as the number of fires’ counts was calculated (*novelty*). Further, we proposed few directions for BB study by means of the intensive parameters.

20 The first direction is to study the same BB event through the measurements taken at several stations. For the current dataset we found five events as observed by two stations. The common fire source is precisely identified while the number of other fires contributing to the smoke measurement was quantified (*novelty*). For two cases, BAE@532/1064 could be compared. In the current example, the measurements represent smoke originating from several fires (mixed smoke). We found that BAE@532/1064 had a smaller value for the station which recorded smoke transported for a longer time for the common fire. 25 The differences between the two values can be attributed to the fact that the mixed smoke measured in the two locations originated from different fires (besides the common fire).

The second direction was the study of LRT of smoke from *NorthN* America. 24 events were available. We have identified that the LRT from *NorthN* America can be of *NorthN* America origin only or a mixture of both *NorthN* America and local fires (*novelty*). The quantification of the smoke as mixed explained various values for IPs in cases where the values were closer 30 either to *NorthN* America type or to European type. In the example shown here, we identified three layers where two were labelled as ‘mixed’ and one as ‘pure N America’. For the later, EAE (1) and  $CR_{LR} > 1$  suggested aged smoke, larger particle size. For one of the mixed smokes we had  $CR_{LR} < 1$  suggesting fresh aerosol (no EAE available). This can be explained by the contribution of the local fires detected. For the ‘pure N America’ smoke layer we obtained the smallest BAE@355/532 and the larger value for BAE@532/1064.  $CR_{BAE}$  provides the biggest value for ‘pure N America’ smoke.

The third direction was based on consideration of four geographical regions (SE, SW, NE and CE Europe), analysed individually. Histograms of fires' locations as detected by individual stations (through HYSPLIT and FIRMS) are presented (*novelty*), showing the predominant type of measurements taken by each station (local versus LRT).

Statistics over intensive parameters were performed in the following manner. For each geographical region, the scatter plots between various IPs were drawn and the mean values for each IP were computed function of continental BB origin. In the present example for SE region, we could observe the following (Fig. 15). LR@532 versus PDR@532 for EU source region suggest the presence of medium size particles with low depolarization and relatively high absorption. A linear dependence of LR@532 versus LR@355 was observed (as reported in literature) with colour ratios larger than one, suggesting the presence of aged smoke in average. EAE had the smaller value for EUAF source region, suggesting relatively high particle size (aged smoke). EAE values for EU, EUAS and EUNA had similar values, relatively large (~1.5) suggesting relatively small particle size (rather fresh smoke). High EAE values for mixtures (EUAS and EUNA) can be explained by the large contribution of EU fires to the mixtures. Based on SE results, we found the following trends. EAE increases with increasing BAE@355/532 and decreases with increasing BAE@532/1064. A slight EAE decrease with increasing LR@532 was observed as well. The relationship between the two BAE does not show a clear feature. Note that for the current dataset, the standard deviation is large for all the means and there is an overlap among most of the values.

One of the important outcomes of this study is the quantification (within the existing assumptions) of the fires which contribute to the smoke measurement. As observed, in most of the cases, the smoke measured have several fire sources ('mixed smoke'). Note that in the part II paper more discussion is given on the statistical analysis based on the four geographical regions considered where the data are interpreted function of continental source origin.

The current paper presents first ever such widely applied approach for the analyses of the BB optical properties derived from the lidar measurements. Full methodology was developed, from QC via selection of the layers to obtaining mean optical properties with uncertainty analyses. Comparison of optical properties of BB aerosol depending on its origin was possible and revealed interesting and distinctly different results for various regions of Europe. In general, we measure mixed smoke and thus, we do not recommend to associate precisely a measurement with a specific source without a careful check over other possible source. Based on favourable meteorological conditions and the fires' sources locations, the analysed stations or regions provides different measurements. Thus, Central Europe mostly measures LRT smoke from [NorthN](#) America, SW Europe mostly measure smoke originating from Iberic Peninsula and [NorthN](#) Africa, while SE and NE Europe mostly measure smoke originating in E Europe. The current study provides a reference for further research, including algorithm testing and aerosol typing. As for the limitations, we show that although enormous efforts are undertaken on the EARLINET-ACTRIS regular long-term observations, still the availability of the optical properties profiles in the database is limited, which is mainly due to the fact that for many stations still manual evaluation of profiles is needed. Therefore, we see a strong need for both the further development of the SCC data evaluation automated chain as well as the use of this evaluation chain by as many as possible stations for processing of lidar data. The present methodology can reveal more insights regarding the specifics of different measurement regions versus various sources when a larger number of IPs is available.

In order to increase the number of input data and further the number of intensive parameters as well as the BB study through measurements taken at several locations, we recommend to have coordinated measurements in EARLINET during BB events. On the other hand, there are numerous events discussed in literature while the data is not reported in EARLINET yet. The data should be treated in the same manner (use SCC). The data quality control through SCC output still needs improvement. We 5 acknowledge the large effort put to improve SCC which is envisaged to be fully operational in a few years.

Future investigations envisage several important features to be accounted for. A more detailed analysis on grouping the sources' location using cluster analysis is envisaged, where a larger number of clusters should be chosen in order to pack more homogeneous regions with similar vegetation type. Thus, a more accurate correlation between the source type and the 10 measurements is envisioned. The time travel should be in some way considered. FRP will be considered to estimate the injection height and thus have more confidence that the smoke reaches the backtrajectory' altitude. The biggest challenge remains the quantification of the contribution of different fires.

*Author contributions.* MA developed the methodology and wrote the paper. All authors but MA are PIs of the stations contributing the most to EARLINET Forest Fire category. All authors contributed to revisions of the paper.

15 *Competing interests.* The authors declare that they have no conflict of interest.

*Special issue statement.* This article is part of the special issue “EARLINET, the European Aerosol Research Lidar Network. It is not associated with a conference.

20 *Acknowledgements:* We acknowledge the use of data and imagery from LANCE FIRMS operated by the NASA/GSFC/Earth Science Data and Information System (ESDIS) with funding provided by NASA/HQ. The authors gratefully acknowledge the NOAA Air Resources Laboratory (ARL) for the provision of the HYSPLIT transport and dispersion model and/or READY website (<http://www.ready.noaa.gov>) used in this publication. The authors acknowledge the EARLINET-ACTRIS community 25 for provision of the aerosol lidar profiles used in this study, in particular the PIs of all stations that provided data to the Forest Fire category in the EARLINET-ACTRIS database: A. Papayannis (Athens), A. Comeron (Barcelona), A. Pietruczuk (Belsk), D. Nicolae (Bucharest), A. Apituley (Cabauw), D. Bartoli (Evora), L. Alados-Arboledas (Granada), U. Wandinger (Leipzig), A. Chaikovsky (Minsk), I. Mattis (Observatory Hohenpeissenberg), A. Amodeo (Potenza), D. V. Stoyanov (Sofia), D. Balis (Thessaloniki), and I. S. Stachlewska (Warsaw). We acknowledge Wojciech Kumala, Lucja Janicka, Dominika 30 Szczepanik, Krzysztof Markowicz, and Rafal Fortuna (University of Warsaw) for their technical support at the ACTRIS site in Warsaw, Livio Belegante, Cristi Radu, Dragos Ene and Alexandru Dandocsi (INOE 2000) for their technical support at the ACTRIS site in Magurele.

*Funding:* The research leading to these results has received funding from the European Union Seventh Framework Programme (FP7/2007-2013) under grant agreement n° 262254, as well as the H2020 ACTRIS-2 grant n° 654109. It was

also supported with following national funding: the Romanian National contracts 18N/08.02.2019 and 19PFE/17.10.2018 as well as with the European Space Agency (ESA-ESTEC) funding: The Technical assistance for Polish Radar and Lidar Mobile Observation System (POLIMOS 4000119961/16/NL/FF/mg). The research was partially funded by the European Regional Development Fund through the Competitiveness 613 Operational Programme 2014-2020, POC-A.1-A.1.1.1-F-5 2015, project Research Centre for Environment and Earth 614 Observation CEO-Terra, SMIS code 108109, contract No. 152/2016.

Data access: The aerosol lidar profiles used in this study are available upon registration from EARLINET webpage <https://data.earin.net/earlinet/login.zul>, last access: 20191126). The FIRMS data used in the study is available upon request from <https://firms.modaps.eosdis.nasa.gov/>.

## 10 References

Adam, M., Pahlow, M., Kovalev, V. A., Ondov, J. M., Parlange, M. B., and Nair, N.: Aerosol optical characterization by nephelometer and lidar: The Baltimore Supersite experiment during the Canadian forest fire smoke intrusion, *J. Geophys. Res.*, 109, D16S02, doi:10.1029/2003JD004047, 2004.

Adam, M., Nicolae, D., Belegante, L., Stachlewska, I. S., Szczepanik, D., Mylonaki, M., Papanikolaou, C. A., Siomos, N. , 15 Voudouri, K. A., Apituley, A., Alados-Arboledas, L., Bravo-Aranda, J. A., Pietruczuk, A., Chaikovski, A., Sicard, M., Muñoz-Porcar, C., Mattis, I., Papagiannopoulos, N., Mona, L., Baars, H., Wandinger, U., Bortoli, D., Grigorov, I., Peshev, Z., Antonescu, B.: Biomass burning measurements in EARLINET, ILRC29, S25-17, Hefei, China, 2019.

Adam, M., Nicolae, D., Belegante, L., Stachlewska, I. S., Janicka, L., Szczepanik, D., Mylonaki, M., Papanikolaou, C. A., Siomos, N., Voudouri, K. A., Alados-Arboledas, L., Bravo-Aranda, J. A., Apituley, A., Papagiannopoulos, N., Mona, L., Mattis, I., Chaikovsky, A., Sicard, M., Muñoz-Porcar, C., Pietruczuk, A., Bortoli, D., Baars, H., Grigorov, I., and Peshev, Z.: Biomass burning events measured by lidars in EARLINET. Part II. Results and discussions, Atmos. Chem. Phys. Discuss., 20 https://doi.org/10.5194/acp-2020-647, in review, 2020.

Alonso-Blanco, E., Castro, A., Calvo, A. I., Pont, V., Mallet, M., Fraile, R.: Wildfire smoke plumes transport under a subsidence inversion: Climate and health implications in a distant urban area, *Sci. Total Environ.*, 619-620, 988-1002, 25 <https://doi.org/10.1016/j.scitotenv.2017.11.142>, 2018.

Ansmann, A., Riebesell, M., Wandinger, U., Weitkamp, C., Voss, E., Lahmann, W. and Michaelis, W.: Combined Raman elastic-backscatter LIDAR for vertical profiling of moisture, aerosol extinction, backscatter, and LIDAR ratio, *Appl. Phys., B* 55, 18-28, 1992.

Ansmann, A., Baars, H., Tesche, M., Müller, D., Althausen, D., Engelmann, R., Pauliquevis, T., and Artaxo, P.: Dust and 30 smoke transport from Africa to South America: Lidar profiling over Cape Verde and the Amazon rainforest, *Geophys. Res. Lett.*, 36, L11802, doi:10.1029/2009GL037923, 2009.

Ansmann, A., Baars, H., Chudnovsky, A., Mattis, I., Veselovskii, I., Haarig, M., Seifert, P., Engelmann, R., and Wandinger, U.: Extreme levels of Canadian wildfire smoke in the stratosphere over central Europe on 21–22 August 2017, *Atmos. Chem. Phys.*, 18, 11831–11845, <https://doi.org/10.5194/acp-18-11831-2018>, 2018.

Benedetti, A., Reid, J. S., Knippertz, P., Marsham, J. H., Di Giuseppe, F., Rémy, S., Basart, S., Boucher, O., Brooks, I. M., 5 Menut, L., Mona, L., Laj, P., Pappalardo, G., Wiedensohler, A., Baklanov, A., Brooks, M., Colarco, P. R., Cuevas, E., da Silva, A., Escribano, J., Flemming, J., Huneeus, N., Jorba, O., Kazadzis, S., Kinne, S., Popp, T., Quinn, P. K., Sekiyama, T. T., Tanaka, T. and Terradellas, E.: Status and future of Numerical Atmospheric Aerosol Prediction with a focus on data requirements, *Atmos. Chem. Phys.*, 18, 10615–10643, <https://doi.org/10.5194/acp-18-10615-2018>, 2018.

Bond, T. C., Doherty, S. J., Fahey, D. W., Forster, P. M., Berntsen, T., DeAngelo, B. J., Flanner, M. G., Ghan, S., Kärcher, B., 10 Koch, D., Kinne, S., Kondo, Y., Quinn, P. K., Sarofim, M. C., Schultz, M. G., Schulz, M., Venkataraman, C., Zhang, H., Zhang, S., Bellouin, N., Guttikunda, S. K., Hopke, P. K., Jacobson, M. Z., Kaiser, J. W., Klimont, Z., Lohmann, U., Schwarz, J. P., Shindell, D., Storelvmo, T., Warren, S. G., and Zender, C. S.: Bounding the role of black carbon in the climate system: A scientific assessment, *J. Geophys. Res.*, 118, 5380-5552, doi:10.1002/jgrd.50171, 2013.

Bösenberg, J., et al.: EARLINET: A European Aerosol Research Lidar Network to Establish an Aerosol Climatology. Max-15 Planck-Institut Report No. 348, 2003.

Burton, S. P., Ferrare, R. A., Hostetler, C. A., Hair, J. W., Rogers, R. R., Oblard, M. D., Butler, C. F., Cook, A. L., Harper, D. B., and Froyd, K. D.: Aerosol classification using airborne High Spectral Resolution Lidar measurements – methodology and examples, *Atmos. Meas. Tech.*, 5, 73–98, doi:10.5194/amt-5-73-2012, 2012.

Burton, S. P., Hair, J. W., Kahnert, M., Ferrare, R. A., Hostetler, C. A., Cook, A. L., Harper, D. B., Berkoff, T. A., Seaman, S. 20 T., Collins, J. E., Fenn, M. A., and Rogers, R. R.: Observations of the spectral dependence of linear particle depolarization ratio of aerosols using NASA Langley airborne High Spectral Resolution Lidar, *Atmos. Chem. Phys.*, 15, 13453–13473, doi:10.5194/acp-15-13453-2015, 2015.

D'Amico, G., Amodeo, A., Baars, H., Binietoglou, I., Freudenthaler, V., Mattis, I., Wandinger, U., and Pappalardo, G.: EARLINET Single Calculus Chain – overview on methodology and strategy, *Atmos. Meas. Tech.*, 8, 4891–4916, 25 doi:10.5194/amt-8-4891-2015, 2015.

D'Amico, G., Amodeo, A., Mattis, I., Freudenthaler, V., and Pappalardo, G.: EARLINET Single Calculus Chain – technical – Part 1: Pre-processing of raw lidar data, *Atmos. Meas. Tech.*, 9, 491–507, doi:10.5194/amt-9-491-2016, 2016.

Ancellet, G., Pelon, J., Totems, J., Chazette, P., Bazureau, A., Sicard, M., Di Iorio, T., Dulac, F., and Mallet, M.: Long-range 30 transport and mixing of aerosol sources during the 2013 North American biomass burning episode: analysis of multiple lidar observations in the western Mediterranean basin, *Atmos. Chem. Phys.*, 16, 4725–4742, doi:10.5194/acp-16-4725-2016, 2016.

Davies, D. K., Ilavajhala, S., Wong, M. M., and Justice, C. O.: Fire Information for Resource Management System: Archiving and Distributing MODIS Active Fire Data, *IEEE TRANSACTIONS ON GEOSCIENCE AND REMOTE SENSING*, VOL. 47, NO. 1, 72-79, doi:10.1109/TGRS.2008.2002076, 2009.

Fiebig, M., Petzold, A., Wandinger, U., Wendisch, M., Kiemle, C., Stifter, A., Ebert, M., Rother, T., and Leiterer, U.: Optical closure for an aerosol column: Method, accuracy, and inferable properties applied to a biomass-burning aerosol and its radiative forcing, *J. Geophys. Res.*, VOL. 107, NO. D21, 8130, doi:10.1029/2000JD000192, 2002.

Fiebig, M., Stohl, A., Wendisch, M., Eckhardt, S., and Petzold, A.: Dependence of solar radiative forcing of forest fire aerosol on ageing and state of mixture, *Atmos. Chem. Phys.*, 3, 881–891, 2003, [www.atmos-chem-phys.org/acp/3/881/](http://www.atmos-chem-phys.org/acp/3/881/).

Giannakaki, E., Pfüller, A., Korhonen, K., Mielonen, T., Laakso, L., Vakkari, V., Baars, H., Engelmann, R., Beukes, J. P., Van Zyl, P. G., Josipovic, M., Tiipta, P., Chiloane, K., Piketh, S., Lihavainen, H., Lehtinen, K. E. J., and Komppula, M.: One year of Raman lidar observations of free-tropospheric aerosol layers over South Africa, *Atmos. Chem. Phys.*, 15, 5429–5442, doi:10.5194/acp-15-5429-2015, 2015.

Giglio, L., Schroeder, W., Justice, C. O.: The collection 6 MODIS active fire detection algorithm and fire products, *Rem. Sens. Environ.*, 178, 31-41, <http://dx.doi.org/10.1016/j.rse.2016.02.054>, 2016.

Gross, S., Esselborn, M., Weinzierl, B., Wirth, M., Fix, A., and Petzold, A.: Aerosol classification by airborne high spectral resolution lidar Observations, *Atmos. Chem. Phys.*, 13, 2487–2505, doi:10.5194/acp-13-2487-2013, 2013.

Haarig, M., Ansmann, A., Baars, H., Jimenez, C., Veselovskii, I., Engelmann, R., and Althausen, D.: Depolarization and lidar ratios at 355, 532, and 1064 nm and microphysical properties of aged tropospheric and stratospheric Canadian wildfire smoke, *Atmos. Chem. Phys.*, 18, 11847-11861, <https://doi.org/10.5194/acp-18-11847-2018>, 2018.

Haarig M., Baars, H., Ansmann, A., Engelmann, R., Ohneiser, K., Jimenez, C., Althausen, D., Bühl, J., Seifert, P., Mamouri, R., Nisantzi, A.: Wildfire smoke in the stratosphere over Europe – first measurements of depolarization and lidar ratios at 355, 532, and 1064 nm, ILRC 29, S2-232, Hefei, China, 2019.

Heese, B., and Wiegner, M.: Vertical aerosol profiles from Raman polarization lidar observations during the dry season AMMA field campaign, *J. Geophys. Res.*, 113, D00C11, doi:10.1029/2007JD009487, 2008.

Hu, Q., Goloub, P., Veselovskii, I., Bravo-Aranda, J.-A., Popovici, I., Podvin, T., Haeffelin, M., Lopatin, A., Pietras, C., Huang, X., Torres, B., and Chen, C.: A study of long-range transported smoke aerosols in the Upper Troposphere/Lower Stratosphere, *Atmos. Chem. Phys.*, 19, 1173–1193, <https://doi.org/10.5194/acp-19-1173-2019>, 2019.

IPCC: *Climate Change 2013: The Physical Science Basis. Contribution of Working Group I to the Fifth Assessment Report of the Intergovernmental Panel on Climate Change* [Stocker, T.F., D. Qin, G.-K. Plattner, M. Tignor, S.K. Allen, J. Boschung, Nauels, A., Xia, Y., Bex, V. and Midgley, P.M. (eds.), Cambridge University Press, Cambridge, United Kingdom and New York, NY, USA, 1535 pp, 2013.

Janicka, L., Stachlewska, I. S., Veselovskii, I., Baars, H.: Temporal variations in optical and microphysical properties of mineral dust and biomass burning aerosol derived from daytime Raman lidar observations over Warsaw, Poland, *Atmos. Environ.*, 169, 162-174, <http://dx.doi.org/10.1016/j.atmosenv.2017.09.022>, 2017.

Janicka, L., Bockmann, C., Wang, D., Stachlewska, I. S.: Lidar derived fine scale resolution properties of tropospheric aerosol mixtures, ILRC29, S2-122, Hefei, China, 2019.

Janicka, L. and Stachlewska, I. S.: Properties of biomass burning aerosol mixtures derived at fine temporal and spatial scales from Raman lidar measurements: Part I optical properties, *Atmos. Chem. Phys. Discuss.*, <https://doi.org/10.5194/acp-2019-207>, 2019.

Lolli, S., Khor, W. Y., Matjafri, M. Z. and Lim, H. S.: Monsoon Season Quantitative Assessment of Biomass Burning Clear-  
5 Sky Aerosol Radiative Effect at Surface by Ground-Based Lidar Observations in Pulau Pinang, Malaysia in 2014, *Remote Sens.*, **11**, 2660, doi:10.3390/rs11222660, 2019.

Mariano, G. L., Lopes, F. J. S., Jorge, M. P. P. M., Landulfo, E.: Assessment of biomass burnings activity with the synergy of sunphotometric and LIDAR measurements in São Paulo, Brazil, *Atmos. Res.*, **98**, 486-499, doi:10.1016/j.atmosres.2010.08.025, 2010.

10 Markowicz, K. M., Chilinski, M. T., Lisok, J., Zawadzka, O., Stachlewska, I. S., Janicka, L., Rozwadowska, A., Makuch, P., Pakszys, P., Zielinski, T., Petelski, T., Posyniak, M., Pietruczuk, A., Szkop, A., Westphal, D. L.: Study of aerosol optical properties during long-range transport of biomass burning from Canada to Central Europe in July 2013, *J. Aerosol Sci.*, **101**, 156-173, DOI: 10.1016/j.jaerosci.2016.08.006, 2016.

Mattis, I., Müller, D., Ansmann, A., Wandinger, U., Preißler, J., Seifert, P., and Tesche, M.: Ten years of multiwavelength Raman lidar observations of free-tropospheric aerosol layers over central Europe: Geometrical properties and annual cycle, *J. Geophys. Res.*, **113**, D20202, doi:10.1029/2007JD009636, 2008.

Mattis, I., D'Amico, G., Baars, H., Amodeo, A., Madonna, F., and Iarlori, M.: EARLINET Single Calculus Chain – technical – Part 2: Calculation of optical products, *Atmos. Meas. Tech.*, **9**, 3009–3029, doi:10.5194/amt-9-3009-2016, 2016.

20 Müller, D., Mattis, I., Wandinger, U., Ansmann, A., Althausen, D., and Stohl, A.: Raman lidar observations of aged Siberian and Canadian forest fire smoke in the free troposphere over Germany in 2003: Microphysical particle characterization, *J. Geophys. Res.*, **110**, D17201, doi:10.1029/2004JD005756, 2005.

Müller, D., Ansmann, A., Mattis, I., Tesche, M., Wandinger, U., Althausen, D., and Pisani, G.: Aerosol-type-dependent lidar ratios observed with Raman lidar, *J. Geophys. Res.*, **112**, D16202, doi:10.1029/2006JD008292, 2007.

25 Müller, D., Ansmann, A., Mattis, I., Tesche, M., Wandinger, U., Althausen, D., and Pisani, G.: Aerosol-type-dependent lidar ratios observed with Raman lidar, *J. Geophys. Res.*, **112**, D16202, doi:10.1029/2006JD008292, 2007.

Müller, D., Kolgotin, A., Mattis, I., Petzold, A., and Stohl, A., Vertical profiles of microphysical particle properties derived from inversion with two-dimensional regularization of multiwavelength Raman lidar data: experiment, *Appl. Opt.*, **50**, 2069-2079, 2011.

30 Müller, D., Böckmann C., Kolgotin, A., Schneidenbach, L., Chemyakin, E., Rosemann, J., Znak, P., and Romanov, A.: Microphysical particle properties derived from inversion algorithms developed in the framework of EARLINET, *Atmos. Meas. Tech.*, **9**, 5007–5035, <https://doi.org/10.5194/amt-9-5007-2016>, 2016.

Murayama, T., Müller, D., Wada, K., Shimizu, A., Sekiguchi, M., and Tsukamoto, T.: Characterization of Asian dust and Siberian smoke with multiwavelength Raman lidar over Tokyo, Japan in spring 2003, *Geophys. Res. Lett.*, **31**, L23103, doi:10.1029/2004GL021105, 2004.

Myhre, G., Samset, B. H., Schulz, M., Balkanski, Y., Bauer, S., Berntsen, T. K., Bian, H., Bellouin, N., Chin, M., Diehl, T., Easter, R. C., Feichter, J., Ghan, S. J., Hauglustaine, D., Iversen, T., Kinne, S., Kirkevåg, A., Lamarque, J.-F., Lin, G., Liu, X., Lund, M. T., Luo, G., Ma, X., van Noije, T., Penner, J. E., Rasch, P. J., Ruiz, A., Seland, Ø., Skeie, R. B., Stier, P., Takemura, T., Tsigaridis, K., Wang, P., Wang, Z., Xu, L., Yu, H., Yu, F., Yoon, J.-H., Zhang, K., Zhang, H., and Zhou, C.: Radiative forcing of the direct aerosol effect from AeroCom Phase II simulations, *Atmos. Chem. Phys.*, 13, 1853–1877, doi:10.5194/acp-13-1853-2013, 2013.

Mylonaki, M., Papayannis, A., Mamouri, R., Argyrouli, A., Kokkalis, P., Tsaknakis, G., and Soupiona, O.: Aerosol optical properties variability during biomass burning events observed by the EOULE-AIAS depolarization lidars over Athens, Greece (2007-2016), 28<sup>th</sup> ILRC, Bucharest, Romania, 2017.

Nicolae, D., Nemuc, A., Müller, D., Talianu, C., Vasilescu, J., Belegante, L., and Kolgotin, A.: Characterization of fresh and aged biomass burning events using multiwavelength Raman lidar and mass spectrometry, *J. Geophys. Res. Atmos.*, 118, 2956–2965, doi:10.1002/jgrd.50324, 2013.

Nicolae, D., Vasilescu, J., Talianu, C., Binietoglou, I., Nicolae, V., Andrei, S., and Antonescu, B.: A Neural Network Aerosol Typing Algorithm Based on Lidar Data, *Atmos. Chem. Phys.*, 18, 14511–14537, <https://doi.org/10.5194/acp-18-14511-2018>, 2018.

Nicolae, V., Talianu, C., Andrei, S., Antonescu, B., Ene, D., Nicolae, D., Dandocsi, A., Toader, V. E., Stefan, S., Savu, T. and Vasilescu, J.: Multiyear typology of long-range transported aerosols over Europe, *Atmosphere*, 10, 482, doi:10.3390/atmos10090482, 2019.

Ortiz-Amezcua, P., Guerrero-Rascado, J. L., Granados-Muñoz, M. J., Benavent-Oltra, J. A., Böckmann, C., Samaras, S., Stachlewska, I. S., Janicka, Ł., Baars, H., Bohlmann, S., and Alados-Arboledas, L.: Microphysical characterization of long-range transported biomass burning particles from North America at three EARLINET stations, *Atmos. Chem. Phys.*, 17, 5931–5946, doi:10.5194/acp-17-5931-2017, 2017.

Pahlow, M., Kleissl, J., Parlange, M. B., Ondov, J. M. and Harrison, D.: Atmospheric boundary-layer structure observed during a haze event due to forest-fire smoke, *BLM*, 114, 53-70, 2005.

Pappalardo, G., Amodeo, A., Apituley, A., Comeron, A., Freudenthaler, V., Linné, H., Ansmann, A., Bösenberg, J., D'Amico, G., Mattis, I., Mona, L., Wandinger, U., Amiridis, V., Alados-Arboledas, L., Nicolae, D., and Wiegner, M.: EARLINET: towards an advanced sustainable European aerosol lidar network, *Atmos. Meas. Tech.*, 7, 2389–2409, doi:10.5194/amt-7-2389-2014, 2014.

Peterson, D. A., Campbell, J. R., Hyer, E. J., Fromm, M. D., Kablick III, G. P., Cossuth, J. H. and DeLand, M. T.: Wildfire-driven thunderstorms cause a volcano-like stratospheric injection of smoke, *Climate Atmos. Science*, 1:30, doi:10.1038/s41612-018-0039-3, 2018.

Preißler, J., Wagner, F., Guerrero-Rascado, J. L., and Silva, A. M.: Two years of free-tropospheric aerosol layers observed over Portugal by lidar, *J. GEOPHYS. RES.*, 118, 3676–3686, doi:10.1002/jgrd.50350, 2013.

Prenni, A., DeMott, P. J., Sullivan, A. P., Sullivan, R. C., Kreidenweiss, S. M., and Rogers, D. C.: Biomass burning as a potential source for atmospheric ice nuclei: Western wildfires and prescribed burns, *Gephys. Res. Lett.*, **39**, L11805, doi:10.1029/2012GL051915, 2012.

Reid, J. S., and Hobbs, P. V.: Physical and optical properties of young smoke from individual biomass fires in Brazil, *J. Geophys. Res.*, **103**, 32013-32030, 1998.

Reid, J. S., Eck, T. F. , Christopher, S. A., Koppmann, R., Dubovik, O., Eleuterio, D. P., Holben, B. N., Reid, E. A., and Zhang, J.: A review of biomass burning emissions part III: intensive optical properties of biomass burning particles, *Atmos. Chem. Phys.*, **5**, 827–849, 2005, [www.atmos-chem-phys.org/acp/5/827/](http://www.atmos-chem-phys.org/acp/5/827/).

Rolph, G., Stein, A., Stunder, B.: Real-time Environmental Applications and Display sYstem: READY, *Environ. Modelling Soft.*, **95**, 210-228, <https://doi.org/10.1016/j.envsoft.2017.06.025>, 2017.

Samaras, S., Nicolae, D., Böckmann, C., Vasilescu, J., Binietoglou, I., Labzovskii, L., Toanca, F., Papayannis, A.: Using Raman-lidar-based regularized microphysical retrievals and Aerosol Mass Spectrometer measurements for the characterization of biomass burning aerosols, *Journal of Computational Physics* **299**, 156–174, <http://dx.doi.org/10.1016/j.jcp.2015.0>, 2015.

San-Miguel-Ayanz, J., Durrant, T., Boca, R., Libertà, G., Branco, A., de Rigo, D., Ferrari, D., Maianti, P., Artés Vivancos, T., Costa, H., Lana, F., Löffler, P., Nuijten, D., Ahlgren, A. C., Leray, T: Forest Fires in Europe, Middle East and North Africa 2017. EUR 29318 EN, ISBN 978-92-79-92831-4, doi: 10.2760/663443, 2018.

Sapkota, A., Symons, J. M., Kleissl, J., Wang, L., Parlange, M. B., Ondov, J., Breysse, P. N., Diette, G. B., Eggleston, P. A., and Buckley, T.: Impact of the 2002 Canadian Forest Fires on Particulate Matter Air Quality in Baltimore City, *Environ. Sci. Technol.*, **39**, 24-32, 2005.

Sicard, M., Granados-Muñoz, M.J., Alados-Arboledas, L., Barragán, R., Bedoya-Velásquez, A.E., Benavent-Oltra, J.A., Bortoli, D., Comerón, A., Córdoba-Jabonero, C., Costa, M.J., del Águila, A., Fernández, A.J., Guerrero-Rascado, J.L., Jorba, O., Molero, F., Muñoz-Porcar, C., Ortiz-Amezcua, P., Papagiannopoulos, N., Potes, M. , Pujadas, M., Rocadenbosch, F., Rodríguez-Gómez, A., Román, R., Salgado, R., Salgueiro, V., Sola, Y., Yela, M.: Ground/space, passive/active remote sensing observations coupled with particle dispersion modelling to understand the inter-continental transport of wildfire smoke plumes, *Remote Sens Environ.*, **232**, 111294, <https://doi.org/10.1016/j.rse.2019.111294>, 2019.

Stachlewska, I. S., Samson, M., Zawadzka, O., Harendta, K. M., Janicka, L., Poczta, P., Szczepanik, D., Heese, B., Wang, D., Borek, K., Tetoni, E., Proestakis, E., Siomos, N., Nemuc, A., Chojnicki, B. H., Markowicz, K. M., Pietruczuk, A., Szkop, A., Althausen, D., Stebel, K., Schuettemeyer, D. and Zehner, C.: Modification of Local Urban Aerosol Properties by Long-Range Transport of Biomass Burning Aerosol, *Remote Sens.*, **10**, 412; doi:10.3390/rs10030412, 2018.

Stein, A.F., Draxler, R.R, Rolph, G.D., Stunder, B.J.B., Cohen, M.D., and Ngan, F.: NOAA's HYSPLIT atmospheric transport and dispersion modeling system, *Bull. Amer. Meteor. Soc.*, **96**, 2059-2077, <http://dx.doi.org/10.1175/BAMS-D-14-00110.1>, 2015.

Su, W., Schuster, G. L., Loeb, N. G., Rogers, R. R., Ferrare, R. A., Hostetler, C. A., Hair, J. W., and Oblad, M. D.: Aerosol and cloud interaction observed from high spectral resolution lidar data, *J. Geophys. Res.*, 113, doi:10.1029/2008JD010588 (2008)

Su, L., Yuan, Z., Fung, J. C. H., Lau, A. K. H.: A comparison of HYSPLIT backward trajectories generated from two GDAS datasets, *Sci. Total Environ.*, 506-507, 527-537, <http://dx.doi.org/10.1016/j.scitotenv.2014.11.072>, 2015.

Sugimoto, N., Tatarov, B., Shimizu, A., Matsui, I., and Nishizawa, T.: Optical Characteristics of Forest-Fire Smoke Observed with Two-Wavelength Mie-Scattering Lidars and a High-Spectral-Resolution Lidar over Japan, *SOLA*, 6, 093–096, doi:10.2151/sola.2010-024, 2010.

Tesche, M., Müller, D., Gross, S., Ansmann, A., Althausen, D., Freundenthaler, V., Weinzierl, B., Veira, A. and Petzold, A.: Optical and microphysical properties of smoke over Cape Verde inferred from multiwavelength lidar measurements, *Tellus*, 63B, 677-694, DOI: 10.1111/j.1600-0889.2011.00549.x, 2011.

van Drooge, B. L., Sicard, M., Stohl, A., Fontal, M., Bravo, N., Muñoz, A., Lange, D., Fernández, P., Grimalt, J. O.: Detection and simulation of wildfire smoke impacting a Mediterranean urban atmosphere, *Atmos. Poll. Res.*, 7, 494-502, <http://dx.doi.org/10.1016/j.apr.2015.12.003>, 2016.

Vaughan, G., Draude, A. P., Ricketts, H. M. A., Schultz, D. M., Adam, M., Sugier, J. and Wareing, D. P.: Transport of Canadian forest fire smoke over the UK as observed by lidar, *Atmos. Chem. Phys.*, 18, 11375–11388, <https://doi.org/10.5194/acp-18-11375-2018>, 2018.

Veselovskii, I., Whiteman, D. N., Korenskiy, M., Suvorina, A., Kolgotin, A., Lyapustin, A., Wang, Y., Chin, M., Bian, H., Kucsera, T. L., Pérez-Ramírez, D. and Holben, B.: Characterization of forest fire smoke event near Washington, DC in summer 2013 with multi-wavelength lidar, *Atmos. Chem. Phys.*, 15, 1647–1660, doi:10.5194/acp-15-1647-2015, 2015.

Veselovskii, I., Goloub, P., Podvin, T., Tanre, D., da Silva, A., Colarco, P., Castellanos, P., Korenskiy, M., Hu, Q., Whiteman, D. N., Pérez-Ramírez, D., Augustin, P., Fourmentin, M. and Kolgotin, A.: Characterization of smoke and dust episode over West Africa: comparison of MERRA-2 modeling with multiwavelength Mie–Raman lidar observations, *Atmos. Meas. Tech.*, 11, 949–969, <https://doi.org/10.5194/amt-11-949-2018>, 2018.

Wandinger, U., Müller, D., Böckmann, C., Althausen, D., Matthias, V., Bösenberg, J., Weiß, V., Fiebig, M. Wendisch, M., Stohl, A. and Ansmann, A.: Optical and microphysical characterization of biomassburning and industrial-pollution aerosols from multiwavelength lidar and aircraft measurements, *J. Geophys. Res.*, 107, NO. D21, 8125, doi:10.1029/2000JD000202, 2002.

Wang D., Szczepanik, D. and Stachlewska, I. S.: Interrelations between surface, boundary layer, and columnar aerosol properties derived in summer and early autumn over a continental urban site in Warsaw, Poland, *Atmos. Chem. Phys.*, 19, 13097-13128, <https://doi.org/10.5194/acp-19-13097-2019>, 2019.

Wiegner, M.: EARLINET: towards an advanced sustainable European aerosol lidar network, *Atmos. Meas. Tech.*, 7, 2389–2409, doi:10.5194/amt-7-2389-2014, 2014.

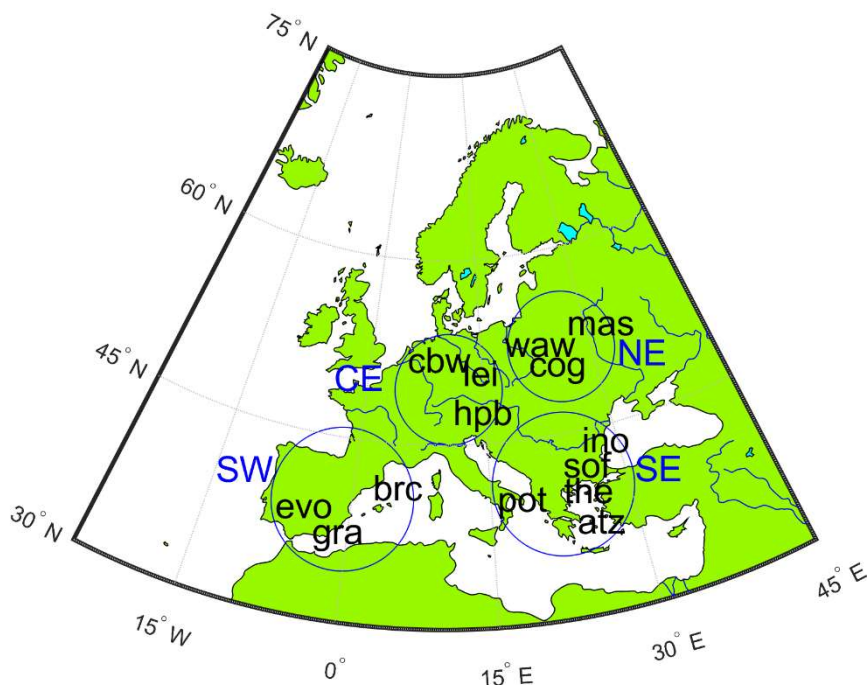
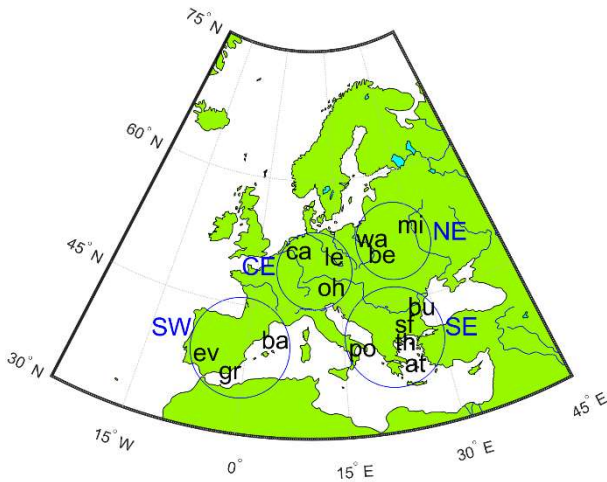
Yu, S., Role of organic acids formic, acetic, pyruvic and oxalic in the formation of cloud condensation nuclei CCN: a review, *Atmos. Res.*, 53, 185-217, 2000.

Zhang, J., Reid, J. S., Christensen, M. and Benedetti, A.: An evaluation of the impact of aerosol particles on weather forecasts from a biomass burning aerosol event over the Midwestern United States: observational-based analysis of surface temperature, 5 *Atmos. Chem. Phys.*, 16, 6475–6494, doi:10.5194/acp-16-6475-2016, 2016.

10

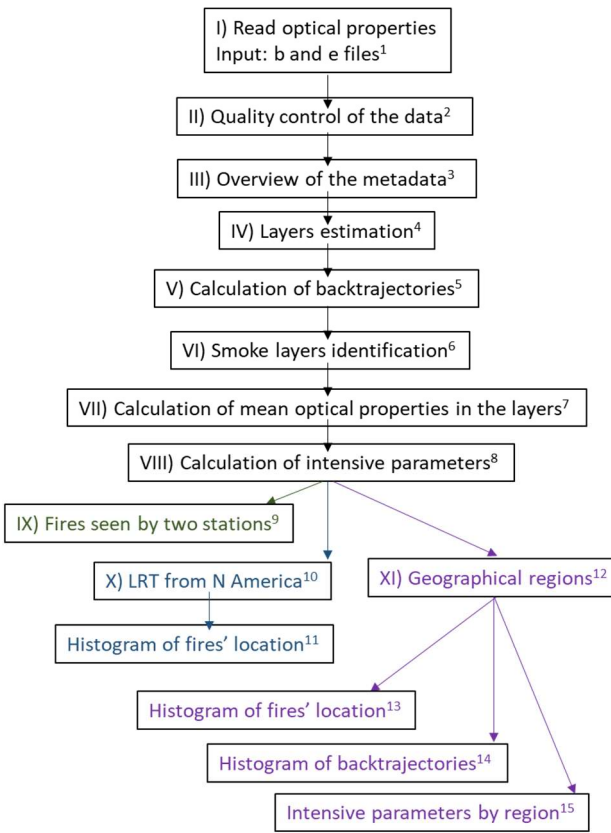
15

20



5 Fig. 1. The geographical location of the 14 stations proving data for Forest Fire category in EARLINET database over 2008-2017 period. The stations are located in Athens (“atzat”), Barcelona (“brcba”), Belsk (“cogbe”), Bucharest (“inobu”), Cabauw (“cbwea”), Evora (“evoev”), Granada (“grage”), Leipzig (“leile”), Minsk (“masmi”), Observatory Hohenpeissenberg (“hpboh”), Potenza (“potpo”), Sofia (“sofsof”), Thessaloniki (“thebh”) and Warsaw (“wawwa”). The blue circles show the four European geographical regions: South East (SE), South West (SW), North East (NE) and Central (CE).





<sup>1</sup> 3589 input files; see Figs. 3, 4 and Table 1

<sup>2</sup> EARLINET/Forest Fire files checked following EARLINET criteria; additional in-house checks

<sup>3</sup> e.g. detection mode, evaluation method, raw resolution; see Table 2.

<sup>4</sup> algorithm developed; non-accurate estimates were manually corrected; 1901 layers calculated for 960 time stamps

<sup>5</sup> run Hysplit, 10 days backwards; use GDAS0.5° (23 cases on GDAS1°)

<sup>6</sup> use Hysplit backtrajectory and fires emissions (FIRMS); 1053 layers for 677 time stamps were considered as having BB origin; see Table 3, columns 5-6.

<sup>7</sup> the average in the layer is calculated if at least 90% data is available; the averages for which SNR<2 were dismissed; there were 1050 layers for 676 time stamps for which at least one average optical property was calculated; see Table 3, columns 7-8, e.g. Fig. 7.

<sup>8</sup> e.g. Fig. 9; literature review on intensive parameters (Fig. S1 and Table S1). Values outside the range of acceptable values are dismissed. Remaining IPs are considered further (795 layers, 526 time stamps). See Table 4, columns 9-10.

<sup>9</sup> based on backtrajectories, the common fires (smoke measured by two stations) were identified; compares IPs; measured smoke can be of "single fire" or "mixed fires". See Figs. 10-11.

<sup>10</sup> based on backtrajectories, the measured smoke can be "pure N America" or "mixed" (N America + local); smoke was measured by single station or several stations; e.g. smoke measured by one station Figs. 12-13; statistics over LRT from N America to be shown in second part of the paper.

<sup>11</sup> by station; e.g. Fig. 12.

<sup>12</sup> region: SE ("atz","ino","pot","the"), NE ("cog","mas","waw"), SW ("brc","evo","gra"), CE ("cbw","lei","hpb")

<sup>13</sup> by station; e.g. Figs. 14 for SE region.

<sup>14</sup> main circulation pattern revealed for some regions.

<sup>15</sup> IPs are classified based on smoke' continental origin (Europe, N America, Asia, Africa or a mixture of them). Mean values and scatter plots are considered. Fig. 15 for SE region.

<sup>1</sup> 3589 input files; see Figs. 3, 4 and Table 1

<sup>2</sup> EARLINET/Forest Fire files checked following EARLINET criteria; additional in-house checks

<sup>3</sup> e.g. detection mode, evaluation method, raw resolution; see Table 2.

<sup>4</sup> algorithm developed; non-accurate estimates were manually corrected; 1901 layers calculated for 960 time stamps

<sup>5</sup> run Hysplit, 10 days backwards; use GDAS0.5° (23 cases on GDAS1°)

<sup>6</sup> use Hysplit backtrajectory and fires emissions (FIRMS); 1053 layers for 677 time stamps were considered as having BB origin; see Table 3, columns 5-6.

<sup>7</sup> the average in the layer is calculated if at least 90% data is available; the averages for which SNR<2 were dismissed; there were 1050 layers for 676 time stamps for which at least one average optical property was calculated; see Table 3, columns 7-8, e.g. Fig. 7.

<sup>8</sup> e.g. Fig. 9; literature review on intensive parameters (Fig. S1 and Table S1). Values outside the range of acceptable values are dismissed. Remaining IPs are considered further (795 layers, 526 time stamps). See Table 4, columns 9-10.

<sup>9</sup> based on backtrajectories, the common fires (smoke measured by two stations) were identified; compares IPs; measured smoke can be of "single fire" or "mixed fires". See Figs. 10-11.

<sup>10</sup> based on backtrajectories, the measured smoke can be "pure N America" or "mixed" (N America + local); smoke was measured by single station or several stations; e.g. smoke measured by one station Figs. 12-13; statistics over LRT from N America to be shown in second part of the paper.

<sup>11</sup> by station; e.g. Fig. 12.

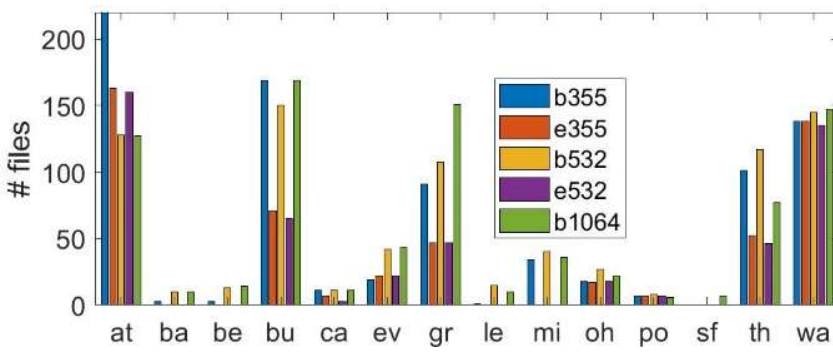
<sup>12</sup> region: SE ('at','bu','po','th'), NE ('be','mi','wa'), SW ('ba','ev','gr'), CE ('ca','le','oh')

<sup>13</sup> by station; e.g. Figs. 14 for SE region.

<sup>14</sup> main circulation pattern revealed for some regions.

<sup>15</sup> IPs are classified based on smoke' continental origin (Europe, N America, Asia, Africa or a mixture of them). Mean values and scatter plots are considered. Fig. 15 for SE region.

**Fig. 2. Methodology diagram.**



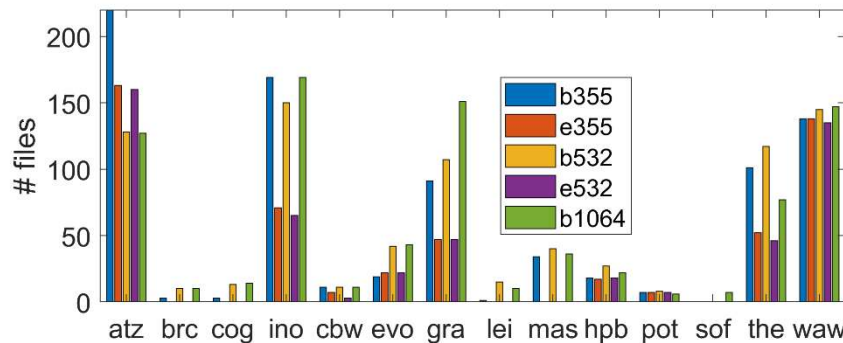
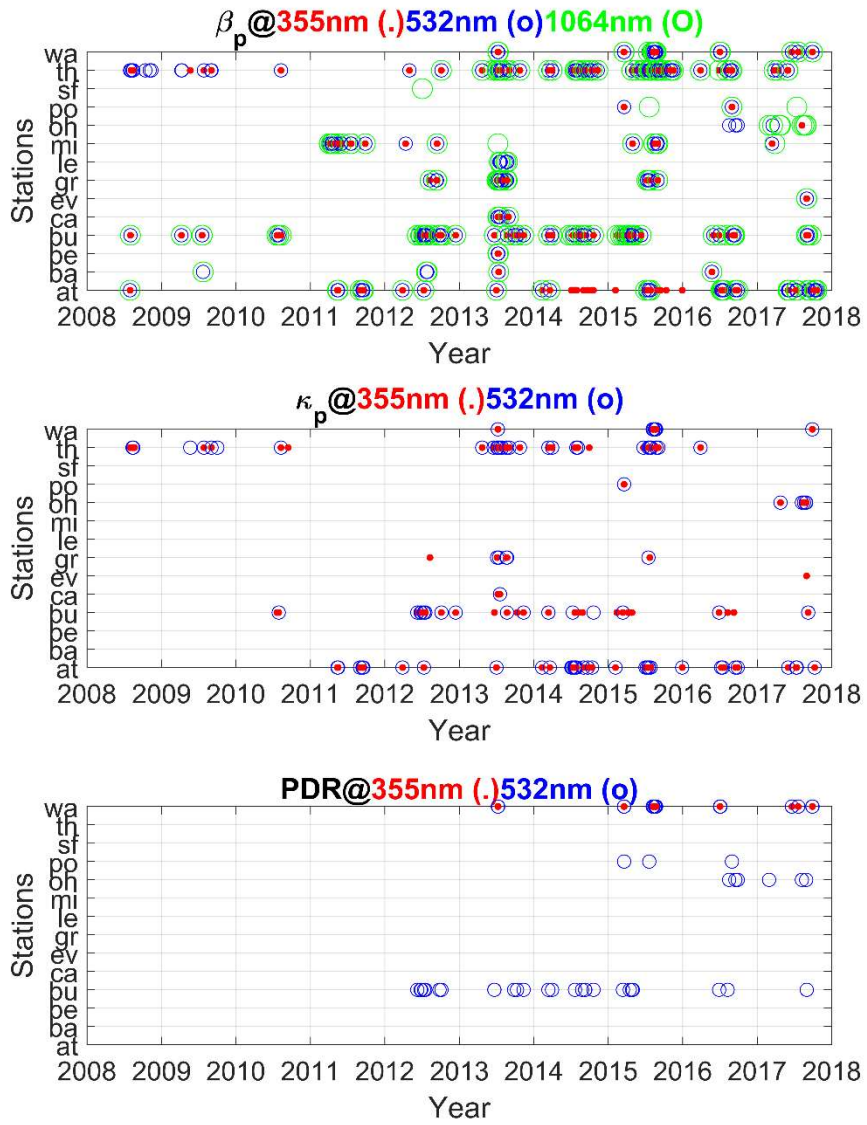


Fig. 3. Number of “b” and “e” files available from 14 EARLINET stations providing data for Forest Fire over 2008-2017 period.



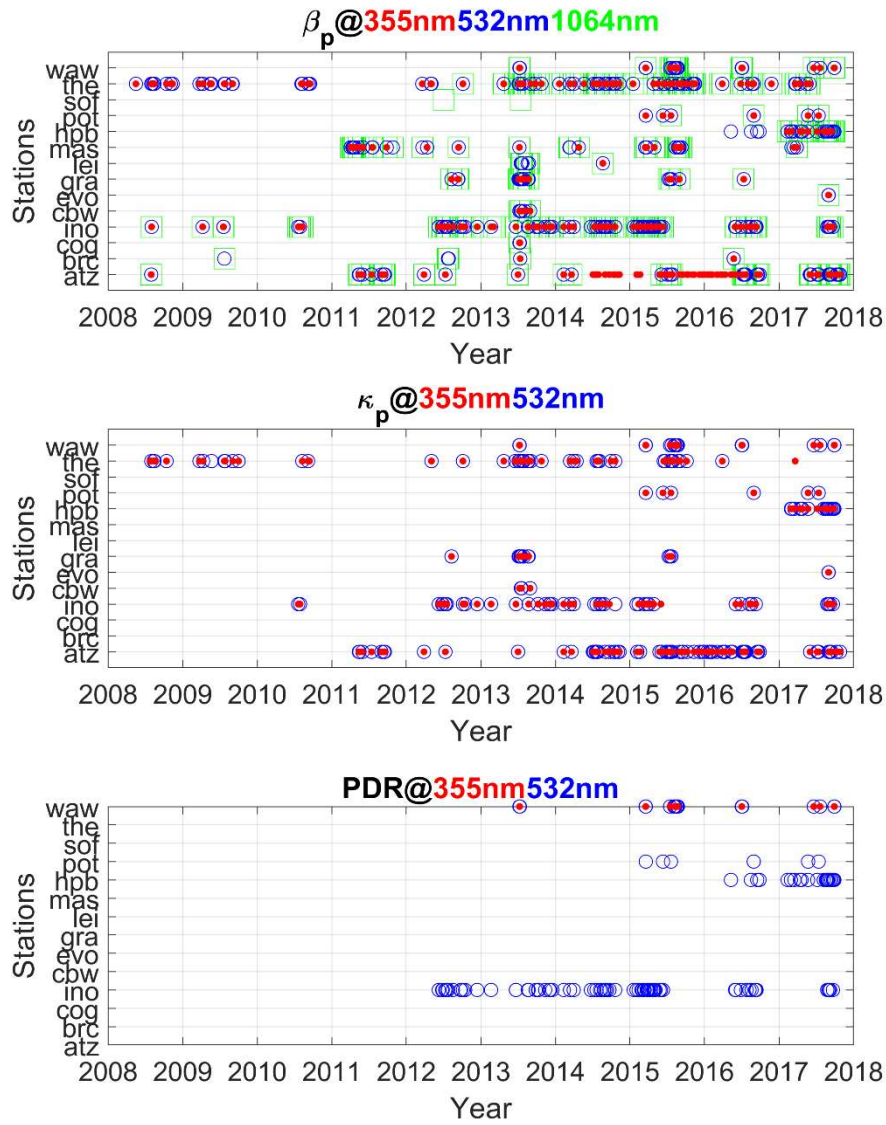
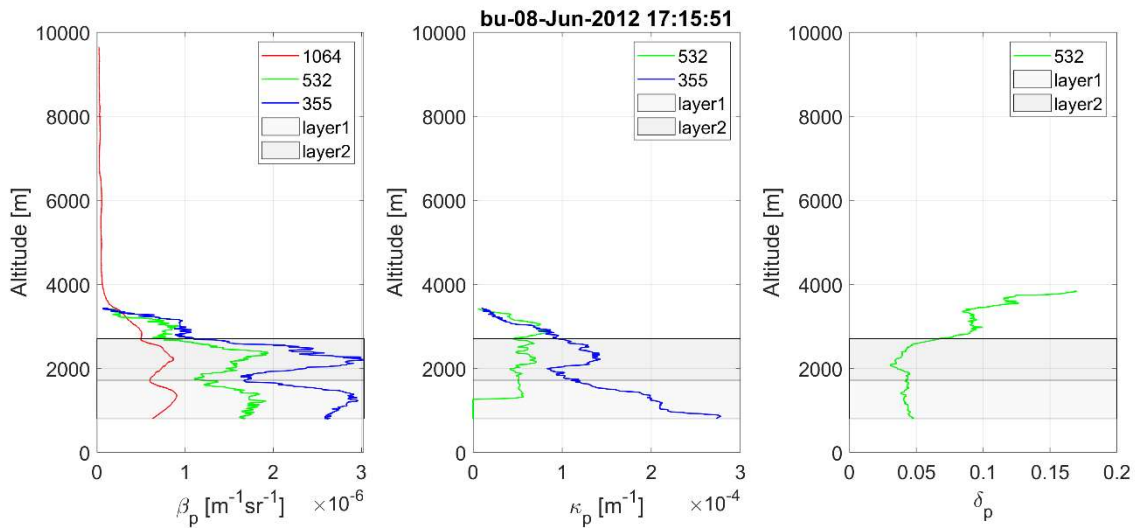
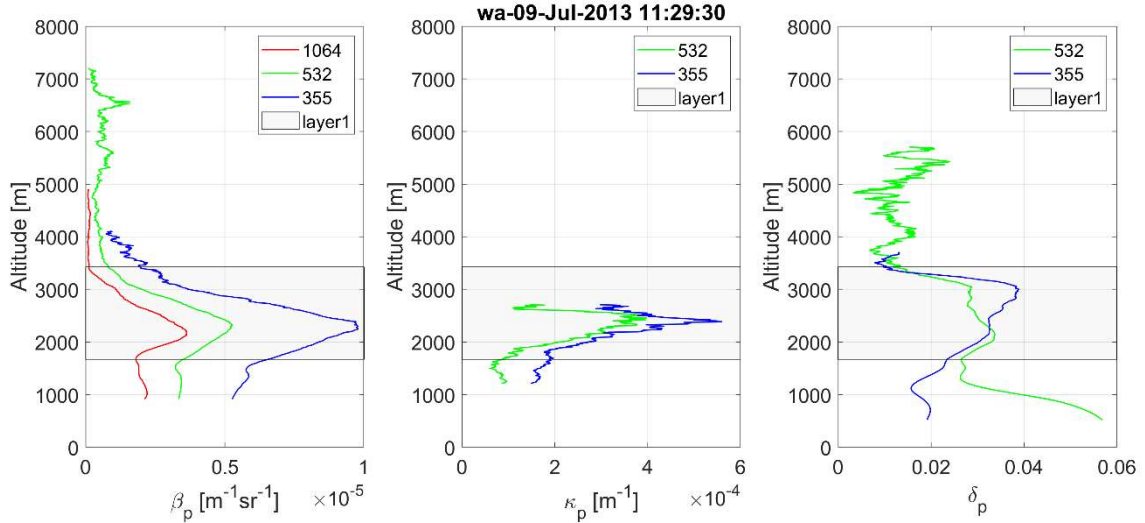


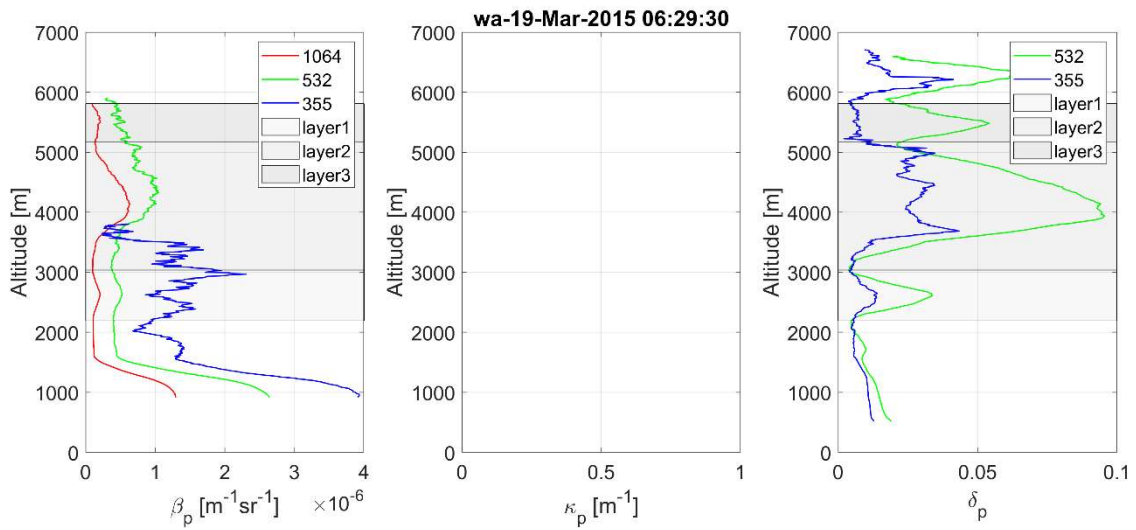
Fig. 4. Time span of the available particles backscatter coefficient (top), extinction coefficient (middle) and depolarization ratio (bottom) for each station, over 2008-2017 period, for the smoke layers.



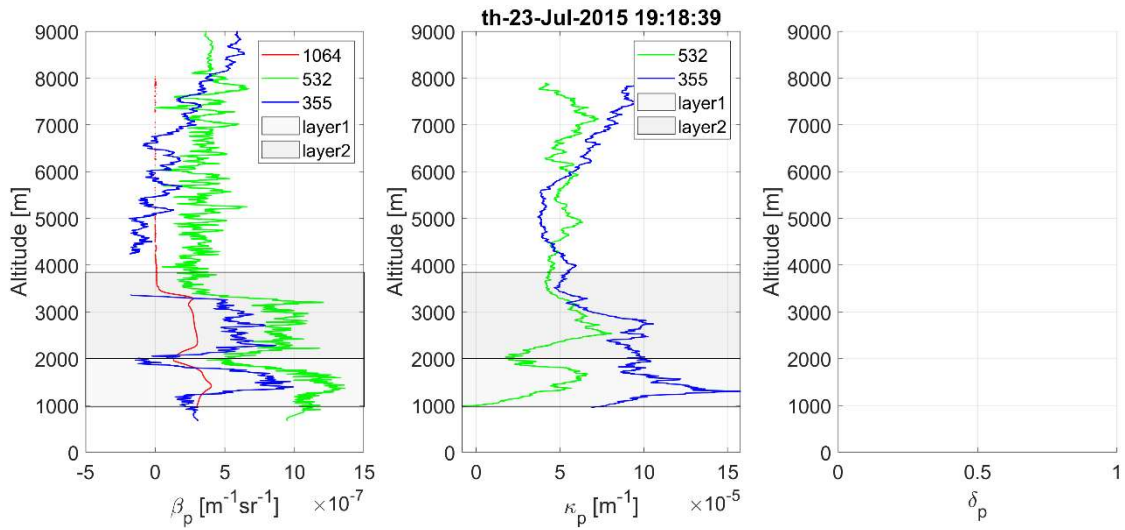
a) Two layers automatically selected based on  $\beta_{1064}$  signal. Layers' boundaries are: [802 1717] m and [1717 2707] m.



b) One layer automatically selected based on  $\beta_{1064}$  signal. Layer' boundaries are [1670 3426] m.

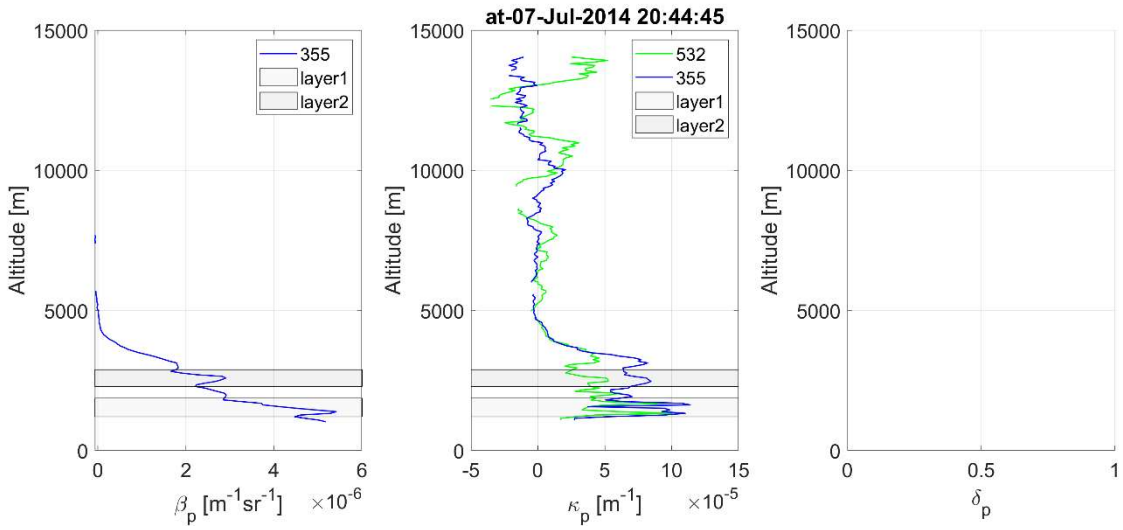


e) Three layers automatically selected based on  $\beta_{1064}$  signal. Layers' boundaries are [2193 3037] m, [3037 5166] m and [5166 5809] m.

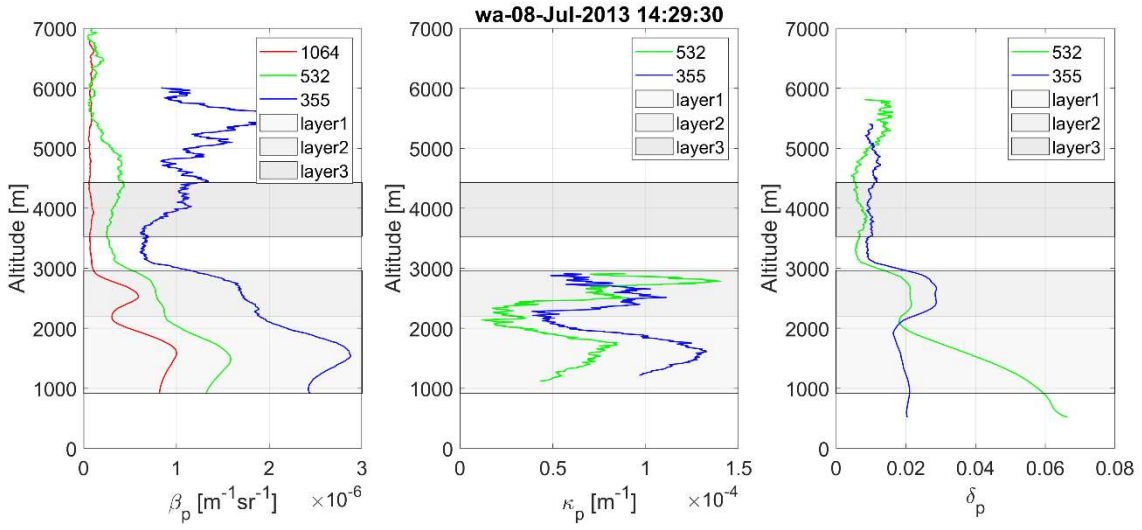


5

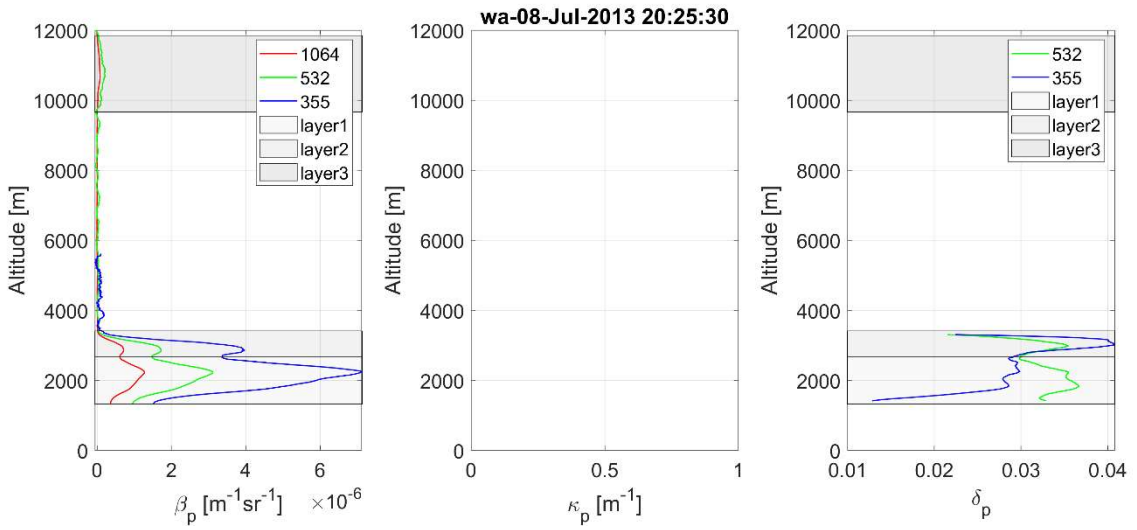
d) Two layers automatically selected based on  $\beta_{1064}$  signal. Layers' boundaries are [968 2002] m and [2002 3847] m.



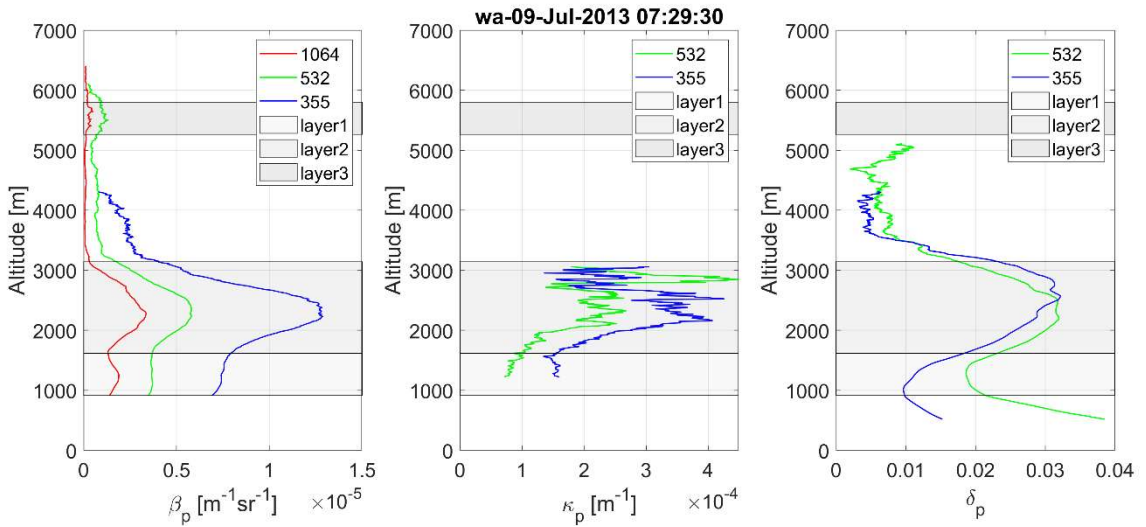
e) Two layers automatically selected, based on  $\beta_{355}$  signal. Layers' boundaries are [1202 1862] m and [2282 2882] m.



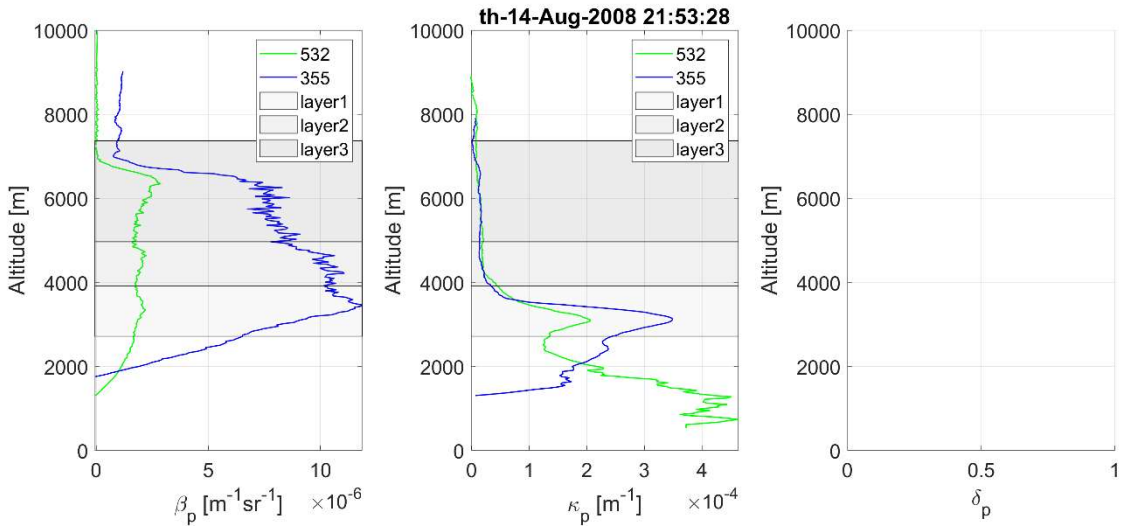
f) Three layers selected based on  $\beta_{1064}$  signal. Layers' boundaries are [915 2193] m, [2193 2962] m and [3530 4427] m. The top of the second layer was manually changed from 3530 m to 2962 m. A fourth layer around 6500m was dismissed.



g) Three layers selected based on  $\beta_{1064}$  signal. Layers' boundaries are [1319 2678] m, [2678 3411] m and [9664 11846] m. The third layer was added manually. The top of the second layer was modified from 4061 m to 3411 m.



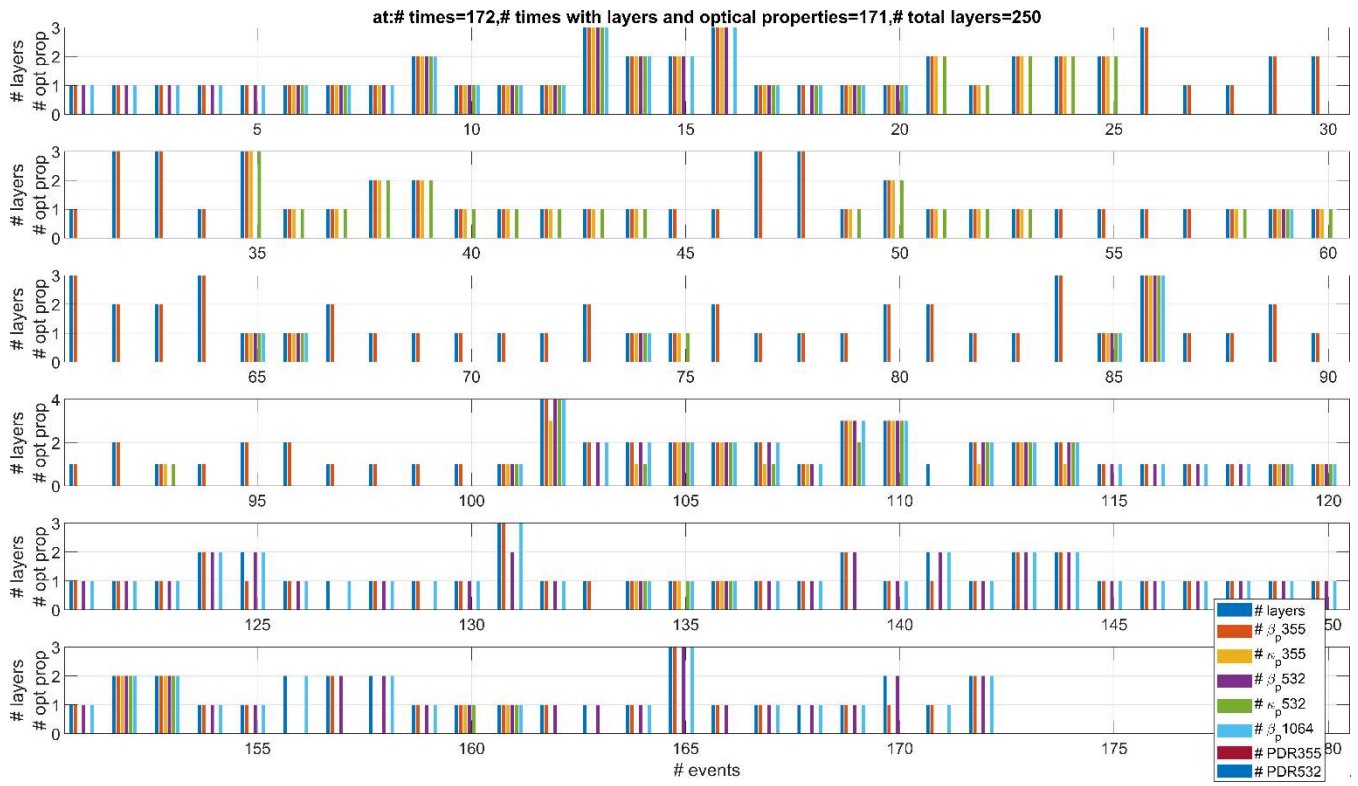
h) Three layers detected based on  $\beta_{1064}$  signal with the boundaries [915 1617] m, [1617 3142] m and [5264 5801] m. The top of the second layer was manually modified from 3612 m to 3142 m.



5 i) Three layers selected, based on  $\beta_{532}$  signal. Layers' boundaries are [2715 3915] m, [3915 4965] m and [4965 7365] m. The bottom of the second and third layers were manually changed from 4485 m to 3915 m and from 5295 m to 4965 m.

10

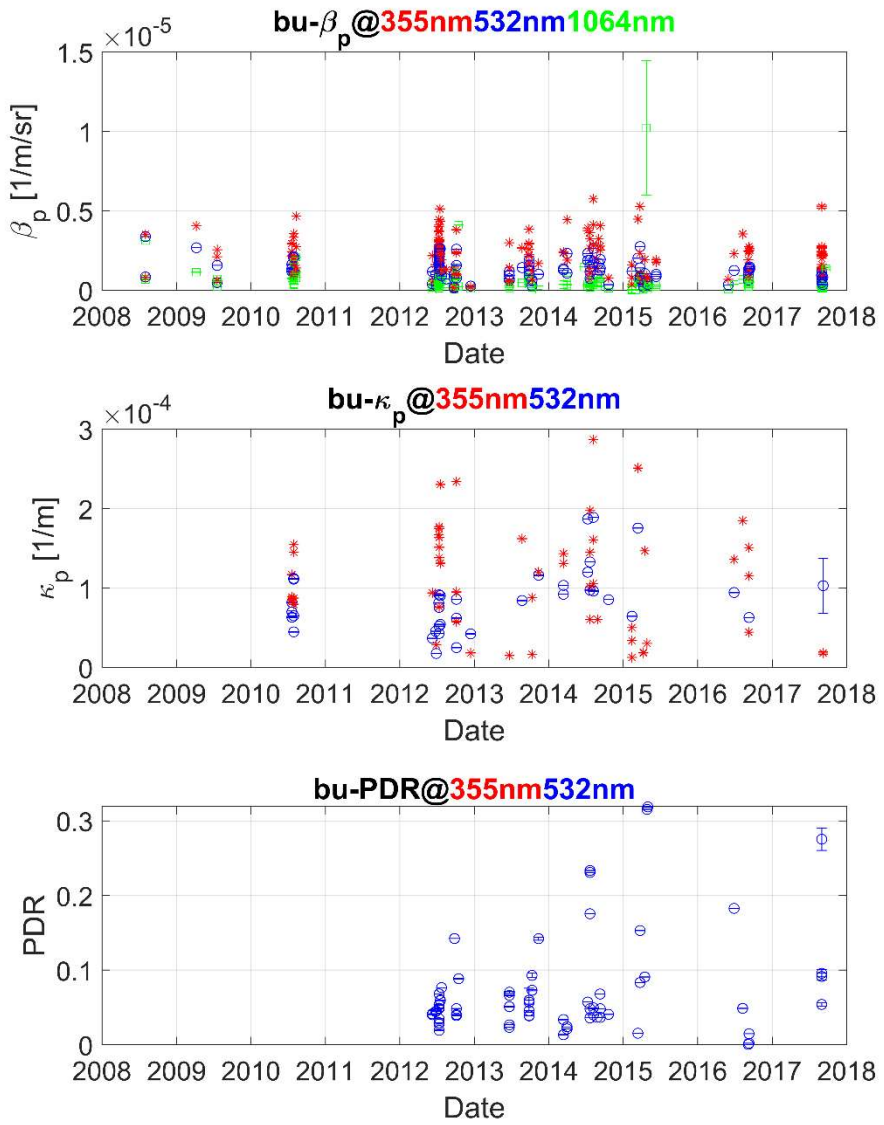
**Figure 5. Examples of layers selection, based on  $\beta_{1064}$  signal (a-d, f-h),  $\beta_{532}$  signal (i) and  $\beta_{355}$  signal (e). Layers are shown by grey areas. All available optical properties are shown (particles backscatter coefficients  $\beta_p$  on the left, particles extinction coefficients  $\kappa_p$  in the middle and particles linear depolarization  $\delta_p$  on the right). The boundaries shown in a-e plots are the automatic output of the algorithm. In the f-i plots, one or more boundaries retrieved by the algorithm were manually adjusted.**



**Fig. 6. The number of times (events) when the layers were evaluated and the corresponding number of optical properties available in the layer. Example for the Athens station. Layers have a biomass burning origin (fire source). For event 111 it was not feasible to determine any optical property.**

5

10



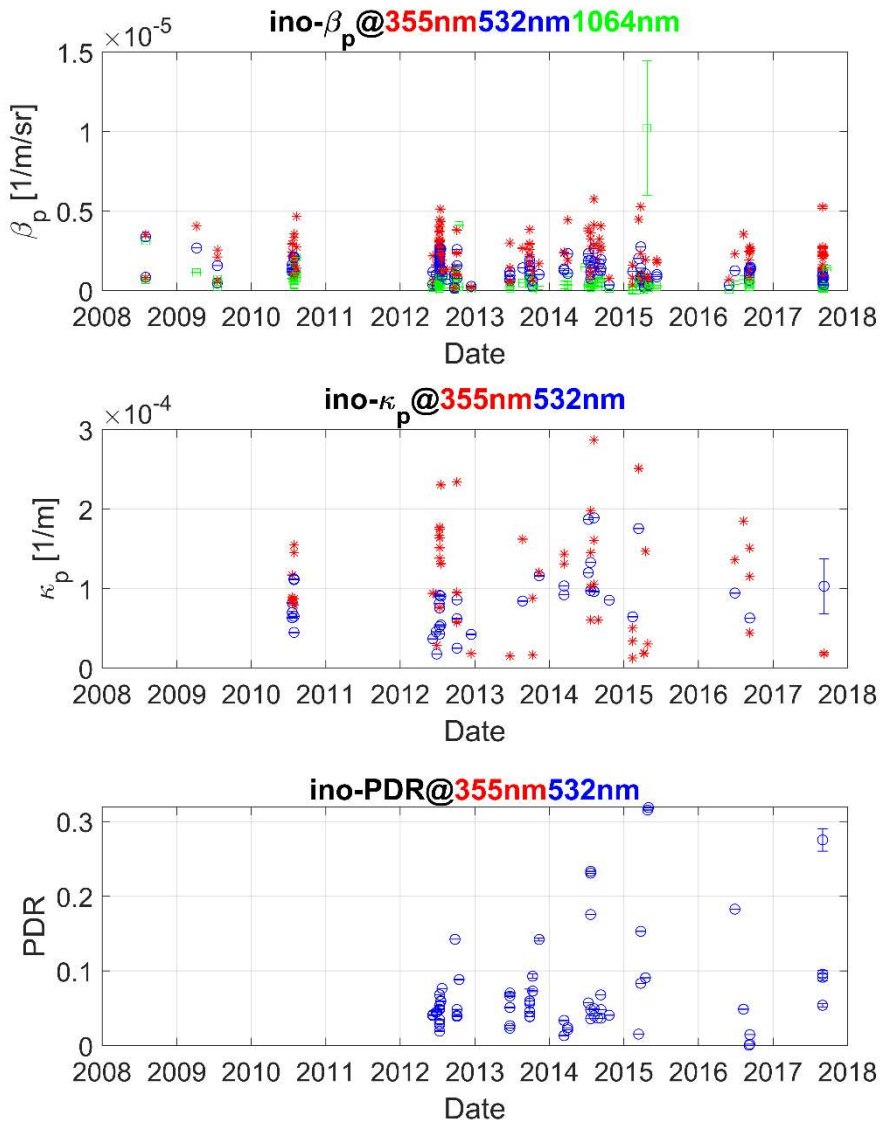
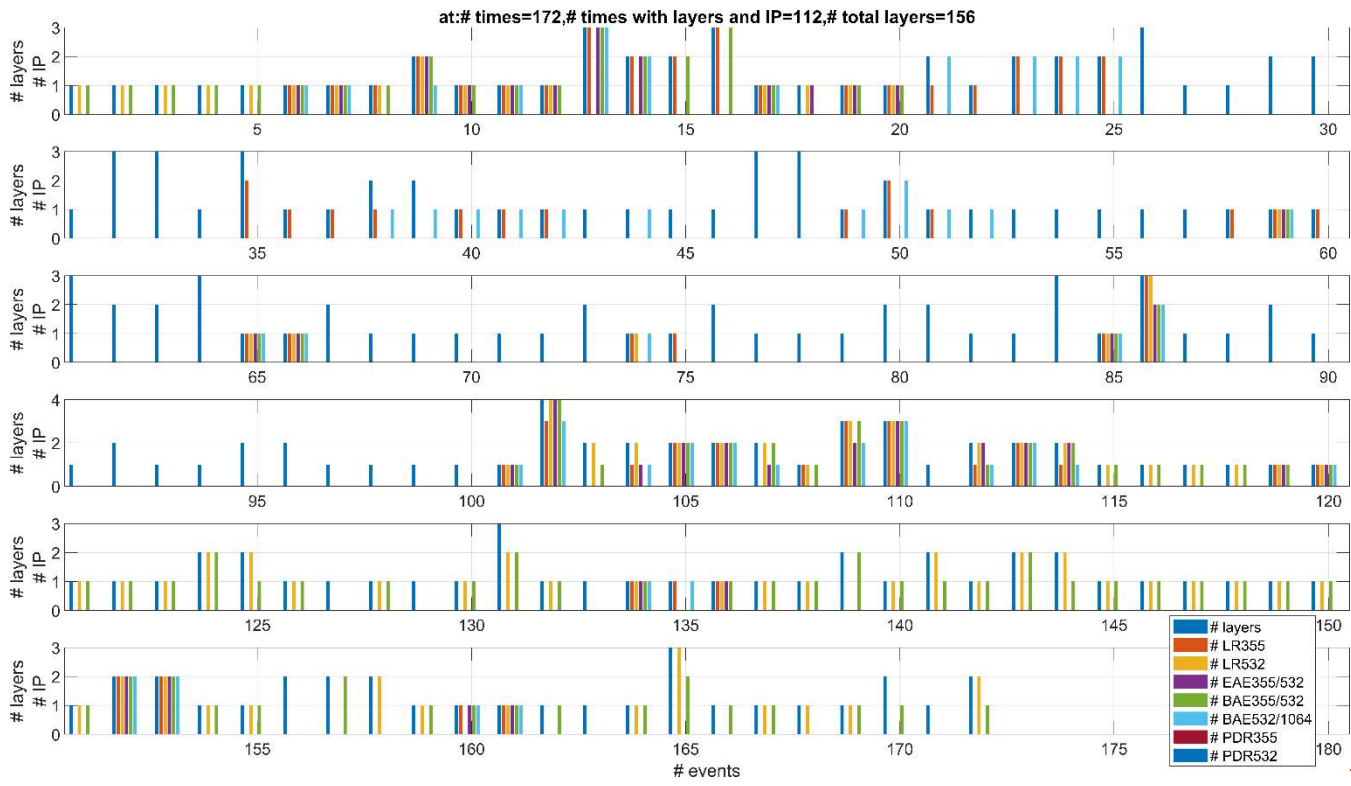
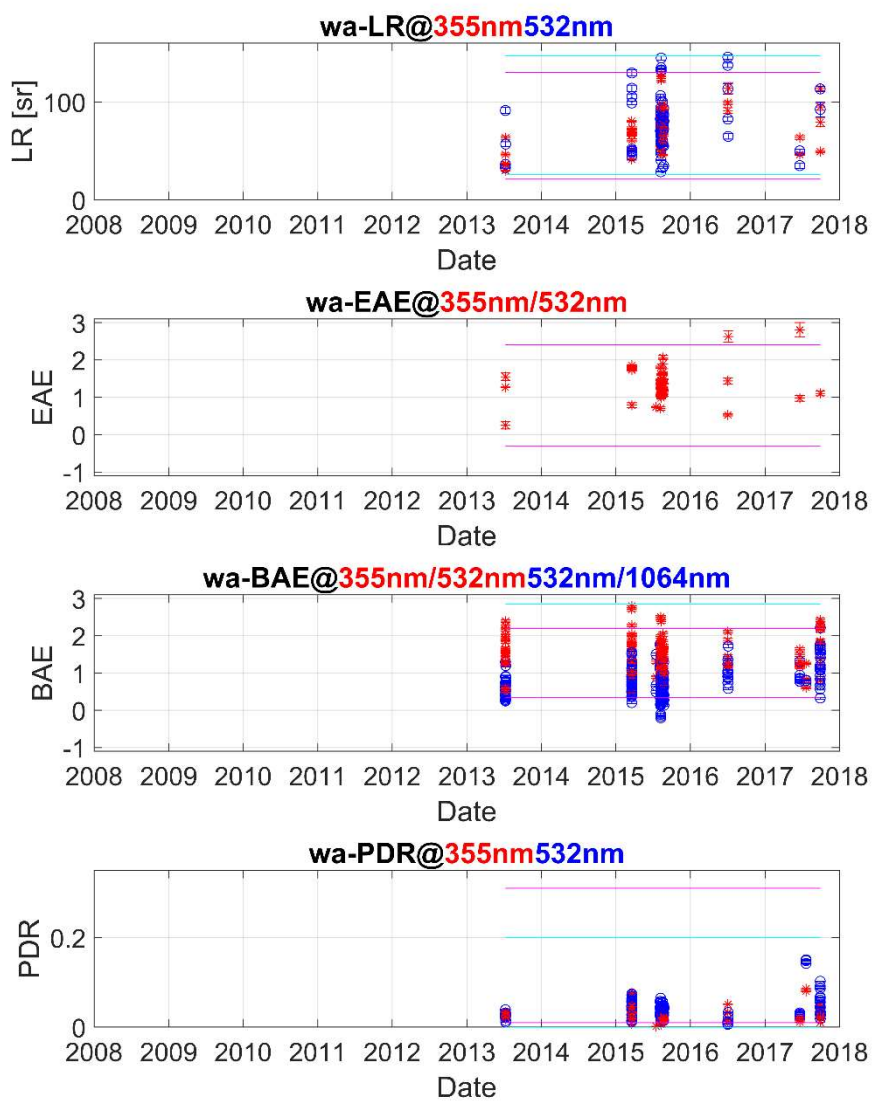


Fig. 57. Values of the mean optical properties and associated uncertainties in the layers. Example for the Bucharest (“ino”-“bu”) station. Layers were identified as having a fire source. Note that with few exceptions the uncertainties are very small and thus undiscernible from the mean values.



**Fig. 8. The number of times (events) when the layers were evaluated and the corresponding number of intensive parameters available in the layer. Example for Athens station. Layers have a biomass burning origin (fire source).**



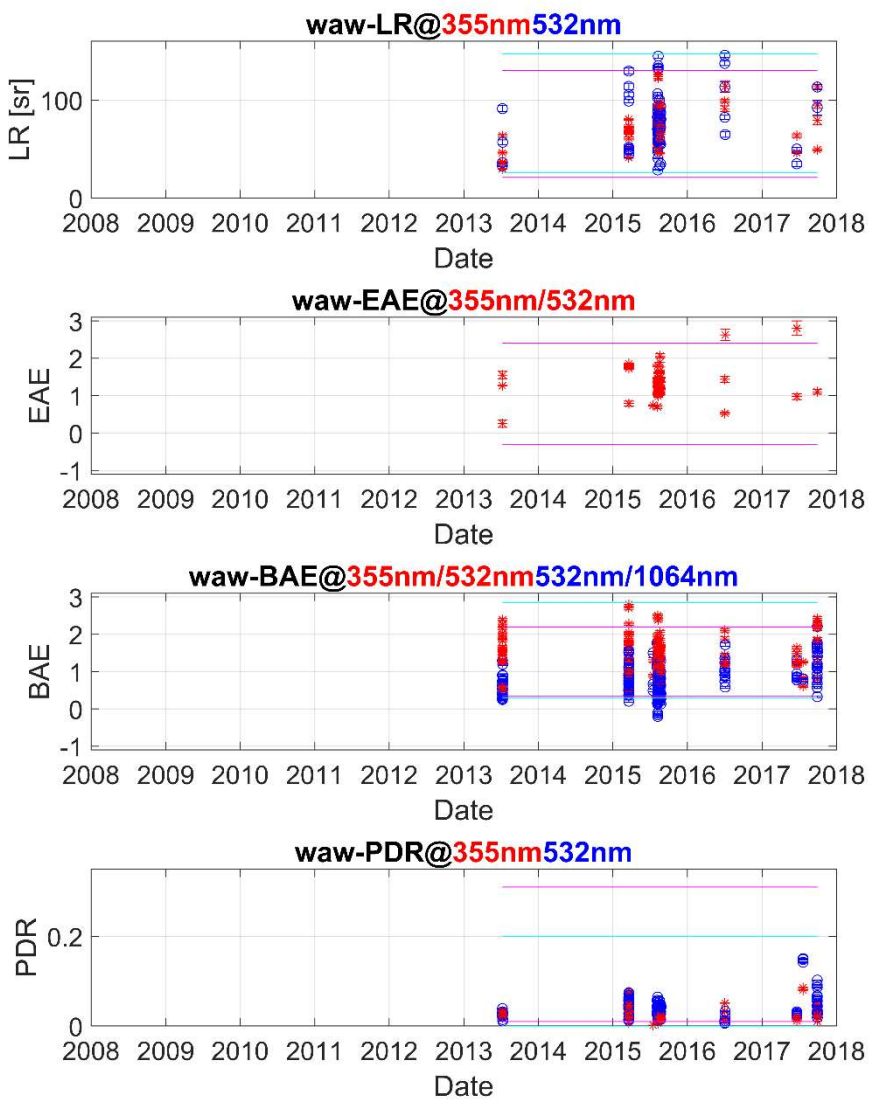
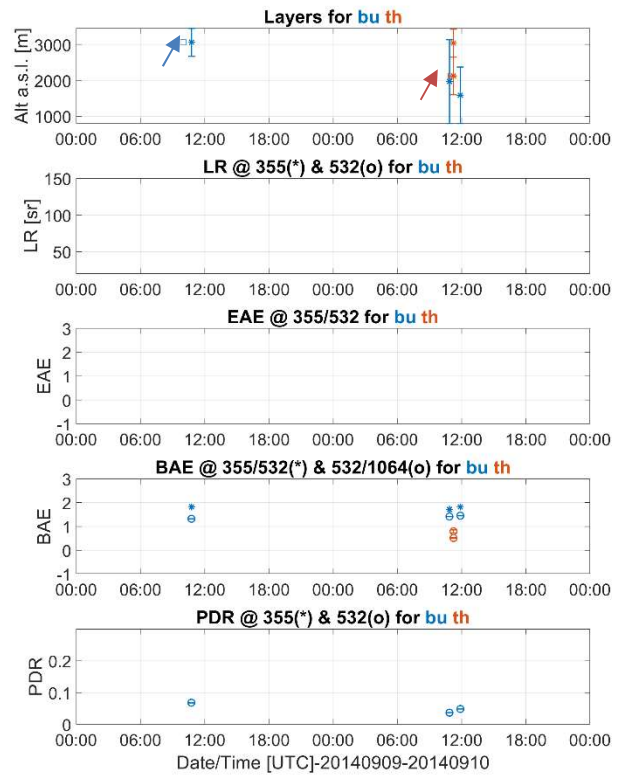
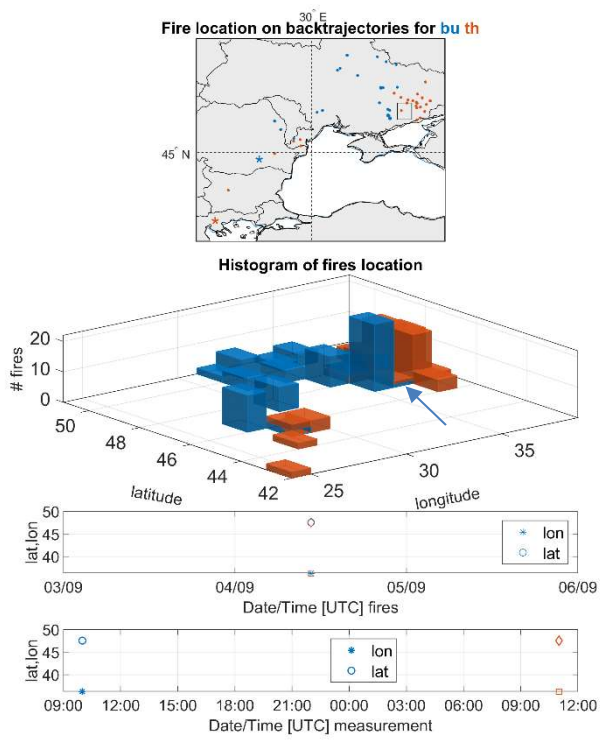
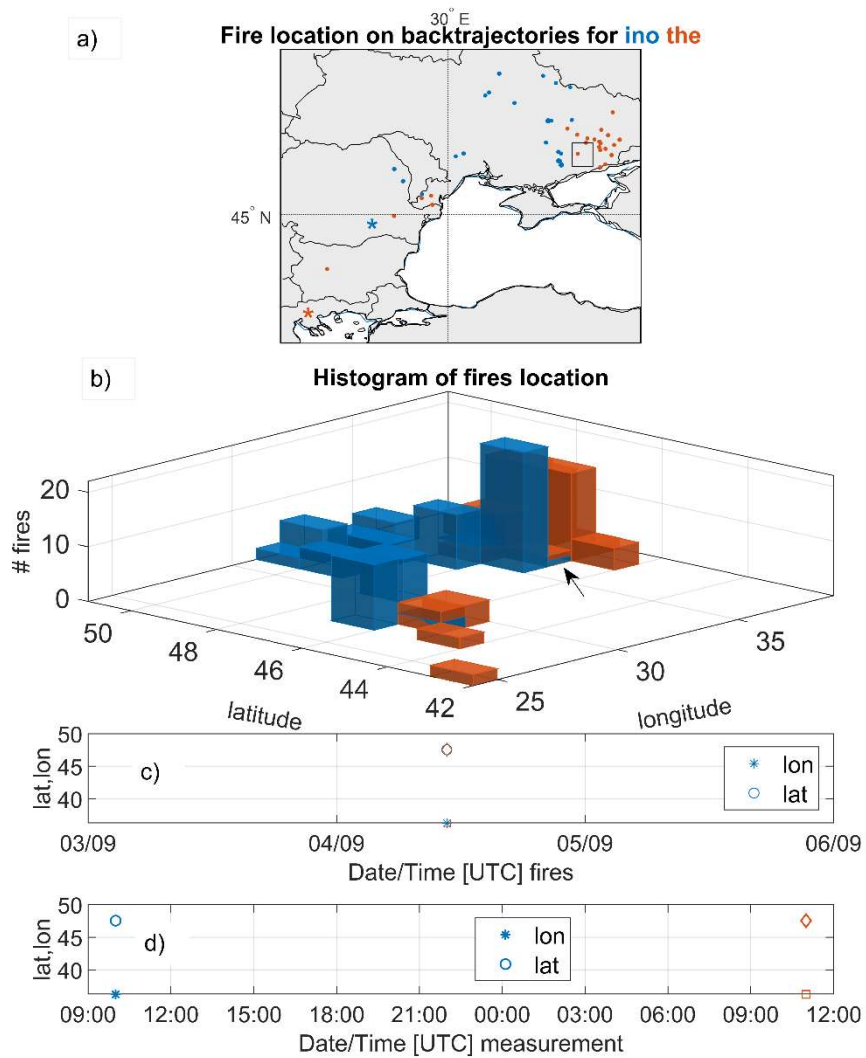


Fig. 69. Intensive aerosol parameters derived in the layers. Example for Warsaw (“wawwa”) station. The lines represent the minimum and maximum values reported in literature. Magenta lines represent the extreme values for the intensive parameters shown in red while the cyan lines represent the extreme values for the intensive parameters shown in blue. Layers have fire source

5 origin.





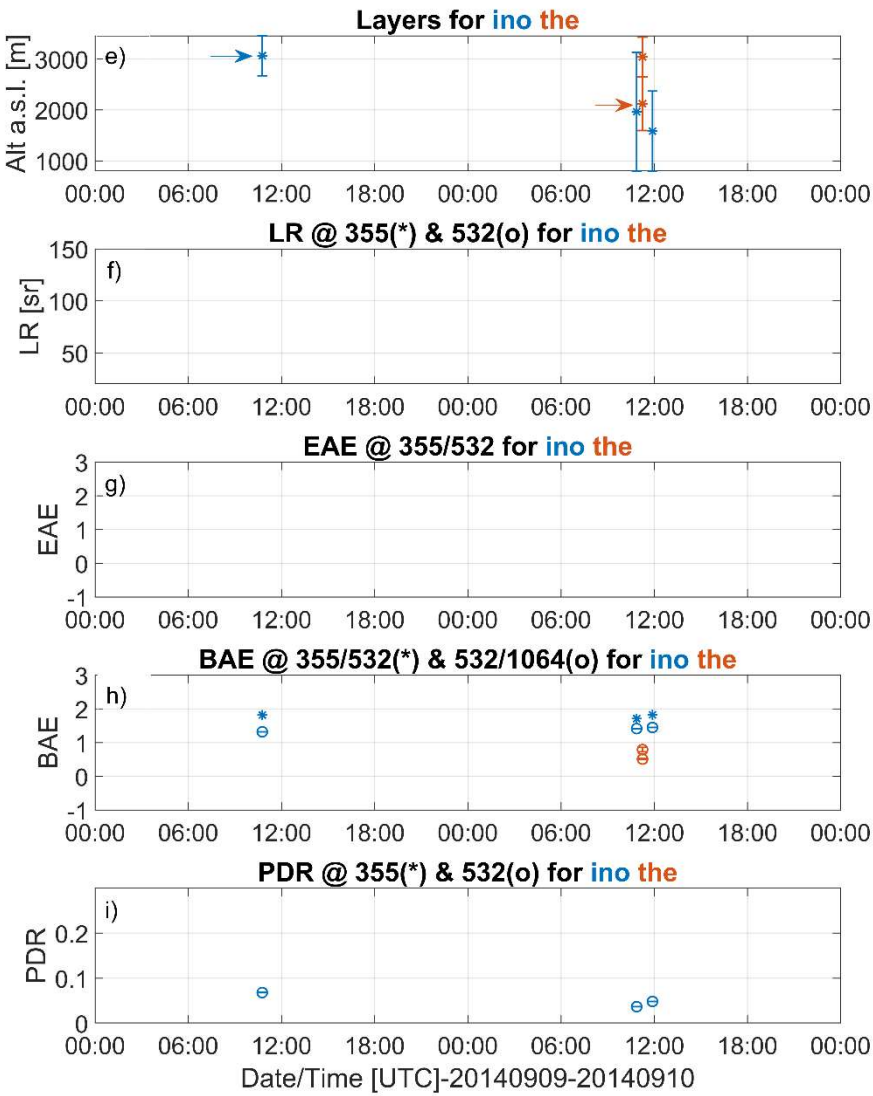


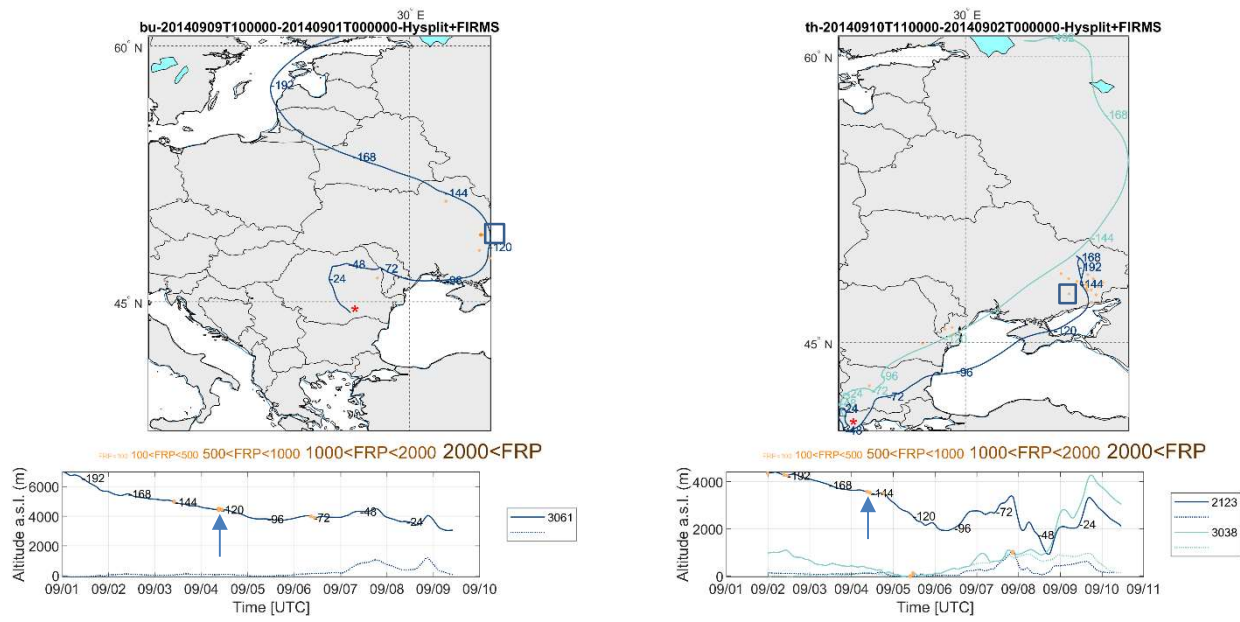
Fig. 10. Measurements with the same source at Thessaloniki ('th') and Bucharest ('bu'). Event: 20140909-20140910. Left plots: (first) fires location seen during back-trajectories from each station (colour coded), (second) histogram of the fires occurrence in each geographical grid, (third) longitude and latitude of the fires' location versus fires' occurrence time, (forth) longitude and latitude of the fires' location versus measurement time at the two locations. Right plots: layers' altitude and intensive parameters for each station. Layers measuring the common fire are shown by arrows. The geographical location of the common fire is shown on histogram by an arrow.

5

**Figure 7. Measurements with the same source in Thessaloniki ("the") and Bucharest ("ino") during 20140909-20140910. a) Fires location seen during back-trajectories from each station (colour coded); b) Histogram of the fires occurrence in each geographical grid; c) Longitude and latitude of the fires' location versus fires' occurrence time; d) Longitude and latitude of the fires' location**

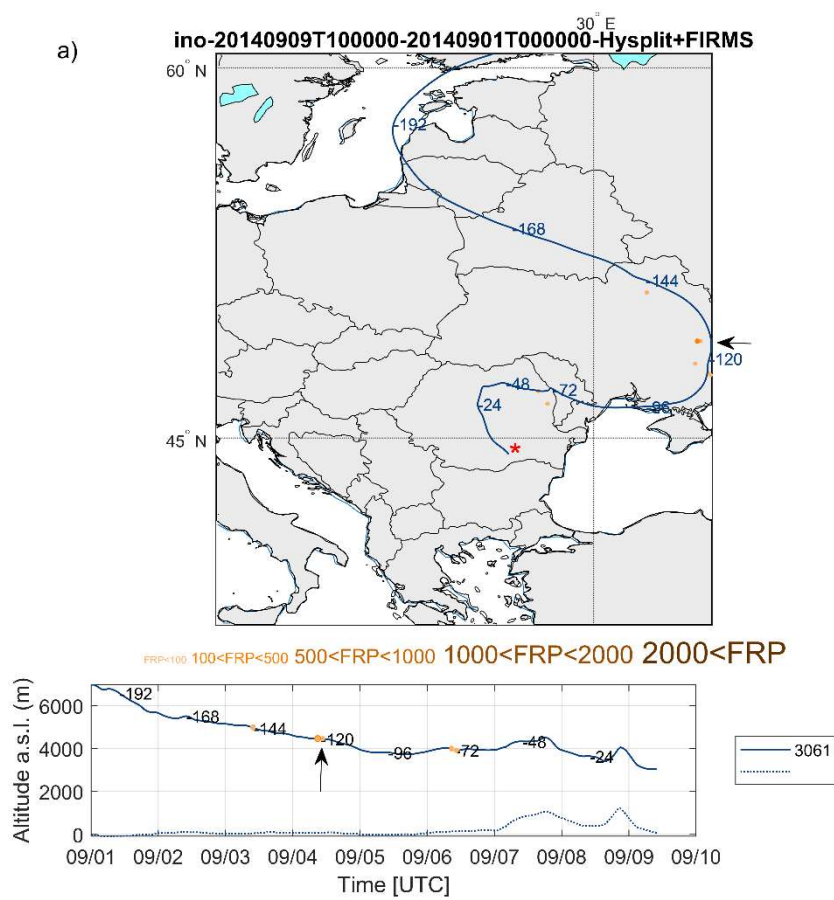
**versus measurement time at the two locations; e–i) layers altitude and intensive parameters for each station. Layers measuring the common fire are shown by arrows. The geographical location of the common fire is shown on histogram by an arrow.**

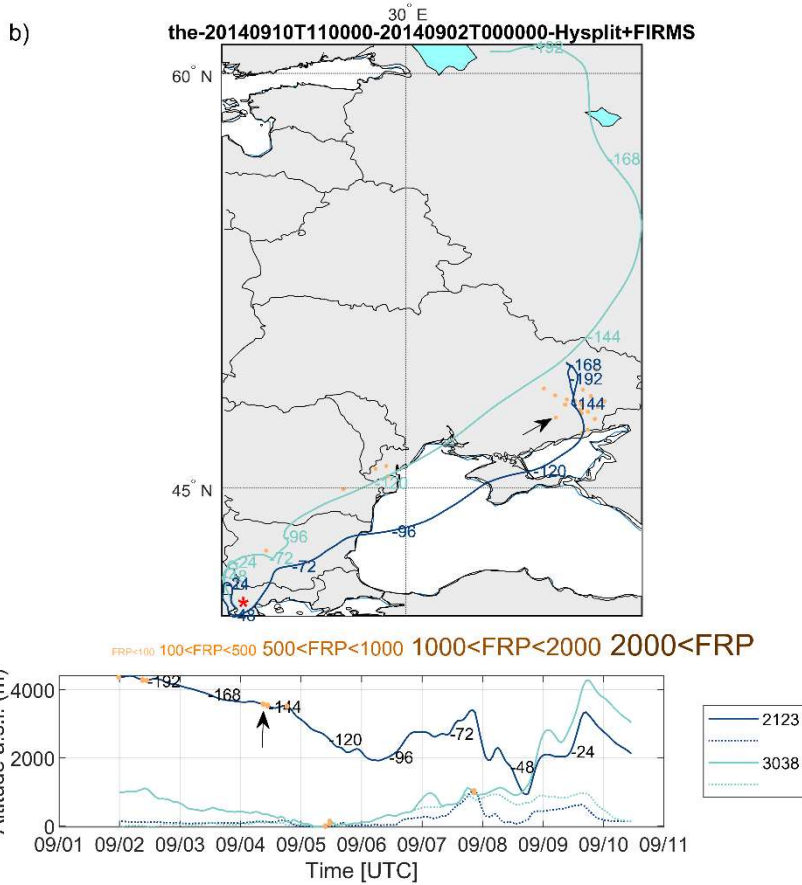
5



10

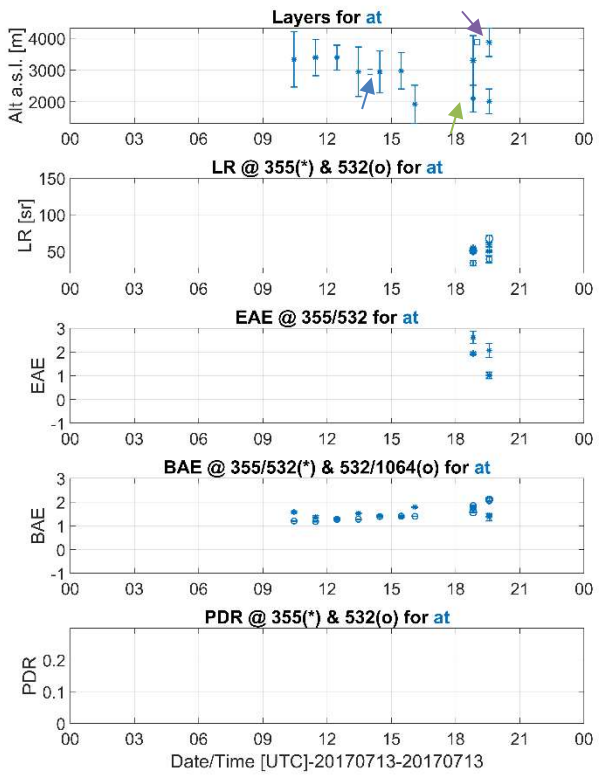
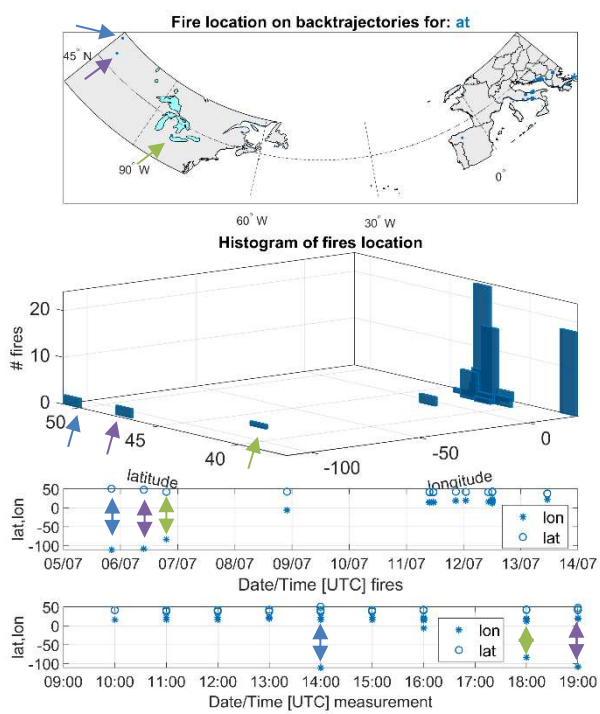
53

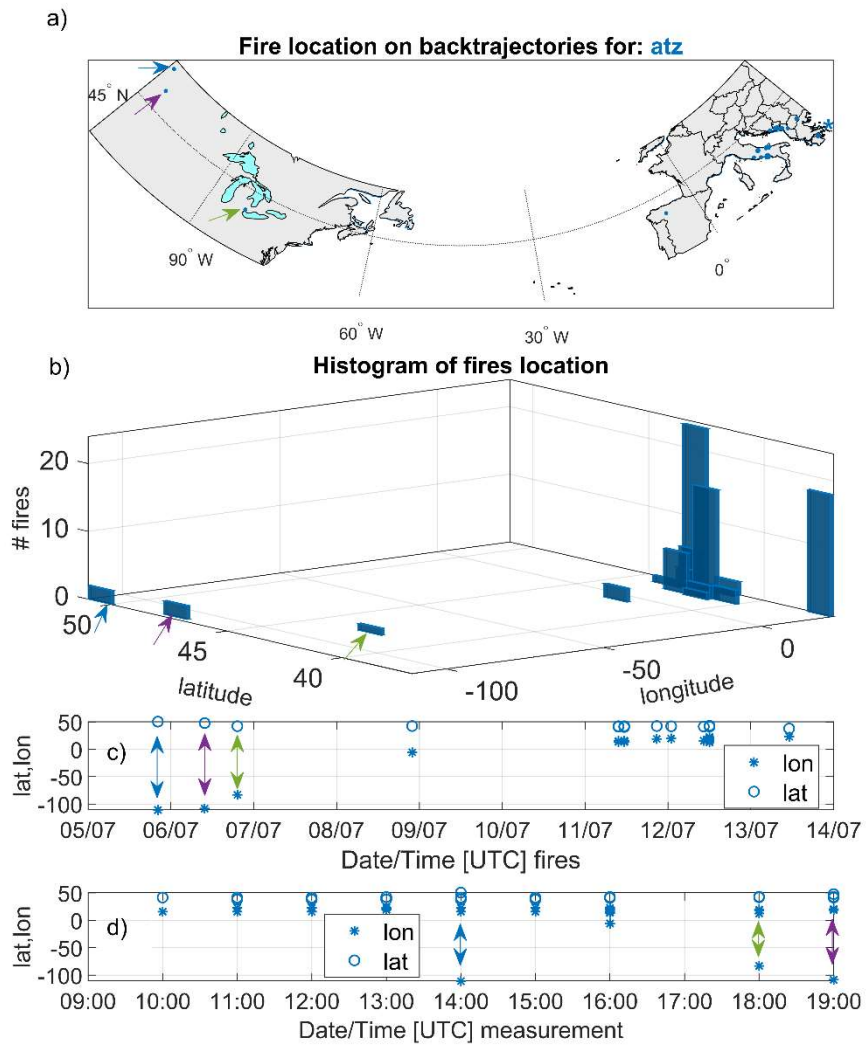




**Fig. 11. Backtrajectories and location of fires along backtrajectories within 100 km and +/- 1h for Bucharest ('bu') on 20140909 (left) and Thessaloniki ('th') on 20140910 (right). Lower plots show the altitude (a.s.l.) of the backtrajectories function of time. The fires' time is shown as well (see arrow location). The blue square denotes the geographical location of the common fire. See text for more details.**

5 **Figure 8. Backtrajectories and location of fires along backtrajectories within 100 km and +/- 1h for Bucharest ("ino") on 20140909 (a) and Thessaloniki ("the") on 20140910 (b). Lower plots show the altitude (a.s.l.) of the backtrajectories versus time. The common fire location is marked with an arrow. See text for more details.**





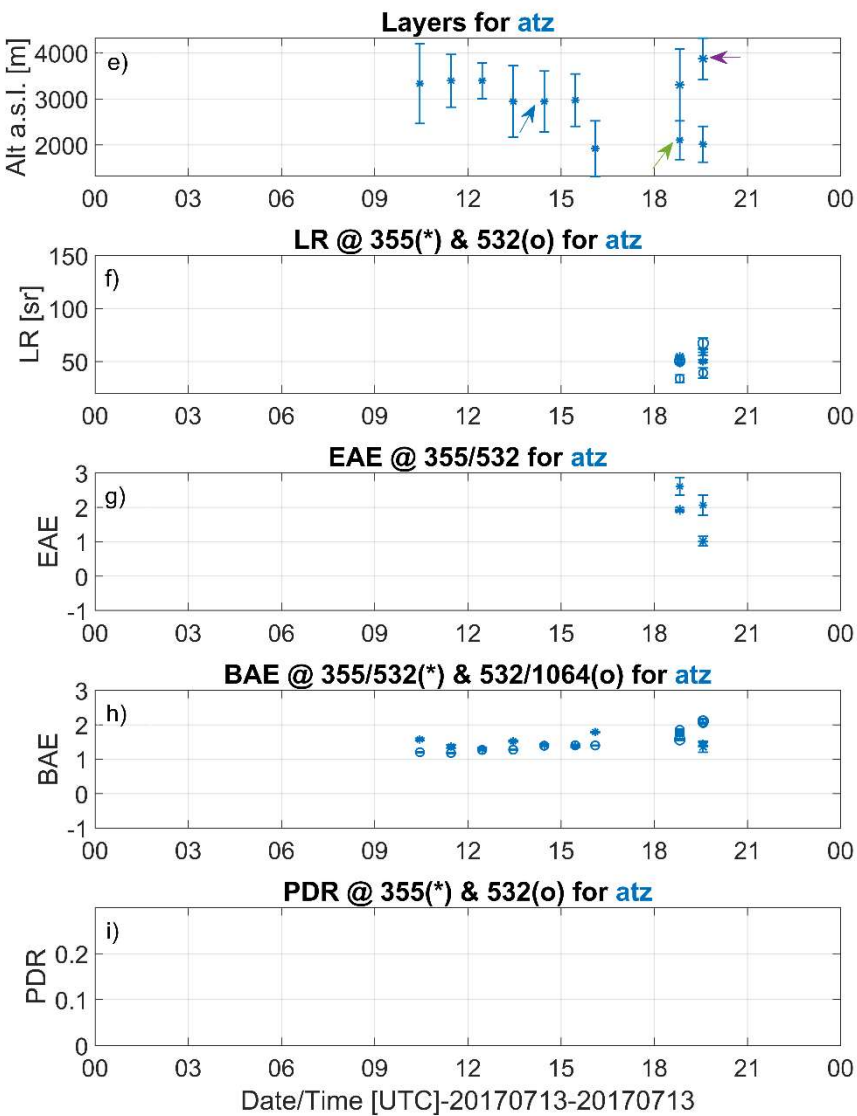
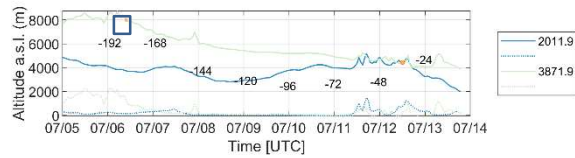
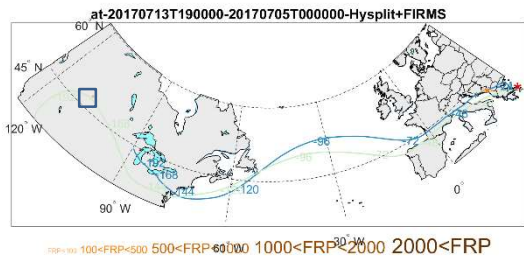
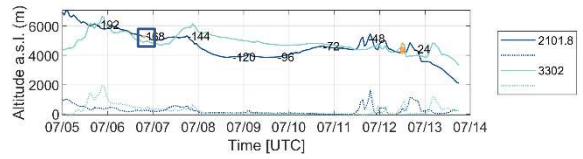
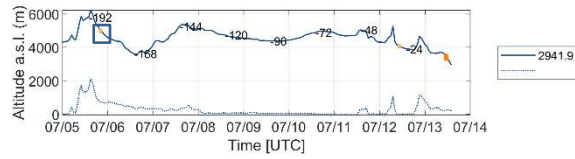
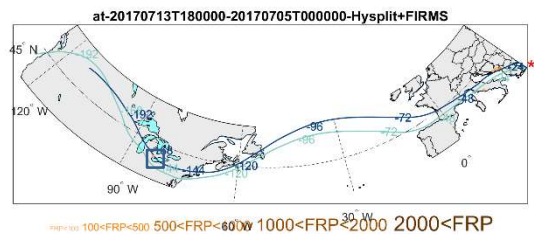
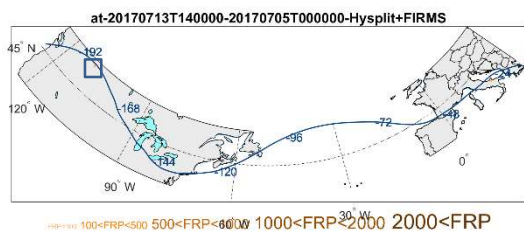
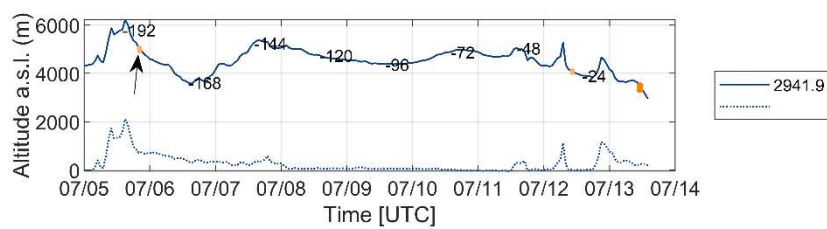
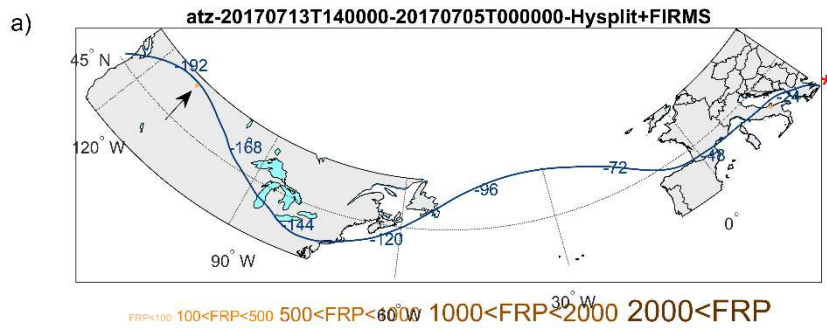


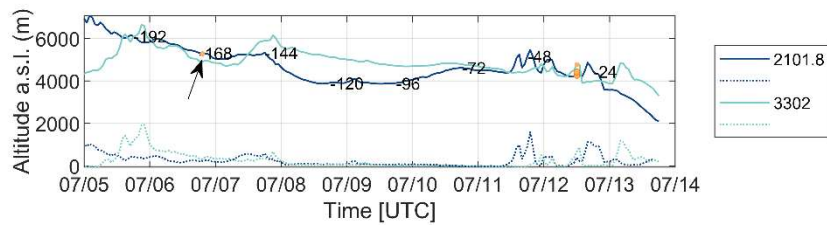
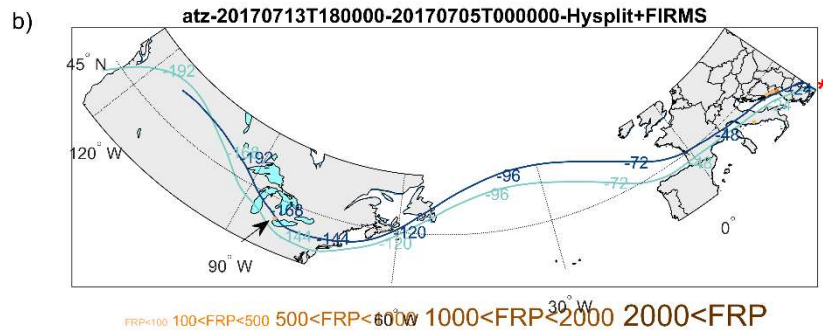
Fig. 12. LRT as measured at “at” on 20170713. First two BB layers are considered “mixed” while the third “pure NA”. The arrows show the location of the fires (left plot) and the location of the smoke layers (right plot).

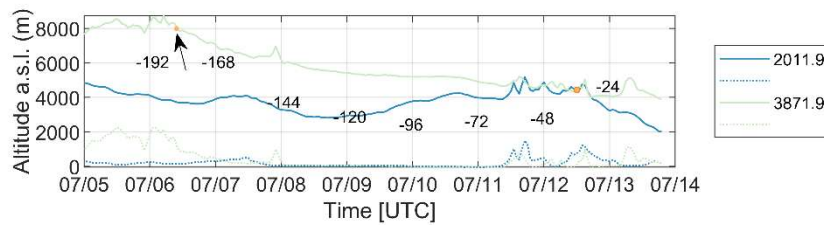
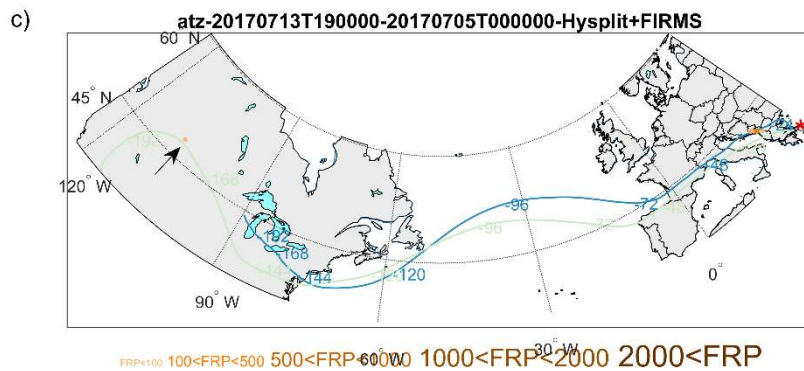
5

**Figure 9. LRT as measured at Athens (“atz”) on 20170713.** a) Location of the fires; b) Histogram of the fires. The North America fires are marked by arrows; c) Fires’ coordinates versus fires’ occurrence time; d) Fires’ coordinates versus measurements time; e) Location of the layers marked by arrows. First two BB layers are considered “mixed” while the third (magenta) “pure NA”; f) – i) Intensive parameters.





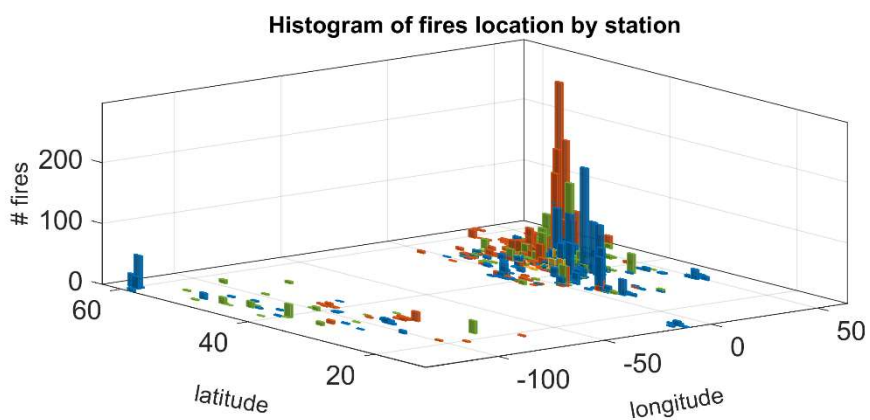
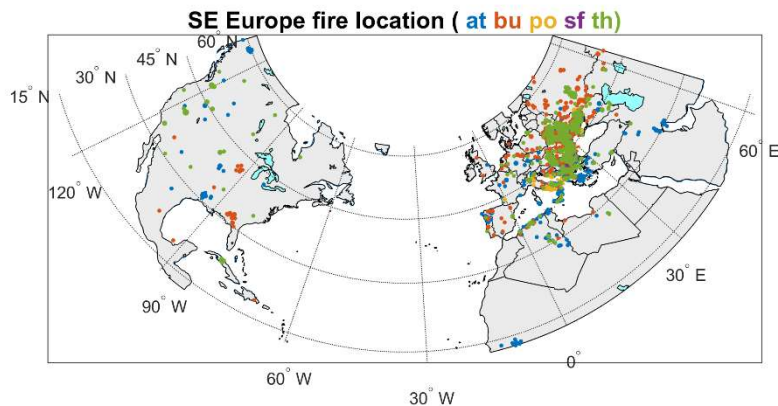


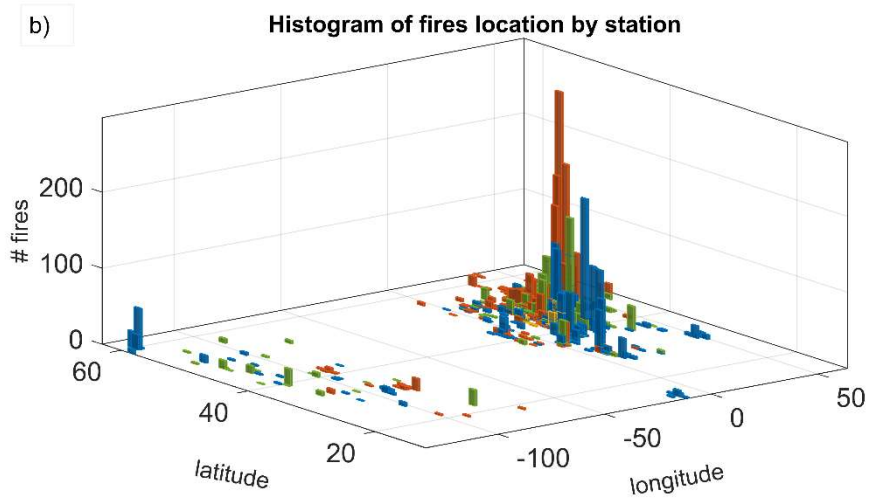
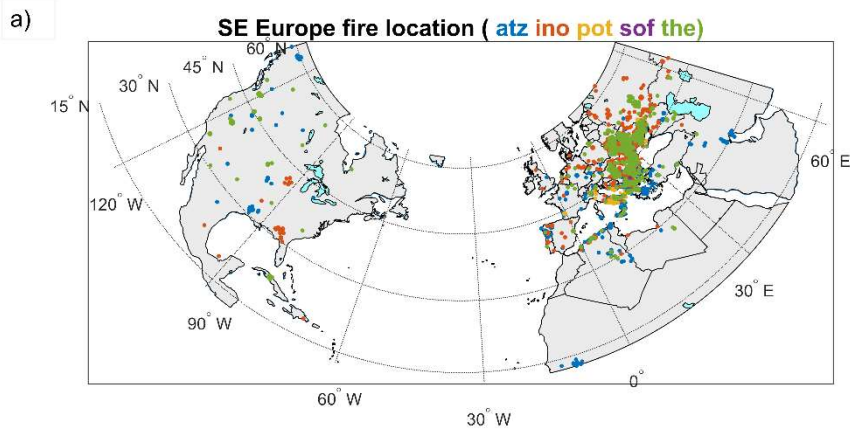


**Fig. 13. Backtrajectories for layers shown in Fig. 12 for Athens ('at') station. First two layers are considered "mixed" while the third is considered "pure N America". See text for more explanation. The squares show the location of the fire.**

5

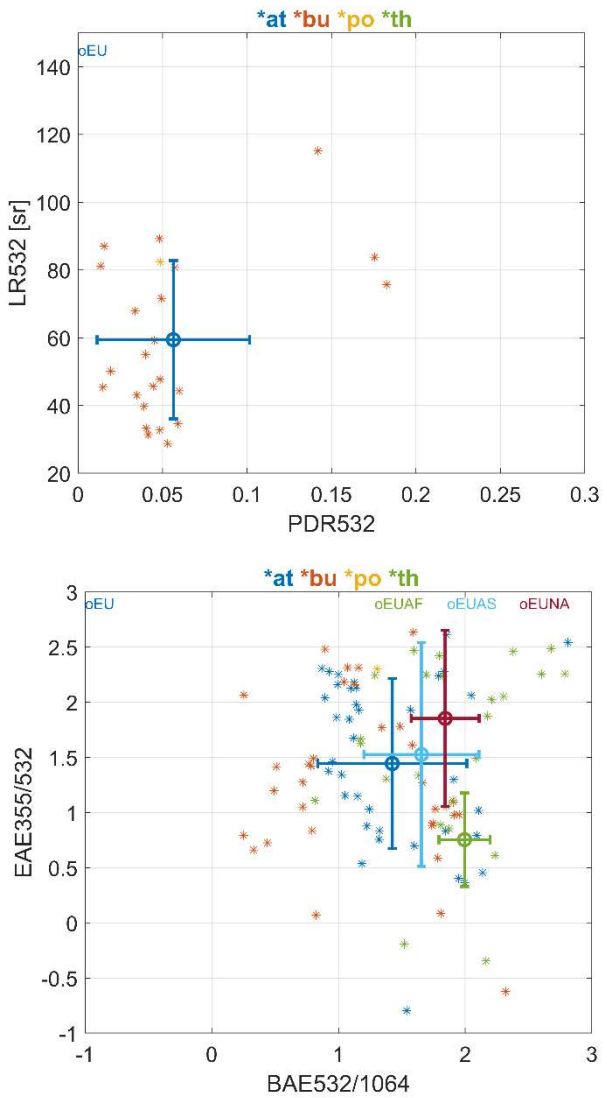
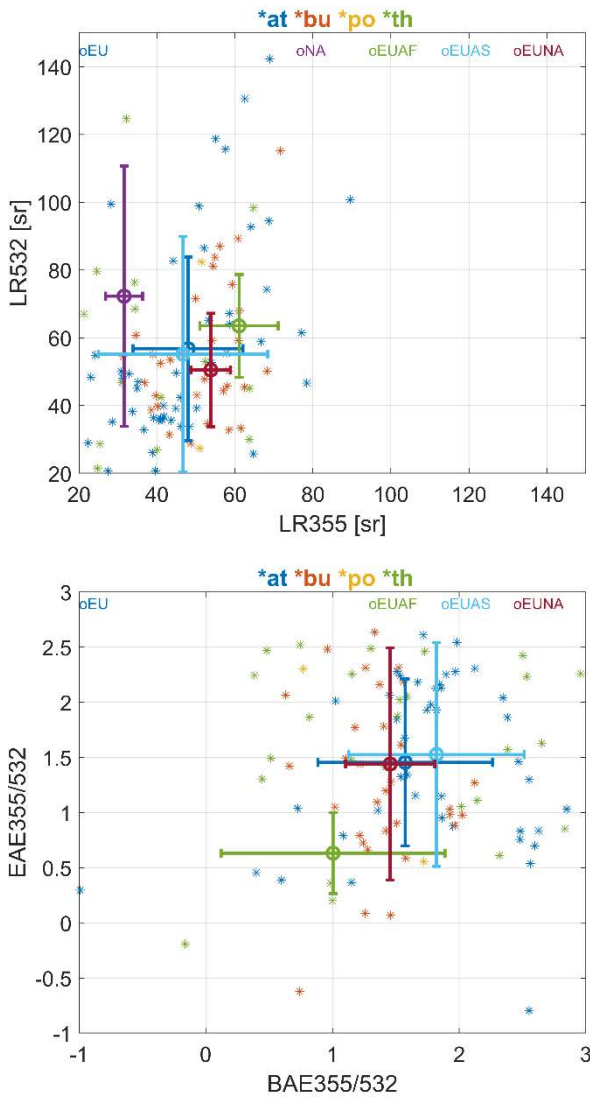
**Figure 10. Backtrajectories for layers shown in Fig. 9 for Athens ("atz") station. Layers in a) and b) are considered "mixed" while the layer in c) is considered "pure N America". See text for more explanation. The fire location is marked with an arrow.**

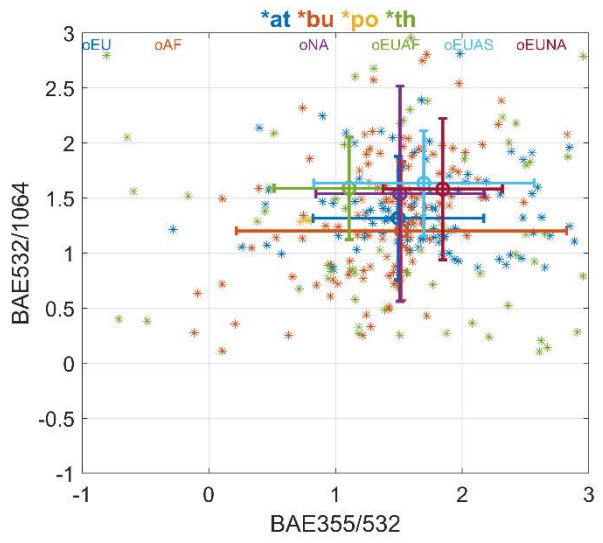
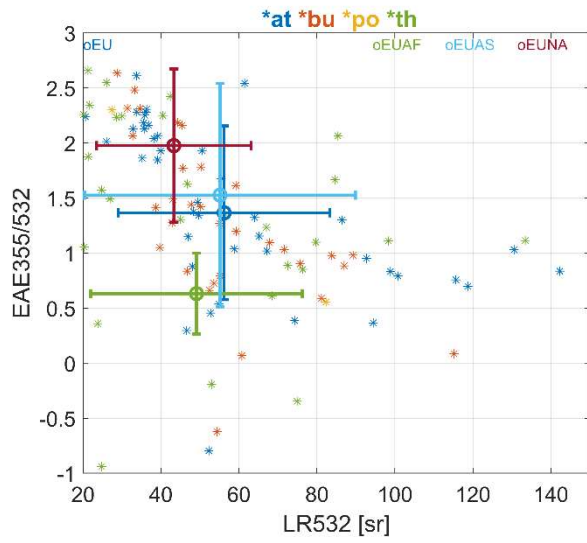


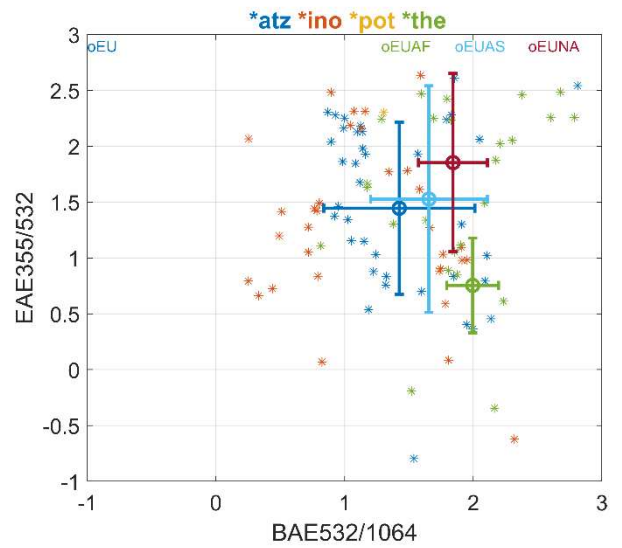
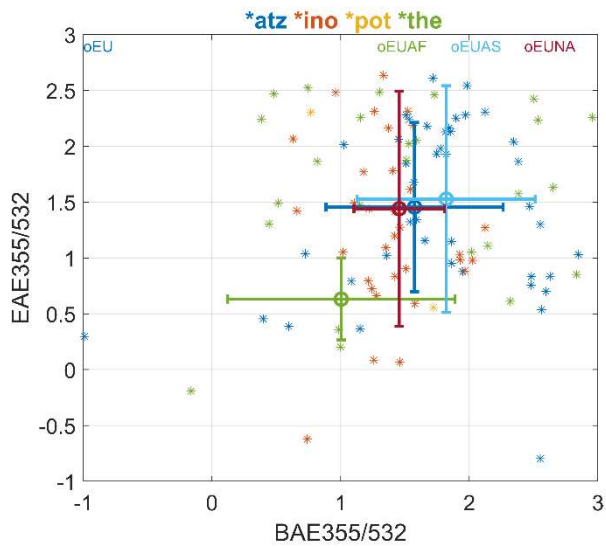
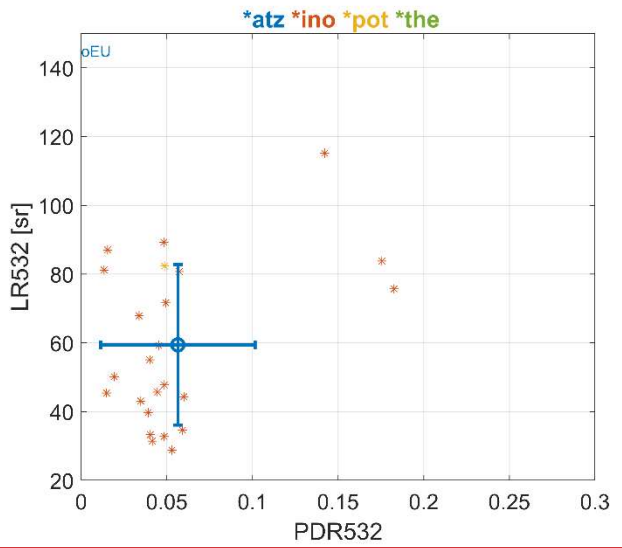
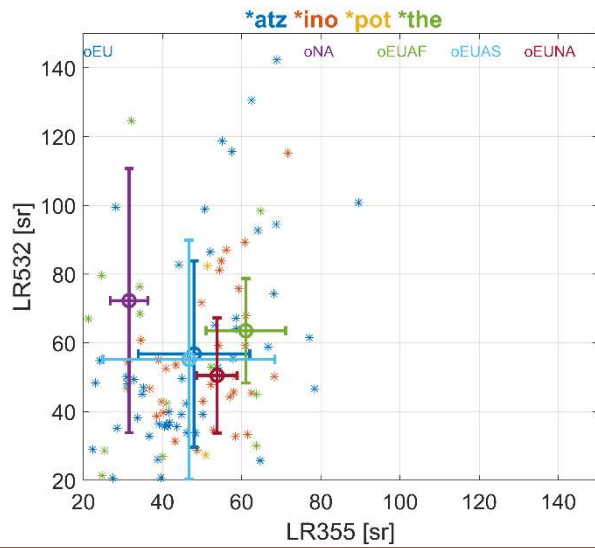


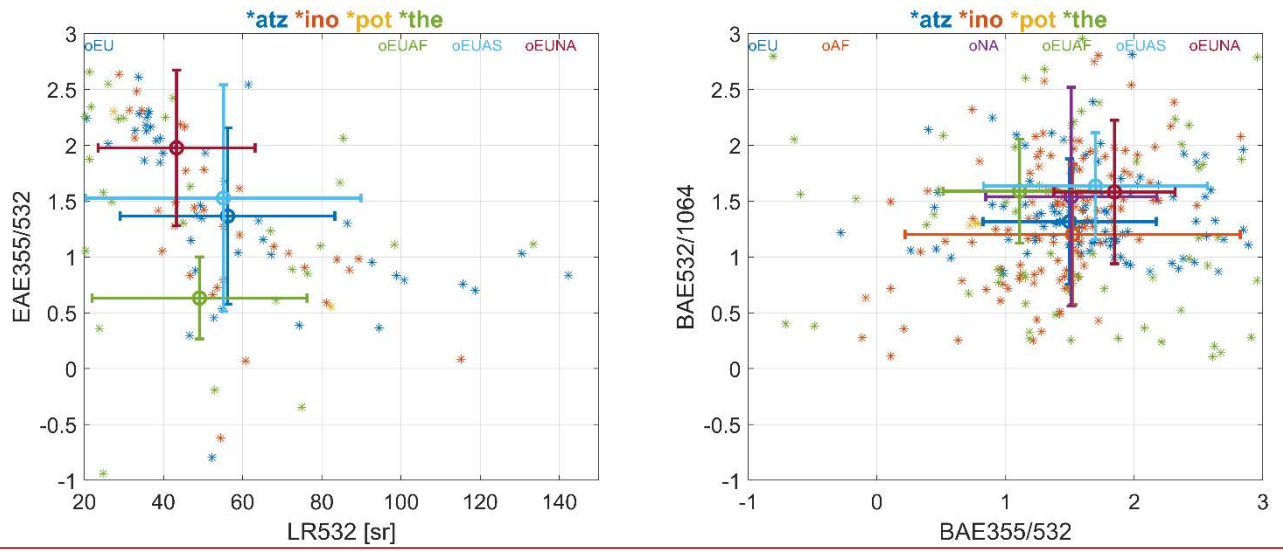
**Fig. 14. SE Europe region formed by stations “at”, “bu”, “po”, “sf” and “th”. Upper plot shows the location of the fires detected by each station. Note that due to overlap some are not seen. The bottom plot shows the histogram of the fires detected by each station.**

**Figure 11. SE Europe region formed by stations Athens (“atz”), Bucharest (“ino”), Potenza (“pot”), Sofia (“sof”) and Thessaloniki (“the”). a) Location of the fires detected by each station. Note that due to overlap some are not seen. b) Histogram of the fires detected by each station.**









5 **Fig. 15** Scatter plots between various two intensive parameters for SE region. The colour code of the points is station related (as labelled in the title). The colour code for the mean and STD values is related with the source origin (as stated on the plots).

**Figure 12.** Scatter plots between various two intensive parameters for SE region (LR@532 vs LR@355, LR@532 vs PDR@532, EAE355/532 vs BAE355/532, EAE355/532 vs BAE532/1064, EAE355/532 vs LR@532 and BAE532/1064 vs BAE355/532). The colour code of the points is station related (as labelled in the title). The colour code for the mean and STD values is related with the source origin (as stated on the plots).

10

15

20

**Table 1. List of stations and their number of backscatter (b-files) and/or extinction (e-files) at 355nm, 532nm and 1064nm. The number of particles backscatter ( $\beta_p$ ) and extinction ( $\kappa_{\text{ext}}$ ) coefficients and particles linear depolarization ratio ( $\text{PDR}_{\delta\text{p}}$ ) are shown as well. Highlights systems: 3b+2e; 3b+2e+1d or 3b+2e+2d; 3b; 1b. b=backscatter, e=extinction, d=depolarization. The last column represents the number of time stamps with at least one profile of optical properties (total number being 1138).**

5

	b355 files	b532 files	b1064 files	e355 files	e532 files	total b+e files	$\beta_p$ 355*	$\beta_p$ 532*	$\beta_p$ 1064	$\kappa_{\text{ext}}$ 355	$\kappa_{\text{ext}}$ 532	$\text{PDR}_{\delta\text{p}}$ 355	$\text{PDR}_{\delta\text{p}}$ 532	# times
"atz"æt	324	128	127	163	160	902	324	128	127	163	160			329
"brc"ɒə	3	10	10	0	0	23	3	10	10	0	0			13
"cog"ɒe	3	13	14	0	0	30	3	13	14	0	0			14
"ino"ɒu	169	150	169	71	65	624	169	153	169	71	65		144	173
"cbw"ea**	11	11	11	7	3	43	11	11	11	7	3			11
"evo"ev	19	42	43	22	22	148	19	42	43	22	22			43
"gra"əf	91	107	151	47	47	443	138	154	151	47	47			163
"lei"ɛ	1	15	10	0	0	26	1	15	10	0	0			17
"mas"mɪ	34	40	36	0	0	110	34	40	36	0	0			42
"hpb"əh	18	27	22	17	18	102	18	27	22	17	18		24	27
"pot"əə	7	8	6	7	7	35	8	8	6	7	7		8	8
"sof"əf	0	0	7	0	0	7	0	0	7	0	0			7
"the"θə	101	117	77	52	46	393	101	117	77	52	46			140
"waw"əwə	138	145	147	138	135	703	140	146	147	138	135	131	144	151
#tot	919	813	830	524	503	3589	969	864	830	524	503	131	320	4141
#sta	13	13	14	9	9		12	12	13	8	8	1	4	

\* backscatter coefficient profiles from both b-files and e-files; for the same time stamp, the profile from e-file is kept

#tot=total number of files or profiles; #sta=number of stations with particular file or profile

10

**Table 2. Summary of main features used to calculate the backscatter and extinction coefficient, specific for each b- and e-files. Detection mode: 1 (photon counting), 2 (analog), 3 (analog + photon counting). Evaluation mode: 1 (Klett-Fernald), 2 (Raman), 3 (aerosol backscatter ratio).**

	Detection mode (1/2/3)	Evaluation method (1/2/3)	Raw-resolution	Shots-averaged	Zenith angle
b355	176/153/ <b>590</b>	<b>524</b> /130/257	<del>most@3.75m and 60m</del>	<del>most@1e4</del>	<del>most@0°</del>
e355	<b>417</b> /0/107	0/ <b>516</b> /0	<del>most@60m</del>	<del>most@1e4</del>	<del>most@0°</del>
b532	229/199/ <b>385</b>	<b>335</b> /296/174	<del>most@3.75m, then 7.5m, 15m, 60m</del>	<del>most@1e4</del>	<del>most@0°</del>
e532	<b>409</b> /0/94	0/ <b>496</b> /0	<del>most@60m</del>	<del>most@1e4</del>	<del>most@0°</del>
b1064	222/ <b>608</b> /0	<b>683</b> /139/0	<del>most@3.75m, then 15m and 60m</del>	<del>most@1e4</del>	<del>most@0°</del>

5

10

15

20

**Table 23.** (2) Number of time stamps with at least one profile of optical properties (# times); (3) number of time stamps with layers and at least one optical property in the layer; (4) total number of layers for time stamps in (3); (5) number of time stamps with optical properties of fire origin. (6) total number of layers for time stamps in (5); Columns 7 and 8 represent the number of times with good optical properties and the total number of layers with good optical properties. Columns 9 and 10 represent the final number of time stamps and corresponding number of layers within imposed acceptable range.

1	2	3	4	5	6	7	8	9	10
Station	# times	# times with layers with optical properties	total # layers for (3)	# times with layers with optical properties of fire origin	total # layers for (5)	# times with layers with optical properties of fire origin, SNR>=2	total # layers for (7)	# times with layers with IP of fire origin, SNR>=2, within accepted range	total # layers for (9)
“ <u>atzat</u> ”	329	233	405	172	251	171	250	112	156
“ <u>brcba</u> ”	13	13	31	12	23	12	23	6	14
“ <u>cogbe</u> ”	14	14	58	14	21	14	21	13	20
“ <u>inobu</u> ”	173	163	289	109	168	109	167	86	130
“ <u>cbwea</u> ”	11	11	26	8	14	8	14	8	14
“ <u>evoev</u> ”	43	42	96	13	16	13	16	6	8
“ <u>gragf</u> ”	163	146	296	80	120	80	120	68	97
“ <u>leile</u> ”	17	17	35	11	18	11	18	4	5
“ <u>masmi</u> ”	42	32	86	25	52	25	52	21	43
“ <u>hpbeh</u> ”	27	21	50	12	18	12	17	11	15
“ <u>potpe</u> ”	8	7	9	5	7	5	7	4	6
“ <u>sofsf</u> ”	7	7	11	4	4	4	4	0	0
“ <u>theth</u> ”	140	103	216	88	151	88	151	66	107
“ <u>wawwa</u> ”	151	151	293	124	190	124	190	121	180
	1138	960	1901	677	1053	676	1050	526	795

## Anonymous Referee #2

Received and published: 6 June 2020

We would like to thank the reviewer for the thorough revision of the manuscript and for suggestions! We hope we addressed  
5 the comments accordingly.

We use across the text (below) the following highlights:

**In red, reviewer's comments.**

In black, our comments.

In green, the citations from the manuscript submitted.

10 In blue, the changed text for the revised manuscript.

Before answering to the reviewer's questions/comments etc, we would like to indicate a few changes that we have done to the initial manuscript. Those changes are not related with the data processing and analysing or its scientific content but rather with text cosmetics.

- added Faculty of Physics for co-author 2)

15 - in Acknowledgements we added Dominika Szczepanik

- in Funding, we added:

*The research was partially funded by the European Regional Development Fund through the Competitiveness 613 Operational Programme 2014-2020, POC-A.1-A.1.1-F- 2015, project Research Centre for Environment and Earth 614 Observation CEO-Terra, SMIS code 108109, contract No. 152/2016.*

20 - in References we added:

Adam, M., Nicolae, D., Belegante, L., Stachlewska, I. S., Janicka, L., Szczepanik, D., Mylonaki, M., Papanikolaou, C. A., Siomos, N., Voudouri, K. A., Alados-Arboledas, L., Bravo-Aranda, J. A., Apituley, A., Papagiannopoulos, N., Mona, L., Mattis, I., Chaikovsky, A., Sicard, M., Muñoz-Porcar, C., Pietruczuk, A., Bortoli, D., Baars, H., Grigorov, I., and Peshev, Z.: Biomass burning events measured by lidars in EARLINET. Part II. Results and discussions, *Atmos. Chem. Phys. Discuss.*,  
25 <https://doi.org/10.5194/acp-2020-647>, in review, 2020.

Janicka, L. and Stachlewska, I. S.: Properties of biomass burning aerosol mixtures derived at fine temporal and spatial scales from Raman lidar measurements: Part I optical properties, *Atmos. Chem. Phys. Discuss.*, <https://doi.org/10.5194/acp-2019-207>, 2019.

Müller, D., Ansmann, A., Mattis, I., Tesche, M., Wandinger, U., Althausen, D., and Pisani, G.: Aerosol-type-dependent lidar ratios observed with Raman lidar, *J. Geophys. Res.*, 112, D16202, doi:10.1029/2006JD008292, 2007.

- Based on suggestions from Earlinet community, we changed the stations acronyms from two letters to three letters, according to the new nomenclature. This was already implemented in Part II. Thus, all the figures with references at station acronyms (on labels or title) were changed for clarity and consistency. Similar holds for tables.

- based on editor's suggestion for Part II, we changed N to North (for N America and N Africa)

35 - based on suggestions from the editor of Part II, we refer to the stations in the text by the full name instead of using acronyms.

- EAE355/532 was changed to EAE in the text (two instances: pp 11, line 18 and line34).

- a list with the acronyms used in the text was added in Supplement (as in Part II) for consistency. The reference at the acronyms list is mentioned at the end of Introduction.

A list of acronyms used in the current work is given in the Supplement (Table S1).

- figs. 10, 11, 12, 13 and 14 (now 7, 8, 9, 10 and 11): we added a), b) etc for each plot for an easier reference. We made small changes to the text and changed the 3 figures caption:

Fig. 10 upper right plot -> Fig. 7 a

5 In Fig. 10, the first two left plots we show -> in Fig. 7 a-b we show

Fig. 10 lower left plots -> Fig. 7 c-d

Figure 7 caption:

Fig. 10. Measurements with the same source at Thessaloniki ('th) and Bucharest ('bu'). Event: 20140909-20140910. Left plots: (first) fires location seen during back-trajectories from each station (colour coded), (second) histogram of the fires occurrence in each geographical grid, (third) longitude and latitude of the fires' location versus fires' occurrence time, (forth) longitude and latitude of the fires' location versus measurement time at the two locations. Right plots: layers' altitude and intensive parameters for each station. Layers measuring the common fire are shown by arrows. The geographical location of the common fire is shown on histogram by an arrow.

Figure 7. Measurements with the same source in Thessaloniki ("the") and Bucharest ("ino") during 20140909-20140910. a)

15 Fires location seen during back-trajectories from each station (colour coded); b) Histogram of the fires occurrence in each geographical grid; c) Longitude and latitude of the fires' location versus fires' occurrence time; d) Longitude and latitude of the fires' location versus measurement time at the two locations; e-i) layers altitude and intensive parameters for each station. Layers measuring the common fire are shown by arrows. The geographical location of the common fire is shown on histogram by an arrow.

20 Figure 11, left -> Figure 8 a)

Fig. 11, right -> Fig. 8 b)

See lower plot of Fig. 10 -> See Fig. 8 b)

Figure 8 caption:

Fig. 11. Backtrajectories and location of fires along backtrajectories within 100 km and +/- 1h for Bucharest ('bu') on 20140909 25 (left) and Thessaloniki ('th') on 20140910 (right). Lower plots show the altitude (a.s.l.) of the backtrajectories function of time. The fires' time is shown as well (see arrow location). The blue square denotes the geographical location of the common fire. See text for more details.

Figure 8. Backtrajectories and location of fires along backtrajectories within 100 km and +/- 1h for Bucharest ("ino") on 20140909 (a) and Thessaloniki ("the") on 20140910 (b). Lower plots show the altitude (a.s.l.) of the backtrajectories versus 30 time. The common fire location is marked with an arrow. See text for more details.

Fig. 12, upper right plot -> Fig. 9 e

blue arrows in Fig. 12 -> blue arrows in Fig. 9 (a-e)

green arrows in Fig. 12 -> green arrows in Fig. 9 (a-e)

magenta arrows in Fig. 12 -> magenta arrows in Fig. 9 (a-e)

35 Figure 9 caption:

Fig. 12. LRT as measured at "at" on 20170713. First two BB layers are considered "mixed" while the third "pure NA". The arrows show the location of the fires (left plot) and the location of the smoke layers (right plot).

Figure 9. LRT as measured over Athens ("atz") on 20170713. a) Location of the fires; b) Histogram of the fires. The North America fires are marked by arrows; c) Fires' coordinates versus fires' occurrence time; d) Fires' coordinates versus

measurements time; e) Location of the layers marked by arrows. First two BB layers are considered “mixed” while the third (magenta) “pure NA”; f) – i) Intensive parameters.

The trajectory layer in Fig. 13 is the higher one (light blue). -> The trajectory layer in Fig. 10 c) is the higher one (light blue).

Figure 10 caption:

5 Fig. 13. Backtrajectories for layers shown in Fig. 12 for Athens (‘at’) station. First two layers are considered “mixed” while the third is considered “pure N America”. See text for more explanation. The squares show the location of the fire.

Figure 10. Backtrajectories for layers shown in Fig. 9 for Athens (“atz”) station. Layers in a) and b) are considered “mixed” while the layer in c) is considered “pure N America”. See text for more explanation. The fire location is marked with an arrow.

Figure 11.... Upper plot shows the location of the fires...-> Figure 11... a) Location of the fires

10 Figure 11... The bottom plot shows the histogram of the fires -> Figure 11... b) Histogram of the fires

Figure 11 caption:

Fig. 14. SE Europe region formed by stations “at”, “bu”, “po”, “sf” and “th”. Upper plot shows the location of the fires detected by each station. Note that due to overlap some are not seen. The bottom plot shows the histogram of the fires detected by each station.

15 Figure 11. SE Europe region formed by stations Athens (“atz”), Bucharest (“ino”), Potenza (“pot”), Sofia (“sof”) and Thessaloniki (“the”). a) Location of the fires detected by each station. Note that due to overlap some are not seen. b) Histogram of the fires detected by each station.

Figure 12 caption:

Fig. 15 Scatter plots between various two intensive parameters for SE region. The colour code of the points is station related (as labelled in the title). The colour code for the mean and STD values is related with the source origin (as stated on the plots).

20 Figure 12. Scatter plots between various two intensive parameters for SE region (LR@532 vs LR@355, LR@532 vs PDR@532, EAE355/532 vs BAE355/532, EAE355/532 vs BAE532/1064, EAE355/532 vs LR@532 and BAE532/1064 vs BAE355/532). The colour code of the points is station related (as labelled in the title). The colour code for the mean and STD values is related with the source origin (as stated on the plots).

25 Pp 4, line 18, pp 6, line 22: change 60 % to 65 %.

- Based on editor suggestion for part II, we do not discuss any more in Part II the other event for “common fire” analysis (here section 5.1). Thus, we will add few comments here at the end of section 5.1. Note that it was an error on the manuscript: we mistakenly wrote 20150602 instead of 20170602.

30 Initial:

„For the other event with common IP for the same source (20170529-20150602), the smoke was labelled as of ‘single fire’ as no other fires were identified along the backtrajectory. This event will be discussed in the subsequent paper.”

Changed:

35 For the other event with common IP, recorded in Athens and Thessaloniki during 20170529-20170602, the smoke was labelled as of ‘single fire’ as no other fires were identified along the backtrajectory. The common fire occurred on 26<sup>th</sup> of May at midnight in Ukraine (48.171 N, 30.622 E) and it was recorded in Thessaloniki and Athens on 29/05 and 31/05 respectively. BAE@532/1064 value in Thessaloniki was less than half of that in Athens, while BAE@355/532 was larger for Thessaloniki. High BAE corresponds to higher backscatter at smaller wavelengths, which indicates a higher number of small particles. The values in Thessaloniki correspond to a higher number of small size particles (at 355 nm) and with a higher proportion of large particles (at 1064 nm) compared to the ones over Athens. CR<sub>BAE</sub> (colour ratio of the backscatter Ångström exponents) increases from Thessaloniki to Athens (0.22 to 0.78, respectively), which suggests an increase with travel distance (time). As CR<sub>LR</sub>

(colour ratio of the lidar ratios) and EAE (extinction Ångström exponent) were not available to characterize the smoke in terms of age, we classified the smoke as aged based on the duration of the travel time.

Overall, we conclude that the number of common events as well as the number of the common IPs is limited and, thus, no thorough examination of these events is possible. The most important feature of this analysis is that it enables us to quantify the smoke as of ‘single fire’ or ‘mixed’ and hence explain various IP values. This kind of analysis can be successfully applied in the future, when more data become available.

### **Answers to specific comments of the Referee:**

Significant part of the manuscript is dedicated to description of the procedure of data treatment. No question, it is important when large volume of data from different stations is analyzed. Still this is ACP, so may be it is better to put data treatment in Appendix? But this is up to the authors.

Thank you for this suggestion. We moved to Appendix Figs. 5, 6 and 8 as well as Table 2 (now they cite as Figs. S1, S2 and S4, Table S2). The figures and tables were re-numbered. We consider that Chapter 3 on data quality control is not large and thus we would like to keep it in the main manuscript. As different criteria involved in QC are discussed along various steps of the procedure, it is difficult to move sparse parts to Appendix. We moved to Appendix the description of the algorithm to determine the aerosol boundary layer (Section 3 in Supplement).

Data quality is important and Fig.4 probably should illustrate it. However, it rises a lot of questions.

Actually, every plot provides a lot of questions and reader will definitely be confused. The uncertainties should be provided to separate real results from artifacts.

Regarding the examples in Fig. 5 (not 4 as mentioned), we added the uncertainties as suggested. In general, we cannot comment precisely on the accuracy of the optical properties profiles as related to different factors. In the database of Earlinet such information is not provided and therefore we could not investigate how they originated (e.g. calibration region, depolarization constant etc). **The input data in the study were the b-files and e-files containing the optical parameters and associated errors (which were quality checked by Earlinet QC tools and approved by the PIs of the stations).** However, a series of additional quality checks were implemented within our study (discussed in detail in the text). We performed an investigation about the profiles shown in Fig. 5 to show how we managed the IPs values.

For example, in Fig.4a, extinction. in upper layer ( 2000 m) at 532 nm is stable, but at 355 nm it oscillates. Is it real or just artifact?

**Fig. 5a).** In fact, this illustrated the special means of additional quality check that we conducted in our study. Note that large uncertainties were seen for backscatter at 532 nm above  $\sim 3$ km (x-axis not shown at full scale on left plot) and for extinction at 532 nm in the first range bins. Further, depolarization is shown as zero for few hundred meters, which is an artefact. We cannot say for sure if extinction at 532 nm has an artefact but likely 532 channel had some problems at this time. Therefore, we checked if the final IPs data set contains data from this measurement. There is no IP associated with this time stamp. The reason for this is that for these layers we did not detect any fire along backtrajectories and thus the data was dismissed (before any other quality checks).

On Fig.4b the peak of extinction is more narrow than that of backscattering. Why? At 3000 m depolarization at 355 nm becomes larger than at 532 nm. Is it real?

**Fig. 5b).** Extinction profiles for 355 and 532 are extracted from e-file (as mentioned in the text). For this particular case, there is 101 bins ‘smooth running’ (49 bins are used in b-files). Evaluation method is Raman in both b-files and e-files. Regarding the peaks, the extinction profiles may present artefacts towards last validated bins. The data were eliminated above 2.7 km (as provided in e-file). In the paper by Ortiz-Amezscua et al. (2017), the authors show profiles of backscatter and extinction as well as LR and PDR (their Fig. 8) for 00:00-01:00 interval. Their extinction profiles go up to  $\sim 3.5$  km. Unfortunately, they do not report PDR@355nm. PDR@532 is  $\sim 3\%$  (similar with the present plot, but note that their layer is estimated differently). We did not find a fire for this case either, so the data was eliminated from analyses. Most probably, extinction at 532 nm would

have been eliminated when computing the mean values in the layer as we wouldn't have had 90 % of the data available. Looking at closer measurements in our dataset, we found the following PDR mean values in layers as: 23:28 on 08/07 PDR@355=2.96 and PDR@532=3.01, 06:29 on 09/07 PDR@355=2.84 and PDR@532=3.17, 15:22 on 09/07 PDR@355=2.77 and PDR@532=2.87. As seen, the values are very close in value. However, there are regions where PDR@355 > PDR@532.

5 This is possible, and it is reported in literature e.g. Janicka et al. 2017, Harrig et al. 2019, Baars et al. 2019.

In Fig.4c,d when backscattering coefficients at355 nm are calculated, the reference points are not shown and it is not clear, if these exist.

**Fig. 5c-d).** We did not investigate the reference points (nor showed on plots). The reference points are not mandatory variable in the Earlinet database and they are sporadically reported.

10 For **Fig. 5c)** the data processing was performed with in-house (PollyXT) algorithm and we have the following information: @355 'Ref.value 4 50 1/m\*sr at 3500.5m', @532 'Ref.value 1 70 1/m\*sr at 7352m', @1064 'Ref.value 6 0 1/m\*sr at 8300.5m' (all using Photon Counting and Raman as evaluation method). We obtained the following IPs for the three layers (all with BB origin): 2.7 for BAE@355/532 (Ist layer), 2.6, 1.1 and 1.5 for BAE@532/1064, and 2.1, 5.6 and 4.1 % for PDR@532. Due to various criteria, the values for PDR@355 were not estimated.

15 For the plot in **Fig. 5d)** the following information is given in the file (processed with SCC): @b355 'find calibr. interval (width = 500m) between 5000 and 9000m with method: min. of sig ratio; bsc. ratio = 1.0E+000' (backscatter ratio method), @b532 'find calibr. interval (width = 500m) between 3000 and 9000m with method: min. of sig ratio; bsc. ratio = 1.2E+000' (backscatter ratio method), @b1064 'find calibr. interval (width = 500m) between 2000 and 5000m with method: min. of sig ratio; ' (iterative method). We obtained for both layers (with BB origin) the following IP values: 40 and 72 sr for LR@532, 20 2.3 and 0.9 for EAE, 1.7 and 1.8 for BAE@532/1064. As seen, the value of BAE@355/532 and LR@355 could not be estimated due to unreliable profile for backscatter at 355nm. However, we suspect that the backscatter profile at 532 nm is not accurate either (we do not know how ABR=1.2 was chosen).

**Fig. 5e).** Both layers were identified as having BB origin. The following IPs values were calculated: 20 and 31 sr for LR@355, 1.1 and 1.7 for EAE.

25 **Fig. 5f).** Only the second layer was identified as having BB origin. The following IPs were determined. LR@355=46sr, LR@532=91sr, EAE=0.25, BAE@355/532=1.9, BAE@532/1064=0.9, PDR@355=2.8%, PDR@532=2.2 %.

**Fig. 5g).** Only the first layer was identified as having BB origin. The following IPs were calculated: BAE@355/532=1.9, BAE@532/1064=1.3. Due to various criteria, PDR was not estimated.

**Fig. 5h).** This dataset was eliminated as considered to have no BB origin.

30 **Fig. 5i).** All layers have BB origin. The following IPs were calculated: 21sr for LR@355 (Ist layer), 67sr for LR@532 (Ist layer), 1.2 and -0.56 for EAE (Ist and IIInd layer).

Note that all the profiles showing regions with PDR355 > PDR532 belong to the same event (long range transport from North America), recorded over 7-10 July 2013 in Warsaw, Belsk and Cabauw (discussed in part II). PDR is provided only by Warsaw ("waw") for this event and it is in accordance with results reported by Janicka et al. 2017. The PDR values retrieved for the 35 entire three days period are small and very close in value, slightly larger for PDR355. Thus, for eight cases where we had estimates at both wavelengths, we obtained the mean and STD as: PDR355 =  $2.5 \pm 0.5$  % and PDR532 =  $2.4 \pm 0.9$  %.

We would like to mention again that it is hardly possible to thoroughly check each profile manually in full detail because of the very high number of profiles analysed (> 4000 profiles) and also to check how the individual retrievals were performed. We only have access at the final product (optical properties). It was behind the scope of this study to check how the raw data 40 were processed with an in-house algorithm or SCC (to do that, firstly, raw data would have to be available; secondly, this kind of work is a study by itself and it needs huge amounts of resources). Conversely, we focused on post processing quality checks along various steps in the procedure. From these examples, we can see that many IPs were not fulfilling our QC criteria and thus rejected from analyses. We did not investigate in detail such situations when backscatter or extinction at 532 nm is larger than those at 355 nm or when PDR@355 > PDR@532. These situations are very rare but they can be real (e.g. Burton et al., 45 Haarig et al., 2018; Hu et al., 2018; Stachlewska et al., 2018). Haarig et al. (2018) and Hu et al. (2018) report PDR355

> PDR532 for stratosphere while both PDR have larger values (~20%). For troposphere, Haarig et al. report PDR355 = 2 %  $\pm$  4 % and PDR532 = 3 %  $\pm$  2 %. Haarig et al. hypothesize that the missing coarse mode in the size distribution is responsible for the high spectral dependence of PDR. Stachlewska et al. (2018) record in a layer at 2.2 - 2.4 km PDR355 = 1.6  $\pm$  0.2 and PDR532 = 0.3  $\pm$  0.1, this being related to advection of smoke particles.

5 A tremendous work was put on QC of the data analysed in this study. We do not claim it is perfect but we believe that we have eliminate most of unreliable profiles. The purpose of the Table 3 was to show how different datasets were eliminated during various stages, following various criteria.

We add the following statement at the end of section 4.1, describing the Fig. S1.

10 The optical profiles shown in Fig. S1 illustrate the layer estimation and show also various questionable patterns for different optical variables. Our quality checks were meant to eliminate profiles (or parts of profiles) where suspicions in their high-quality arise. The examples shown in a), b) and h) were eliminated as they were considered of non-BB origin (as discussed later). For the profiles in c), all layers have BB origin. Various QC did not allow the estimation of the IPs based on non-reliable backscatter coefficient at 355 nm for second and third layer while PDR@355 was dismissed as well. For d) case, both layers have BB origin. QC did not allow the retrieval of various IPs based on non-reliable backscatter coefficient at 355 nm. For g) 15 case, the first layer was considered as having BB origin. QC did not allow the computation of the mean PDR in the layers. For i) case, all three layers have BB origin. However, the QC allowed the estimation of both LR and EAE for first layer and only EAE for the second layer.

#### References:

20 Burton, S. P., J. W. Hair, M. Kahnert, R. A. Ferrare, C. A. Hostetler, A. L. Cook, D. B. Harper, T. A. Berkoff, S. T. Seaman, J. E. Collins, M. A. Fenn, and R. R. Rogers, Observations of the spectral dependence of linear particle depolarization ratio of aerosols using NASA Langley airborne High Spectral Resolution Lidar, *Atmos. Chem. Phys.*, 15, 13453–13473, doi:10.5194/acp-15-13453-2015, 2015.

Baars, H., Ansmann, A., Ohneiser, K., Haarig, M., Engelmann, R., Althausen, D., Hanssen, I., Gausa, M., Pietruczuk, A., 25 Szkop, A., Stachlewska, I. S., Wang, D., Reichardt, J., Skupin, A., Mattis, I., Trickl, T., Vogelmann, H., Navas-Guzmán, F., Haefele, A., Acheson, K., Ruth, A. A., Tatarov, B., Müller, D., Hu, Q., Podvin, T., Goloub, P., Veselovskii, I., Pietras, C., Haeffelin, M., Fréville, P., Sicard, M., Comerón, A., Fernández García, A. J., Molero Menéndez, F., Córdoba-Jabonero, C., Guerrero-Rascado, J. L., Alados-Arboledas, L., Bortoli, D., Costa, M. J., Dionisi, D., Liberti, G. L., Wang, X., Sannino, A., Papagiannopoulos, N., Boselli, A., Mona, L., D'Amico, G., Romano, S., Perrone, M. R., Belegante, L., Nicolae, D., Grigorov, 30 I., Gialitaki, A., Amiridis, V., Soupiona, O., Papayannis, A., Mamouri, R. E., Nisantzi, A., Heese, B., Hofer, J., Schechner, Y. Y., Wandinger, U., and Pappalardo, G.: The unprecedeted 2017–2018 stratospheric smoke event: decay phase and aerosol properties observed with the EARLINET, *Atmos. Chem. Phys.*, 19, 15183–15198, <https://doi.org/10.5194/acp-19-15183-2019>, 2019.

Haarig, M., Ansmann, A., Baars, H., Jimenez, C., Veselovskii, I., Engelmann, R., and Althausen, D.: Depolarization and lidar 35 ratios at 355, 532, and 1064 nm and microphysical properties of aged tropospheric and stratospheric Canadian wildfire smoke, *Atmos. Chem. Phys.*, 18, 11847-11861, <https://doi.org/10.5194/acp-18-11847-2018>, 2018.

Haarig M., Baars, H., Ansmann, A., Engelmann, R., Ohneiser, K., Jimenez, C., Althausen, D., Bühl, J., Seifert, P., Mamouri, R., Nisantzi, A.: Wildfire smoke in the stratosphere over Europe – first measurements of depolarization and lidar ratios at 355, 532, and 1064 nm, ILRC 29, S2-232, Hefei, China, 2019.

5 Hu, Q., P. Goloub, I. Veselovskii, J.-A. Bravo Aranda, I. Popovici, T. Podvin, M. Haeffelin, A. Lopatin, C. Pietras, X. Huang, B. Torres, and C. Chen, A study of long-range transported smoke aerosols in the Upper Troposphere/Lower Stratosphere, *Atmos. Chem. Phys. Discuss.*, <https://doi.org/10.5194/acp-2018-655>, 2018.

Janicka, L., Stachlewska, I. S., Veselovskii, I., Baars, H.: Temporal variations in optical and microphysical properties of mineral dust and biomass burning aerosol derived from daytime Raman lidar observations over Warsaw, Poland, *Atmos. Environ.*, 169, 162-174, <http://dx.doi.org/10.1016/j.atmosenv.2017.09.022>, 2017.

10 Stachlewska, I. S., M. Samson, O. Zawadzka , K. M. Harenda, L. Janicka, P. Poczta, D. Szczepanik, B. Heese, D. Wang, K. Borek, E. Tetoni, E. Proestakis, N. Siomos, A. Nemuc, B. H. Chojnicki, K. M. Markowicz, A. Pietruczuk, A. Szkop, D. Althausen, k. Stebel , D. Schuettemeyer and C. Zehner, Modification of Local Urban Aerosol Properties by Long-Range Transport of Biomass Burning Aerosol, *Remote Sens.*, 10, 412; doi:10.3390/rs10030412, 2018.

15

20

25

30

### Anonymous Referee #3

Received and published: 22 July 2020

5 We would like to thank the reviewer for the thorough revision of the manuscript and for suggestions! We hope we addressed the comments accordingly.

We use across the text (below) the following highlights:

In red, reviewer's comments.

In black, our comments.

In green, the citations from the manuscript submitted.

10 In blue, the changed text for the revised manuscript.

In magenta, some citations from different papers.

Before answering to the reviewer's questions/comments etc, we would like to indicate a few changes that we have done to the initial manuscript. Those changes are not related with the data processing and analysing or its scientific content but rather with text cosmetics.

15 - added Faculty of Physics for co-author 2)

- in Acknowledgements we added Dominika Szczepanik

- in Funding, we added:

*The research was partially funded by the European Regional Development Fund through the Competitiveness 613 Operational Programme 2014-2020, POC-A.1-A.1.1- F- 2015, project Research Centre for Environment and Earth 614 Observation CEO-Terra, SMIS code 108109, contract No. 152/2016.*

20 - in References we added:

Adam, M., Nicolae, D., Belegante, L., Stachlewska, I. S., Janicka, L., Szczepanik, D., Mylonaki, M., Papanikolaou, C. A., Siomos, N., Voudouri, K. A., Alados-Arboledas, L., Bravo-Aranda, J. A., Apituley, A., Papagiannopoulos, N., Mona, L., Mattis, I., Chaikovsky, A., Sicard, M., Muñoz-Porcar, C., Pietruczuk, A., Bortoli, D., Baars, H., Grigorov, I., and Peshev, Z.: Biomass burning events measured by lidars in EARLINET. Part II. Results and discussions, *Atmos. Chem. Phys. Discuss.*, <https://doi.org/10.5194/acp-2020-647>, in review, 2020.

25 Janicka, L. and Stachlewska, I. S.: Properties of biomass burning aerosol mixtures derived at fine temporal and spatial scales from Raman lidar measurements: Part I optical properties, *Atmos. Chem. Phys. Discuss.*, <https://doi.org/10.5194/acp-2019-207>, 2019.

30 Müller, D., Ansmann, A., Mattis, I., Tesche, M., Wandinger, U., Althausen, D., and Pisani, G.: Aerosol-type-dependent lidar ratios observed with Raman lidar, *J. Geophys. Res.*, 112, D16202, doi:10.1029/2006JD008292, 2007.

- Based on suggestions from Earlinet community, we changed the stations acronyms from two letters to three letters, according to the new nomenclature. This was already implemented in Part II. Thus, all the figures with references at station acronyms (on labels or title) were changed for clarity and consistency. Similar holds for tables.

35 - based on editor's suggestion for Part II, we changed N to North (for N America and N Africa)

- based on suggestions from the editor of Part II, we refer to the stations in the text by the full name instead of using acronyms.

- EAE355/532 was changed to EAE in the text (two instances: pp 11, line 18 and line34).

- a list with the acronyms used in the text was added in Supplement (as in Part II) for consistency. The reference at the acronyms list is mentioned at the end of Introduction.

40 A list of acronyms used in the current work is given in the Supplement (Table S1).

- figs. 10, 11, 12, 13 and 14 (now 7, 8, 9, 10 and 11): we added a), b) etc for each plot for an easier reference. We made small changes to the text and changed the 3 figures caption:

Fig. 10 upper right plot -> Fig. 7 a

In Fig. 10, the first two left plots we show -> in Fig. 7 a-b we show

5 Fig. 10 lower left plots -> Fig. 7 c-d

Figure 7 caption:

Fig. 10. Measurements with the same source at Thessaloniki ('th) and Bucharest ('bu'). Event: 20140909-20140910. Left plots: (first) fires location seen during back-trajectories from each station (colour coded), (second) histogram of the fires occurrence in each geographical grid, (third) longitude and latitude of the fires' location versus fires' occurrence time, (forth) longitude and latitude of the fires' location versus measurement time at the two locations. Right plots: layers' altitude and intensive parameters for each station. Layers measuring the common fire are shown by arrows. The geographical location of the common fire is shown on histogram by an arrow.

Figure 7. Measurements with the same source in Thessaloniki ("the") and Bucharest ("ino") during 20140909-20140910. a) Fires location seen during back-trajectories from each station (colour coded); b) Histogram of the fires occurrence in each geographical grid; c) Longitude and latitude of the fires' location versus fires' occurrence time; d) Longitude and latitude of the fires' location versus measurement time at the two locations; e-i) layers altitude and intensive parameters for each station. Layers measuring the common fire are shown by arrows. The geographical location of the common fire is shown on histogram by an arrow.

Figure 11, left -> Figure 8 a)

20 Fig. 11, right -> Fig. 8 b)

See lower plot of Fig. 10 -> See Fig. 8 b)

Figure 8 caption:

Fig. 11. Backtrajectories and location of fires along backtrajectories within 100 km and +/- 1h for Bucharest ('bu') on 20140909 (left) and Thessaloniki ('th') on 20140910 (right). Lower plots show the altitude (a.s.l.) of the backtrajectories function of time. The fires' time is shown as well (see arrow location). The blue square denotes the geographical location of the common fire. See text for more details.

Figure 8. Backtrajectories and location of fires along backtrajectories within 100 km and +/- 1h for Bucharest ("ino") on 20140909 (a) and Thessaloniki ("the") on 20140910 (b). Lower plots show the altitude (a.s.l.) of the backtrajectories versus time. The common fire location is marked with an arrow. See text for more details.

30 Fig. 12, upper right plot -> Fig. 9 e

blue arrows in Fig. 12 -> blue arrows in Fig. 9 (a-e)

green arrows in Fig. 12 -> green arrows in Fig. 9 (a-e)

magenta arrows in Fig. 12 -> magenta arrows in Fig. 9 (a-e)

Figure 9 caption:

35 Fig. 12. LRT as measured at "at" on 20170713. First two BB layers are considered "mixed" while the third "pure NA". The arrows show the location of the fires (left plot) and the location of the smoke layers (right plot).

Figure 9. LRT as measured over Athens ("atz") on 20170713. a) Location of the fires; b) Histogram of the fires. The North America fires are marked by arrows; c) Fires' coordinates versus fires' occurrence time; d) Fires' coordinates versus measurements time; e) Location of the layers marked by arrows. First two BB layers are considered "mixed" while the third (magenta) "pure NA"; f) – i) Intensive parameters.

The trajectory layer in Fig. 13 is the higher one (light blue). -> The trajectory layer in Fig. 10 c) is the higher one (light blue).

Figure 10 caption:

Fig. 13. Backtrajectories for layers shown in Fig. 12 for Athens ('at') station. First two layers are considered "mixed" while the third is considered "pure N America". See text for more explanation. The squares show the location of the fire.

5 Figure 10. Backtrajectories for layers shown in Fig. 9 for Athens ("atz") station. Layers in a) and b) are considered "mixed" while the layer in c) is considered "pure N America". See text for more explanation. The fire location is marked with an arrow.

Figure 11.... Upper plot shows the location of the fires...-> Figure 11... a) Location of the fires

Figure 11... The bottom plot shows the histogram of the fires -> Figure 11... b) Histogram of the fires

Figure 11 caption:

10 Fig. 14. SE Europe region formed by stations "at", "bu", "po", "sf" and "th". Upper plot shows the location of the fires detected by each station. Note that due to overlap some are not seen. The bottom plot shows the histogram of the fires detected by each station.

Figure 11. SE Europe region formed by stations Athens ("atz"), Bucharest ("ino"), Potenza ("pot"), Sofia ("sof") and Thessaloniki ("the"). a) Location of the fires detected by each station. Note that due to overlap some are not seen. B) Histogram

15 of the fires detected by each station.

Figure 12 caption:

Fig. 15 Scatter plots between various two intensive parameters for SE region. The colour code of the points is station related (as labelled in the title). The colour code for the mean and STD values is related with the source origin (as stated on the plots).

20 Figure 12. Scatter plots between various two intensive parameters for SE region (LR@532 vs LR@355, LR@532 vs PDR@532, EAE355/532 vs BAE355/532, EAE355/532 vs BAE532/1064, EAE355/532 vs LR@532 and BAE532/1064 vs BAE355/532). The colour code of the points is station related (as labelled in the title). The colour code for the mean and STD values is related with the source origin (as stated on the plots).

A list of acronyms used in the current work is given in the Supplement (Table S1).

Pp 4, line 18, pp 6, line 22: change 60 % to 65 %.

25 - Based on editor suggestion for part II, we do not discuss any more in Part II the other event for "common fire" analysis (here section 5.1). Thus, we will add few comments here at the end of section 5.1. Note that it was an error on the manuscript: we mistakenly wrote 20150602 instead of 20170602.

Initial: „For the other event with common IP for the same source (20170529-20150602), the smoke was labelled as of 'single fire' as no other fires were identified along the backtrajectory. This event will be discussed in the subsequent paper.”

30 Changed: For the other event with common IP, recorded in Athens and Thessaloniki during 20170529-20170602, the smoke was labelled as of 'single fire' as no other fires were identified along the backtrajectory. The common fire occurred on 26<sup>th</sup> of May at midnight in Ukraine (48.171 N, 30.622 E) and it was recorded in Thessaloniki and Athens on 29/05 and 31/05 respectively. BAE@532/1064 value in Thessaloniki was less than half of that in Athens, while BAE@355/532 was larger for Thessaloniki. High BAE corresponds to higher backscatter at smaller wavelengths, which indicates a higher number of small

35 particles. The values in Thessaloniki correspond to a higher number of small size particles (at 355 nm) and with a higher proportion of large particles (at 1064 nm) compared to the ones over Athens. CR<sub>BAE</sub> (colour ratio of the backscatter Ångström exponents) increases from Thessaloniki to Athens (0.22 to 0.78, respectively), which suggestss an increase with travel distance (time). As CR<sub>LR</sub> (colour ratio of the lidar ratios) and EAE (extinction Ångström exponent) were not available to characterize the smoke in terms of age, we classified the smoke as aged based on the duration of the travel time.

40 Overall, we conclude that the number of common events as well as the number of the common IPs is limited and, thus, no thorough examination of these events is possible. The most important feature of this analysis is that it enables us to quantify

the smoke as of ‘single fire’ or ‘mixed’ and hence explain various IP values. This kind of analysis can be successfully applied in the future, when more data become available.

**Answers to specific comments of the Referee:**

5 ... However, in the current form I still see room for improvements, both from technical and conceptual aspects.  
Let me start from the principal point of view. For a publication in ACP the described method should be so clear, novel and comprehensive that the same methodology could be applied elsewhere and stands out as an independent result. Reading the manuscript in the current form I was wondering, whether a publication in a data journal with a sound description of according metadata would be an alternative.

10 We committed to bring a contribution to the special issue for EARLINET. As the special issue in AMT was closed, we agreed to submit the manuscripts in ACP (where similar topics, based on algorithms or methodologies were already published, e.g. in this issue: Jimenez et al., 2020; Wang et al 2019, **Papagiannopoulos et al., 2018**; Nicolae et al., 2018 - [https://acp.copernicus.org/articles/special\\_issue834.html](https://acp.copernicus.org/articles/special_issue834.html)). Currently, we are constrained with time and manpower and therefore not able to entirely rewrite, adjust and resubmit the manuscript to another journal. Meanwhile, the Part II paper was 15 also submitted to ACP, the same special issue.

In any case the authors may consider to publish the data in itself. My feeling is that this will be worth it (see below).

We will indeed consider the publication of the selected slot of data and the obtained data products itself in the future. For this we plan to approach Lucia Mona, who has experience in publishing specific Earlinet data slots in repositories.

From a technical point of view the error estimation should be improved. In the manuscript (see my detailed remarks below) 20 the authors state to have a SNR of 2 as a limit and derive astonishingly small error intervals for intensive quantities. To me this does not fit together. I am convinced that a trustful evaluation of backscatter with  $\text{SNR} \geq 2$  is on the edge, but the derivation of extinction or intensive quantities will be impossible. Maybe the  $\text{SNR} > 2$  refers to raw data of individual shots, but the final analysis is done with a coarser resolution? Please make this clear.

25 The input data in analysis are aerosol backscatter, extinction coefficients and particle linear depolarization ratio (along with associated errors). This data is provided into the Earlinet database in a so-called b-files and e-files. Thus, we do not derive any of these variables or their errors. First, we used  $\text{SNR} < 2$  to reject the mean values of the optical properties in the layers (backscatter, extinction, PDR). Second, we used  $\text{SNR} < 2$  to reject IOPs (LR, EAE, BAE). We used error propagation to compute the mean optical properties in the layers and then IOPs. Only during statistics, we computed STD (as 30 stated in the manuscripts). The data in b-files and e-files represents one profile which is the average over dozens of minutes (usually 1 h) and then followed by some smoothing (corresponding to “resolution evaluated”). In most of the cases, the spatial resolution for “resolution evaluated” is identical with the raw resolution (e.g. 7.5 m). During this process, the errors decreased. As mentioned, we do not have the whole picture of how the average profile was computed and smoothed nor how the errors 35 were computed.

35 One possible usage of this paper might be by researchers outside the lidar community for further analysis and then a trustful, transparent error analysis will be mandatory.

The error analysis in this study is very simple. Thus, the input errors associated with each optical property profile (provided in b-files and e-files), are further propagated using error propagation. For the scatter plots and other statistics studies performed in part II paper we used STD (clearly stated).

40 Further, there is hardly any description of underlying lidar data from the EARLINET data base. I was wondering, looking at BAE in Fig 15, whether all lidar stations are using the same boundary condition to assess the backscatter?

As a principle, the boundary calibration for all stations is done with the classical approach – calibration in the aerosol-free range with guessed backscatter value. Therefore, it is not possible that precisely the same boundary condition is used at each station. The boundary condition for backscatter is retrieved by individual stations (with their own algorithms) or, when the retrievals are performed by SCC (Single Calculus Chain), there are several criteria involved. For SCC, we cited D’Amico et

al, 2015; D'Amico et al, 2016; Mattis et al, 2016. See also Pappalardo et al. (2014) who describe EARLINET (see. 3.4 Database content). In Mattis et al. (2016) it is mentioned:

“According to the EARLINET requirements, errors of backscatter coefficients at 355 and 532 nm (1064 nm) have to be below 20% (30 %) or smaller than  $5 \times 10^{-7} \text{ m}^{-1} \text{ sr}^{-1}$  (Matthias et al., 2004).”

5 Users have several options to choose when retrieving the optical parameters. For example, regarding the region of retrieval (Mattis et al, 2016):

“Both, minimum and maximum altitudes are to be provided by the user for each individual product.”

ELDA (EARLINET Lidar Data Analyzer) searches automatically for a calibration region where backscatter coefficient has a minimum (or backscatter ratio is 1).

10 “A calibration window of user-defined width is shifted through the altitude region, where particle-free conditions typically occur (user-defined calibration interval).”

Regarding Fig. 15, here we have plotted BAE. We specified the filtering process for IPs (pp 11, lines 12-13) where we dismiss the BAE data below -1 and above 3.

15 To me, one of the overarching questions (not necessarily to be answered by this paper alone) is “to what extent the information content of lidar data is sufficient to track changes in the microphysical properties of (BB) aerosol”. I assume that the existing data set, presented in this work, is the best and most complete from quality-assured ground based stations we have. Further immediate applications would be to not only apply a fire mask but generally an aerosol emission map to further distinction between pure BB from mixed events. Also, soil and vegetation maps may be included (In the future).

20 Thank you for this comment! Indeed, it would be very interesting to assess if we can track changes in the microphysical properties of (BB) aerosol. For such study, it is important to use the data of the stations that are able to provide input data for the inversion algorithm in each BB layer. We did not attempt a study of the microphysical properties of (BB) aerosol because in spite of the large dataset from 13 stations over 10 years ('best and more complete dataset over 2008-2017'), the number of events where simultaneously 3 backscatter + 2 extinction + 1(2) depolarization data (regarded as optimal input for microphysical inversion) is rather strongly limited. Note that Janicka & Stachlewska 2019 (ACPD, this special issue), derived 25 the optimal data set for such study, where the optical properties were derived on a fine scale specifically to address microphysical inversion. However, in our study, being a consequence of the strict QC and the rigorous fire search, the final IPs dataset with 3+2+1(1) was too small (a few cases). Thus, at this stage was not possible to perform a thorough analysis over microphysical properties. However, a more complete data set should be available now (with the additional contribution from the last 2-3 years). At this stage it is not feasible to answer about the changes in microphysical properties. However, it is indeed 30 worth trying in the future. Note that we aimed to analyse the changes in optical properties by considering several stations measuring the same fire smoke but still had difficulty to gather enough IPs for our BB cases. Anyhow, the approach of “common fire” can be successfully applied for the future (more complete) datasets and both optical and microphysical properties can be studied.

35 Finally, without disclosing much details, we confirm that we continue the research and already started looking further into vegetation type (where the fires occurred). Preliminary results will be shown during ELC 2020. However, so far, we did not consider emission map or soil map, this may be done in future though.

40 A statement that a fire occurred in country XY at coordinates zz can only be the starting point for a deeper analysis. At the end, the question will be what type of vegetation on what kind of ground is burning at a shortage or not of oxygen in dry or moist conditions. These factors will probably later on determine the values of the intensive aerosol parameters. Such a work can clearly not be done by the authors here but shows the value of their data set.

As said, we are starting looking into vegetation type. We did not consider yet the soil type or emission map. Thank you for suggestions!

In section 5 the underlying hypothesis could be sharpened, e.g. by stating that with time / travel distance / max. encountered humidity the AEA, BAE, PDR may change like that : : : and for this reason the North American events may stay out like : : : or in the scatter plots the quantity xxx is plotted vs. yyy

We did not consider humidity in this analysis. Such work was done by Janicka & Stachlewska 2019 (ACPD, this special issue).

5 However, for a specific case in part II paper, we considered indeed the RH values for the results interpretation.

For the scatter plots in section 5, we did not mention X vs Y individually as we referred to all combinations. On page 17, line 8, we have:

Fig. 15 shows the scatter plots for some of the combinations between two IPs.

We propose to change the figure caption to:

10 Figure 12. Scatter plots between various two intensive parameters for SE region (LR@532 vs LR@355, LR@532 vs PDR@532, EAE355/532 vs BAE355/532, EAE355/532 vs BAE532/1064, EAE355/532 vs LR@532 and BAE532/1064 vs BAE355/532). The colour code of the points is station related (as labelled in the title). The colour code for the mean and STD values is related with the source origin (as stated on the plots).

The literature research at the beginning of section 5, was rephrased as following:

15 Initial:

We have focused on several directions to investigate and interpret the measurements by means of the intensive parameters. Here we show examples for each direction, while the comprehensive analysis will be performed in the following paper. According to Müller et al. (2005, 2007, 2016), effective radius of BB particles increases with time (distance), most probably due to coagulation and aggregation of the particles (Reid et al., 2005). On the contrary, EAE decreases with time (distance).

20 While the heaviest particles will sediment during transport, the particles reaching measurement site are still larger than the emitted ones. It was shown that for aged BB particles  $LR@532 > LR@355$  (e.g. Wandinger et al., 2002, Murayama et al., 2004; Müller et al., 2005; Sugimoto et al., 2010, Nicolae et al., 2013). Measurements and retrieved values of effective radius of BB particles showed that the fresh particles have a mean radius around 150 nm, while the aged particles have a radius around 300 - 400 nm (Müller et al., 2007). Particle size depends on many factors such as the combustion type in fires (in-flame

25 or smouldering) or type of vegetation while the smoke aerosol undergoes different physical-chemical processes in atmosphere. (Reid and Hobbs, 1998). Differences between smoke properties in different regions were also found. Thus, smoke particles from Brazil absorb more and scatter less the solar radiation as compared with smoke in N America (Reid and Hobbs, 1998). Müller et al. (2005) observed differences between N America and Siberian smoke over Germany; particles from N America showed smaller size and higher EAE. Veselovskii et al. (2015) tried to relate BAE with EAE and showed that while EAE

30 depends mainly on particle size, BAE depends both on particle size and refractive index, being very sensitive to the latter (see their Fig. 20). In specific conditions, for the region of 0.5-1.5 for EAE,  $BAE@532/1064$  decreases ( $BAE@355/532$  increases) with increasing EAE (see their Figs. 20 and 22). However, in different conditions for particles size, refractive index and fine mode fraction, both BAE can increase with increasing EAE (see their Fig. 19). On the other hand, Su et al. (2008) showed few scenarios for the relationship between  $BAE@532/1064$  and  $EAE@533/855$ , which depend on RH and the contribution of the fine mode fraction. While for a high fine mode fraction in the smoke composition and  $RH < 85\%$ ,  $BAE@532/1064$  increases with increasing  $EAE@533/855$  ( $EAE > 2$ ), for a dominant coarse mode and  $RH < 85\%$   $BAE@532/1064$  decreases with increasing  $EAE@533/855$  ( $EAE < 0.5$ ) (see their Fig. 8). According to Veselovskii et al. (2018),  $PDR532$  decreases with

increasing EAE. In general,  $LR532$  increases with increasing  $LR355$  (e.g. Nicolae et al., 2018). Similarly,  $PDR532$  increases with increasing  $PDR355$  (e.g. Stachlewska et al., 2018).

40 Concluding the findings so far, we expect a colour ratio (CR) for  $LR > 1$  for aged smoke ( $LR@355$  decreases and  $LR@532$  increases with aging smoke) and EAE decreasing with time (distance).  $PDR@532$  increases with time (while EAE decreases). The studies showed no straightforward pattern for CRBAE and CRPDR evolution with time.

changed:

We have focused on several directions to investigate and interpret the measurements by means of the intensive parameters. Here we show examples for each direction, while the comprehensive analysis will be performed in the following paper.

The following results were found in literature regarding the IPs values versus travel distance (time travel):

- effective radius: According to Müller et al. (2005, 2007, 2016), effective radius of BB particles increases with time (distance), most probably due to coagulation and aggregation of the particles (Reid et al., 2005). Measurements and retrieved values of effective radius of BB particles showed that the fresh particles have a mean radius around 150 nm, while the aged particles have a radius around 300 - 400 nm (Müller et al., 2007). Particle size depends on many factors such as the combustion type in fires (in-flame or smouldering) or type of vegetation while the smoke aerosol undergoes different physical-chemical processes in atmosphere. (Reid and Hobbs, 1998). While the heaviest particles will sediment during transport, the particles reaching measurement site are still larger than the emitted ones.
- EAE decreases with time (distance) (e.g. Müller et al., 2005, 2007, 2016)
- Lidar ratio: It was shown that for aged BB particles (big travel time)  $LR@532 > LR@355$  (e.g. Wandinger et al., 2002, Murayama et al., 2004; Müller et al., 2005; Sugimoto et al., 2010, Nicolae et al., 2013). Thus, the colour ratio (CR) for LR, i.e.  $CR_{LR} > 1$  for aged smoke ( $LR@532$  increases more with aging smoke)
- PDR@532 decreases with time (Nisantzi et al., 2014).

The general correlations between IPs were shown:

- In general,  $LR532$  increases with increasing  $LR355$  (e.g. Nicolae et al., 2018; Janicka and Stachlewska, 2019).
- In general,  $PDR532$  increases with increasing  $PDR355$  (e.g. Stachlewska et al., 2018; Janicka and Stachlewska, 2019).

The following differences between smoke properties in different regions were reported:

- smoke particles from Brazil absorb more and scatter less the solar radiation as compared with smoke in North America (Reid and Hobbs, 1998).
- differences between North America and Siberian smoke over Germany: particles from North America showed smaller size and higher EAE (Müller et al., 2005)

The following studies showed different behaviour of BAE versus EAE:

- Veselovskii et al. (2015) tried to relate BAE with EAE and showed that while EAE depends mainly on particle size, BAE depends both on particle size and refractive index, being very sensitive to the latter (see their Fig. 20). On one hand, when the real part of the refractive index increases, the imaginary part is constant, the effective radius for coarse mode and the high fine mode fraction are constant while the effective radius of the fine particles decreases,  $BAE@532/1064$  decreases ( $BAE@355/532$  increases) with increasing EAE (over  $\sim 0.5 - 1.5$  region) (see their Figs. 20 and 22). On the other hand, for a constant refractive index, a fixed effective radius for coarse mode and an increase of the fine mode fraction, both BAE increase with increasing EAE (over  $\sim 0.5 - 1.5$  region). This is visible for different effective radius for the fine particles (see their Fig. 19).
- Su et al. (2008) showed few scenarios for the relationship between  $BAE@532/1064$  and  $EAE@553/855$ , which depend on RH (relative humidity) and the contribution of the fine mode fraction. For a high fine mode fraction in the smoke composition and  $RH < 85\%$ ,  $BAE@532/1064$  increases with increasing  $EAE@553/855$  ( $EAE > 2$ ). For a dominant coarse mode and  $RH < 85\%$   $BAE@532/1064$  decreases with increasing  $EAE@553/855$  ( $EAE < 0.5$ ) (see their Fig. 8). For  $RH > 85$  there is no clear pattern of BAE with respect to EAE (BAE increasing and then decreasing with increasing EAE).

Concluding the findings so far, we expect  $CR_{LR} > 1$ , small values of EAE ( $< 1.4$ ) and smaller  $PDR@532$  for aged smoke (especially for long range transport from North America). The studies showed no straightforward pattern for  $CR_{BAE}$  and  $CR_{PDR}$  evolution with time. Studies by Veselovskii et al. (2015) and Su et al. (2008) may help interpreting the scatter plots between BAE and EAE. We did not investigate the RH field though.

So my opinion on this paper is mixed: provided that the error calculation is revised and honestly be stressed what can or cannot be done with this data set, the scientific significance of the data set is very high. In its current form the papers is lacking substantial novel conclusions, though. Due to the principal importance of this data set and the work the authors performed so far to create

it I rate the scientific significance as “excellent” (provided the error treatment will be revised). Due to the overall quality of the paper in its current form I rate the scientific quality as “low”.

In the Summary and conclusions, (pp 18, line 13) we stated:

..., the quality checks remove a large amount of data (more than half of the initial dataset).

5 Regarding the dataset “potential”, we mention the following. Table 1 shows the data files input along with the corresponding optical properties. As said, there are 2341 files QC by Earlinet (from 3579, i.e. 65%) and 1248 new or reprocessed files (not QC by Earlinet). When working with Earlinet dataset, one has to consider the files mentioned in QC\_2.0 (which passed both QC criteria) which here, represented ~ 65% of the total number of files available. See section 3. The 3589 files (2341 + 1248) analysed correspond to 1138 time stamps. **Table 3 shows how this dataset (1138 time stamps) squeezes along various criteria involved in QC or other checks** (such as fire origin of the pollution layer). Columns 3 and 4 show the dataset after in-house QC of the data and the retrieval of the layers (as layers could not be retrieved for all profiles). Columns 5 and 6 show the chosen data as having BB origin (fire along backtrajectory). Columns 7 and 8 shows the restrained dataset after imposing  $SNR > 2$  for optical properties. Finally, columns 9 and 10 show the final dataset used for data interpretation in terms of IPs, after imposing  $SNR > 2$  for IPs along with a filtering of the IPs data. These steps (with numbers involved) were commented in the text. Thus, if we do a relative difference between columns 1 and 2, we observe that overall, 15.6 % of the initial number of time stamps was rejected due to in-house QC or absence of pollution layers. Further, 29.5 % of the time stamps were eliminated as being considered of non-BB origin (according to our criteria). This corresponds to 44.6 % layers rejected.  $SNR > 2$  for optical properties eliminated just one time stamp (0.1%) and 3 layers (0.3 %). The last criteria rejected 22.2 % of the time stamps and 24.3 % layers. These differences are with respect to previous step. Thus, overall, we have rejected 45.2 % of the time stamps (column 9 with respect to column 3) and 58.2 % of layers (column 10 with respect to column 4). For time stamps, this is on top of 15.6 % time stamps eliminated during QC and estimation of pollution layers. Thus, we have 53.8 % of the time stamps eliminated. As described in section 2.1, Earlinet QC rejected ~ 35 % of the files submitted. Note that we mistakenly wrote ~ 60 % instead of 65 % for selected files. We corrected the value. Our numbers in table 3 refer to the number of time stamps (not to the number of files) and thus it is not straightforward to estimate the number of files rejected. As seen in Table 1, for 1138 time stamps there were 3589 profiles [as for one time stamp we can have from 1 optical property profile (Sofia) to 7 optical properties profiles (Warsaw)]. We did not check how many time stamps corresponded to the rejected files (we did not look at all at those files). For a simple calculation, if we extrapolate from 1138 time stamps/3589 files to x time stamps/1238 files rejected we obtain ~ 393 time stamps eliminated by Earlinet QC (~ 26 %). Thus, overall, we would have 526 time stamps/1531 total time stamps, i.e. a rejection of ~ 66 % for the time stamps. It is not so easy to extrapolate to the total number of files rejected. If we extrapolate 35 % rejected data from 3759 Earlinet QC to the total number 4827 files (3759 Earlinet QC + 1248 not-Earlinet QC) then we obtain a rejection of ~ 47 %.

Figure S4 (former 8) shows an example with the IPs distribution for all the events (the graphs for all stations are shown in Part II). One can see in the plot that there are quite a limited number of events where we have all IPs determined (not considering PDR though).

35 More discussions are present in Part II, where we also mention what can we do and not. For the examples in Part I, one can see the following:

-for Fires events seen by two stations (5.1): the number of IPs to be compared is limited. Thus, for the example chosen here, only BAE@532/1064 can be compared. For the other example with common IPs, the two BAE could be compared. As said, the most important IPs to characterize the aerosol are EAE, CR<sub>LR</sub> and PDR.

40 -for LRT case study (5.2.1), again, the two BAE were the common IPs for the 3 layers analysed. The second layer had the two LR available while the third layer had also EAE estimated.

- the scatter plots between various IPs specific for a geographical region (5.3.2, here SE Europe) is aimed to show a potential pattern between them, based on different continental source origin. As observed, not always we have data for all continental sources which we aimed to find a specific pattern. Part II shows the scatter plots for the other regions. Then we characterize and compare each region function of source origin.

Thus, these examples, for each type of investigation, show that in order to better characterize the smoke, more IPs are needed (ideally, all). In many cases, this was not possible. We would like to emphasize though that the methodology, including the types of investigation is quite robust and can be successfully applied when data proving more IPs is available.

5 A few novel approaches were considered in this study: the smoke layer should have at least one fire along backtrajectory, the quantification of the number of fires contributing to a smoke measurement [here we classified the smoke as having the origin from one fire or more fires (mixed smoke)]. We also classified the smoke from North America as originating solely from North America or being mixed with local fires. Lastly, based on statistical analysis, we divided the stations in four regional clusters and we classified the smoke as having the origin in different continents or many continents (mixed smoke). We regret that these were assessed by the Referee as only “low” scientific quality. However, we agree that the results were not as spectacular  
10 as we initially expected (the main reason being the small final dataset for IPs).

**Some specific remarks are:**

Intro line 19: what do you mean be fuel with respect to climate change?

15 The report states: “Climate change affects forest fires both directly through the weather conditions that affect fire ignition and propagation, and indirectly through its effects on vegetation and fuels.” Fuel refers to the biomass which can burn (combustible material). See types of fuel as type of the biomass on fig. 107 of the study: agricultural field crop, broadleaved forest, grassland, needle forest or mixed. We agree the citation is not clearly stated. We rephrase as:

Initial: As mentioned in the report, climate change affects forest fires through the weather conditions, vegetation and fuel.

Changed: As mentioned in the report, climate change affects forest fires through the weather conditions and through its effects on vegetation and fuels (combustible material),

20 Fig 2, No.8 what are the limits for neglecting intensive parameters, what percentage of data has been rejected?

First, we apologize we forgot to mention “Fig. 2, stage VIII in Methodology” when talking about the calculation of the intensive parameters. Thus, on page 11 we introduce:

Initial: Once the mean optical properties were calculated, the intensive parameters were determined (where possible).

25 Changed: Once the mean optical properties were calculated, the intensive parameters were determined, where possible (Fig. 2, stage VIII in Methodology).

We mentioned in the text the condition  $SNR > 2$  and then the limits (pp 11, lines 12-13):

All the IPs have  $SNR > 2$ . The imposed limits (data filtering) for IPs are the following:  $LR@355 = [20 150]$  sr,  $LR@532 = [20 150]$  sr,  $EAE = [-1 3]$ ,  $BAE@355/532 = [-1 3]$ ,  $BAE@532/1064 = [-1 3]$ ,  $PDR@355 = [0 0.3]$  and  $PDR@532 = [0 0.3]$  (following closely Burton et al., 2012; Nicolae et al., 2018).

30 The percentage of the rejected data can be calculated from Table 3 by comparing columns 9 (# time stamps) and 10 (total # layers) with columns 7 and 8 (either by station or per total). On the same page 11, lines 31-34 we mention the rejected number of values for each IP.

The number of outliers dismissed based on predefined ranges of acceptable values for each intensive parameter is small (3.7% per total). For each IP we have the following numbers: 8/305 (2.6%) for  $LR@355$ nm, 8/253 (3.2%) for  $LR@532$ nm, 18/243 (7.4%) for  $EAE@355/532$ , 39/642 (6.1%) for  $BAE@355/532$ , 21/706 (3%) for  $BAE@532/1064$ , 0/132 (0%) for  $PDR@355$  and 0/242 (0%) for  $PDR@532$ .

35 Section 4 P 7, 1 13: with kappa you mean the extinction, right? Before you have used the symbol “e”

Yes, we use kappa for extinction. We add the list of acronyms in Supplement as we did for Part II. Thus, at the end of Introduction we add (similar with Part II):

40 A list of acronyms used in the current work is given in the Supplement (Table S1).

Symbols „e” and „b” are used only for the data files, as they are stored in Earlinet database (no Greek symbols were used in file names).

L 20: is there a reason for the bin numbers? (the product of resolution \* numbers is not constant) how does this different resolution later affects you layer selection?

5 The choice of the bin number is rather based on trial and error, looking at the input profiles. Please note that even if the raw resolution mentioned in the file was 3.75, 7.5, 15, 30 or 60 m, the smoothed resolution (“resolution evaluated”) for the retrieved data (extinction, backscatter and depolarization) was very different among stations (maybe even different for the same station). As mentioned in the text it was almost impossible to extract the information about how the errors were calculated and how the 10 smoothing was performed. Some information is given as a (free style) comment in the general attributes but it is almost impossible to quantify it as we dealt with few thousands of profiles which can have hundreds of free style comments. Please note that this smoothing in this stage is used only to determine the layers. The optical properties are calculated based on input data as it is in the netCDF file. As mentioned, the automatic retrieval for layers boundaries has limitations and that’s why we double check visually the layers. Where there were non-accurate boundaries, we adjusted them “by hand”.

P8, L 4: I do not understand the possibility that a maximum is not surrounded by 2 minima. *findpeaks* is employed for beta1064, 15 i.e. real data, so I assume intervals with constant values are at least not frequent?

Sometimes there is the possibility that a maximum is not surrounded by two minima. Theoretically, there are two minima but the criteria employed with the function *findpeaks* can eliminate one of the minima (e.g. criterium at line 3). In example 5i) we can see that in layers 2 and 3 there are more local maxima and minima but finally only one maximum is chosen.

I am not sure what you refer to when mentioning intervals with constant values. There are intervals with more or less constant 20 values. As it is almost impossible to have identical values over an interval, the function can see more (local) maxima and minima. However, adjacent maxima are eliminated (as said on line 1) based on “prominence width”. Further, the algorithm can determine the minima behind the two maxima. In the worst case, we adjust manually.

P8, L 7: in which way this last criterion is independent from the others (and hence needed)?

You are right, it looks redundant. We eliminate this sentence and we add in parenthesis the following to the previous statement:

25 Initial:

- a maximum peak should be bordered by two minima; when the first or the last minimum is missing, a criterion is used to add the missing minimum; thus, the minimum is chosen at a location ( $> 300$  m from the first or the last maximum peak) where the optical property has the minimum value

Changed:

30

- a maximum peak should be bordered by two minima (which defines the layer boundaries); when the first or the last minimum is missing, a criterion is used to add the missing minimum; thus, the minimum is chosen at a location ( $> 300$  m from the first or the last maximum peak) where the optical property has the minimum value

L24/25: “Our approach : : : in line with : : :” this statement is completely unproven. Maybe you do not need it but to prove it you should apply your code to one of the examples of the mentioned papers.

35 The comparison with different authors was based on visual inspection of their retrievals for layer’s boundaries. We did not intend to apply the algorithm to those examples (not even think about!). It is not a matter of an algorithm but rather a matter of personal choice/criteria on how to choose the boundaries (which is the input for the development of an algorithm). Recall that in general, the research papers deal with case studies and in most of the cases, the boundaries are chosen by visual inspection.

40 P9 L 15 and 16: where is table S2? In my version of the manuscript the citations are not numbered.

Table S2 (now S4) is in Supplement (now page 12).

P10, L 24 I do not understand the definition of data availability: Isn't the ratio between layer thickness and resolution simply the number of data points? Did you use an additional criterion to flag a given data point as valid?

The number of data points in the layer is indeed the ratio between layer thickness and resolution. In order to evaluate (calculate) the mean, we impose (criterion) that 90% of the points to be available. The confusion might come from the fact that we have 5 100% of the points are available for the profile used to determine the layer's boundaries (e.g. b1064) but we might not have 100% available for the other profiles (other backscatter and extinction). In general, the extinction profiles are shorter. In order to compute an intensive parameter in a layer, we should have  $\sim$  the same number of points available in both backscatter and extinction otherwise we do not calculate over the same structure (layer).

The points which are not valid in a layer are simply NaN in the data file. Thus, NaN values should be below 10%.

10 P11, L 11 and following: is SNR  $\geq 2$  really sufficient to determine particle extinction and lidar ratio? The SNR of the underlying Raman channel must have been much better, I assume. Fig 9 is interesting. However, presented like this: almost spherical particles, very high LR and very small particles I am wondering whether this is really BB or anthropogenic pollution. It would be interesting to show the hysplit trajectories for the extreme cases (maybe 2015, 2016, 2017).

15 **The particles extinction, backscatter and depolarization are provided in the data files with associated errors.** The Earlinet database is not provided with the details involved to calculate and validate the optical properties (including errors). By definition, they are Earlinet quality checked and approved by PIs once they are in the database. Additional quality checks can be performed by users.

20 As seen in Fig. 1 (methodology scheme), one can see that the SNR is not referring the lidar signals (which indeed with SNR of 2 likely would not be sufficient to obtain optical properties). As in Fig.1, we apply this criterion on profiles of optical properties not signals, whereby at first, the mean values of the optical properties derived in the layers containing BB are kept only if  $\text{SNR} > 2$ . Then, we calculate the intensive parameters and keep them for analyses if their  $\text{SNR} > 2$ .

25 We have difficulty to understand what you refer to when talking about Fig. 9. This figure shows all the data available (in terms of IPs) for this station. As we can see, the min-max values range for each IP (as reported in literature) is quite large and surely it depends on the measurement site and characteristics of particular BB event and thus we have both small and large values for each IP.

30 As for the IPs in Warsaw, they are quite well spread within the limits, except for PDR. However, taking into account that upper limits reported in literature of 0.2 at 532 and 0.38 at 355 are very high and more in the range of values expected for mineral dust particles not smoke particles. For BB events reported at Warsaw station the PDR in general has a lower upper values limit that this reported in literature (i.e. below 0.18 at 532 and 0.12 at 355), hence here BB shape is closer to spherical particles. The LR and EAE spread over a large range of values, and thus we can have both smaller (high EAE) and larger (small EAE) particles. Unfortunately, we did not investigate the potential contribution of other types of pollution in these layers (it would have been another enormous work to be done for 1901 layers) and we assumed as being of BB origin only. Also, for the values reported in literature – we had no means to investigate to which extend the BB events were contaminated e.g. with mineral dust or pollution.

35 Note that the lower limit for literature values for BAE@532/1064 was missing in Fig. 9. **We added it.**

For a better explanation (hopefully) we changed the following:

Several values outside the literature range are observed for EAE, both BAE and PDR@355 for Warsaw.

40 In general, LR, EAE, both BAE and PDR are spread well within the reported limits, although the latter is rather in its lower range. Lower PDR may be explained as due to specific location of Warsaw being much closer to BB sources in Ukraine, Belarus and Russia than other EU countries, and therefore much more exposed to faster and more direct BB transport to this site. In such case, differences of properties with respect to other measurement sites in Europe are expected and revealed within our work. Moreover, Warsaw is much less exposed to mineral dust intrusions, in comparison with many EU sites at which the BB measurements are more likely to be affected by slight contamination of dust, e.g. Spanish sites. On the other hand, Warsaw is an urban site, thus for BB observed in layers at lower ranges a slight contamination of the BB with the local urban pollution 45 is possible. For higher layers, industrial pollution from Silesia region in Poland (Stachlewska et al. 2018) or Ruhr region in

Germany (e.g. case here on 20160704 at 07:30) is possible. This can explain a few values outside the literature range observed in Warsaw, i.e. for EAE (2 values), for both BAE (33 values) and for PDR355 (8 values). The extreme values for EAE observed on 20160704 07:30 and 20170619 20:30 (2.6 and 2.8 respectively along with  $CR_{LR} < 1$ ) correspond to fires in Germany / Belgium and United Kingdom respectively. The fires occurred in less than 40 h before smoke measurements and thus we can consider the smoke relatively fresh.

We are not sure to which extreme cases you refer to and thus we try to guess. Looking at the two EAE extreme values in 2016 and 2017, we checked the backtrajectories.

The two extreme points for EAE from 2016 and 2017 corresponds to the time stamps:

1) 20160704 07:29:30

2) 20170619 20:29:30

Note that the times are the middle of the time interval (so the input files have a time with  $\sim 30$ min before).

Both events had two layers but for the second layers not all IPs were retrieved.

These are the IPs values:

15 Altitude LR355 LR532 EAE BAE355/532 BAE532/1064 PDR355(%) PDR532(%)

1)

2088m 114+-/6 65+-/3 **2.6+-/0.15** 1.2+-/0.05 0.87+-/0.03 N/A 3.3+-/0.03

5095m N/A N/A N/A N/A 1.7+-/0.05 N/A

2)

20 2417m 64+-/2 35+-/3 **2.8+-/0.2** 1.32+-/0.07 0.84+-/0.04 1.65+-/0.02 3.2+-/0.04

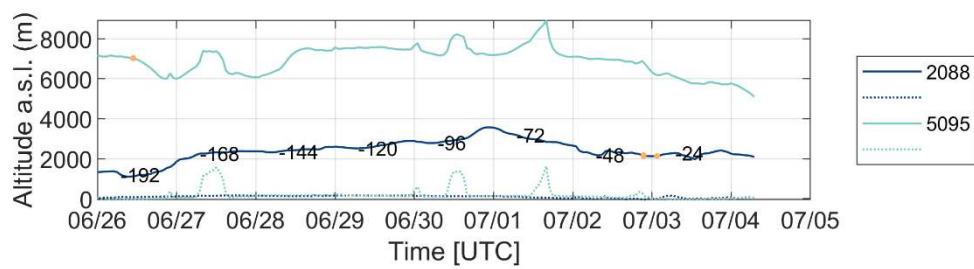
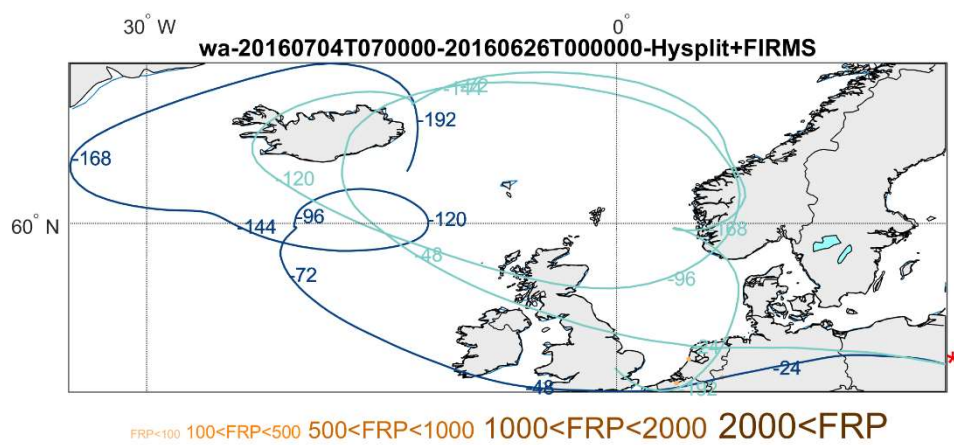
3306m N/A N/A N/A 1.64+-/0.04 0.94+-/0.03 1.5+-/0.01 2.5+-/0.02

Below are the FIRMS-Hysplit plot for these events. The two extreme EAE values correspond to the first layer.

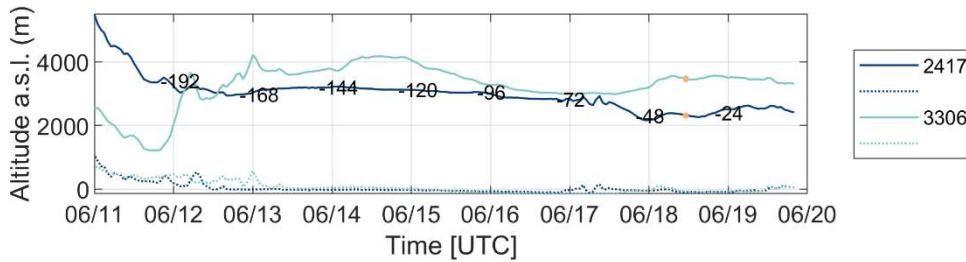
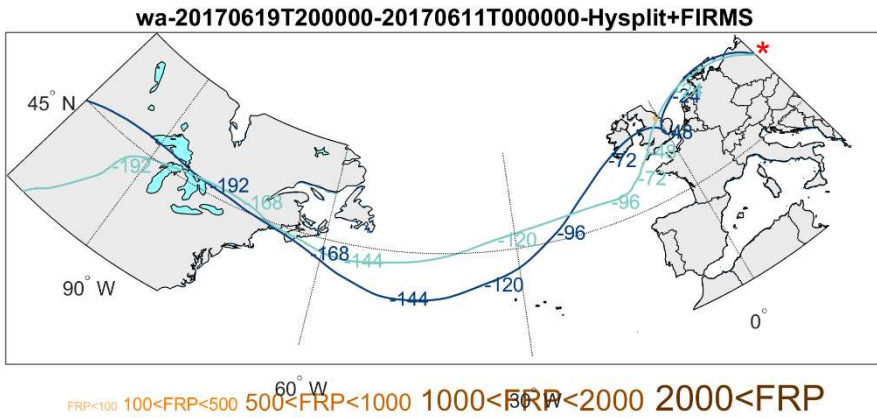
25 Looking into firms-hysplit plots we see:

- 1) The fires along backtrajectory for the first layer are located in Germany and Belgium and are detected somewhere between 24h and 48h back. The second layer 'detects' one of the fires seen by first layer but after  $\sim 192$ h.
- 2) The fires along backtrajectory for the first layer are located in UK and are detected somewhere between 24h and 48h back. Actually, both layers 'detect' the same fire at  $\sim$  the same time. The fire is closer to the second backtrajectory (second layer).

Taking into account that the fires are seen somewhere after around 36 h back we can say it is relatively fresh (and thus high EAE and  $CR_{LR} < 1$ ). The other IPs are within literature limits.



Plot above: Illustration of Event 1) 20160704 07:29:30



Plot above: Illustration of Event 2) 20170619 20:29:30

5 P13 L2: Sorry, I missed that: why PDR (at 532) increases with time? I would have assumed that coagulation makes the particle shape more spherical

The statements at the beginning of the page 13 are based on literature review, discussed on the previous page. However, we erroneously cited Veselovskii et al. (2018) where PDR@532 is shown as increasing while EAE decreases (a decrease of EAE being related with longer travel time). Revising their plot (Fig. 10) we realize that it is based on data from both smoke and dust while EAE range is between 0 and 0.9. At a more careful reading, PDR@532 from smoke is below 10%. Linked with corresponding EAE on the plot, we do not see any correlation for smoke. We deeply apologize for this misunderstanding. On the contrary, we have cited Nisantzi et al. (2014) in Part II which reported PDR@532 decreasing with time. We remove the statement and add the reference to Nisantzi et al. (2014). However, the entire paragraph is rephrased as suggested (shown above).

10 Remove: PDR@532 increases with time (while EAE decreases).

15 Changed: PDR@532 decreases with time (Nisantzi et al., 2014).

P13 L 6 (and P14 later) I would omit mentioning Fig 2 for things which the reader cannot verify on his own.

We are sorry but we did not understand the comment. In Fig. 2 we mentioned the most important steps in methodology. From stage IX we refer to specific analysis indeed. The intention was to point out to a specific stage of the methodology when we start a new section (discussion).

P14, L 7-8 the errors in the IP are unbelievable small and non-proven. If this is the error of many different measurements, you rely on the fact that the aerosol layer did not change during the sampling. Contrary, the different BAE between “bu” and “th” are much more understandable, if the fire conditions, the heat, the burning plants the amount of water vapour :: etc changed.

Indeed, the uncertainties are quite small. The IPs have the errors propagated based on uncertainties provided for the optical properties. The optical profiles represent one single profile over 1-h measurement. According to the station PI, the air mass sampled during this one hour seems not to change. Also, it has to be noted that the uncertainty is calculated without considering the systematic biases (e.g. the uncertainty of the estimated constant lidar ratio over the profile).

In general, we have observed small uncertainties for many IPs and many stations. This fact can be seen in Part II where all the data are shown in Supplement. The mean, median, min and max values for IPs, for each station, are shown in Part II (Table 10 1). There, we can see that the values of the uncertainties for BAE (median and minimum) for Bucharest station are among the smallest.

To double check, we have recalculated the values for BAE for the example in Fig. 10. We obtained the same values for both stations.

We mentioned in 2.2 (metadata), pp 5, lines 24-25 that “we could not determine which was the final spatial resolution nor the 15 method used for smoothing and error calculation”.

For this example, for Bucharest station, the information provided in the attributes of the netCDF files about effective resolution is vague (‘resolution evaluated’: ‘Linearly increasing from 7.50m to 1500.00m’). For Thessaloniki case, the data processed with SCC provide a new variable called ‘VerticalResolution’. The vertical resolution for this case is 7.5 m for 355 nm and 532 nm and 15m for 1064 nm everywhere, i.e. the same as for raw data resolution. Basically, there is no smoothing here and thus, 20 we expect larger uncertainties as compared with smoothed profiles for Bucharest. In addition, there were 35400 shots and 18000 shots averaged for Bucharest and Thessaloniki respectively.

As mentioned in the manuscript, it is very challenging to work with thousands of data files from 14 stations, using 14 different 25 algorithms, several methods for deriving optical properties, many ways to smooth data and to choose the resolution and other many ways to compute the errors. The Earlinet community keeps improving SCC algorithm and thus, all the data will be treated in the same manner in the future. However, keep in mind that the user still has to add few input information (e.g. min and max altitude to be used, windows for searching the calibration region). Earlinet has a tool for QC, the PI has to approve the data before uploading to Earlinet. Still, any user which uses Earlinet database does his/her own QC. We did our best to reject suspicious data in this study.

## 1 List of acronyms

**Table S1. List of acronyms**

<u>Nomenclature</u>	<u>Definition</u>
<u>ACTRIS</u>	<u>Aerosol Cloud and Trace Gases Research Infrastructure</u>
<u>a.g.l.</u>	<u>Above ground level</u>
<u>a.s.l.</u>	<u>Above sea level</u>
<u>"atz", "brc", "cog", "ino", "cbw", "evo", "gra", "lei", "mas", "hpb", "pot", "sof", "the", "waw"</u>	<u>Athens, Barcelona, Belsk, Bucharest, Cabauw, Evora, Granada, Leipzig, Minsk, Observatory Hohenpeissenberg, Potenza, Sofia, Thessaloniki and Warsaw (lidar stations considered in this study).</u>
<u>BAE</u>	<u>Backscatter Ångström exponent. <math>BAE@355/532 = -\log(\beta_{p355}/\beta_{p532})/\log(355/532)</math>, <math>BAE@532/1064 = -\log(\beta_{p532}/\beta_{p1064})/\log(532/1064)</math></u>
<u>BB</u>	<u>Biomass burning</u>
<u><math>\beta_p</math></u>	<u>Particle backscatter coefficient [1/m/sr]</u>
<u>CR(s)</u>	<u>Colour ratio(s). <math>CR_{LR} = LR@532/LR@355</math>, <math>CR_{BAE} = BAE@532/1064/BAE@355/532</math>, <math>CR_{PDR} = PDR@532/PDR@355</math></u>
<u>EAE</u>	<u>Extinction Ångström exponent. <math>EAE@355/532 = -\log(\kappa_{p355}/\kappa_{p532})/\log(355/532)</math></u>
<u>EARLINET</u>	<u>European Aerosol Research Lidar Network</u>
<u>EU, AF, NA, AS</u>	<u>Europe, Africa, North America, Asia continental source regions</u>
<u>EUAF, EUNA, EUAS</u>	<u>Europe + Africa, Europe + North America, Europe + Asia continental source regions</u>
<u>FIRMS</u>	<u>Fire Information for Resource Management System</u>
<u>FRP</u>	<u>Fire radiative power</u>
<u>GDAS</u>	<u>Global Data Assimilation System</u>
<u>HYSPLIT</u>	<u>Hybrid Single-Particle Lagrangian Integrated Trajectory model</u>
<u>IP(s)</u>	<u>Intensive parameter(s)</u>
<u><math>\kappa_p</math></u>	<u>Particle extinction coefficient [1/m]</u>
<u>LR</u>	<u>Lidar ratio [sr]. <math>LR@355 = \kappa_{p355}/\beta_{p355}</math>, <math>LR@532 = \kappa_{p532}/\beta_{p532}</math></u>
<u>LRT</u>	<u>Long range transport</u>
<u>MODIS</u>	<u>Moderate Resolution Imaging Spectroradiometer</u>
<u>PDR</u>	<u>Linear particle depolarization ratio</u>
<u>QC</u>	<u>Quality control</u>
<u>SE, SW, CE and NE</u>	<u>Southeast, Southwest, Central and Northeast Europe (geographical measurement regions)</u>
<u>SNR</u>	<u>Signal to noise ratio</u>
<u>STD</u>	<u>Standard deviation</u>

## 2 Summary of metadata

**Table S2. Summary of main features used to calculate the backscatter and extinction coefficient, specific for each b-files and e-files.**  
**Detection mode: 1 (photon counting), 2 (analog), 3 (analog + photon counting). Evaluation mode: 1 (Klett-Fernald), 2 (Raman), 3 (aerosol backscatter ratio).**

	<u>Detection mode (1/2/3)</u>	<u>Evaluation method (1/2/3)</u>	<u>Raw resolution</u>	<u>Shots averaged</u>	<u>Zenith angle</u>
b355	<u>176/153/590</u>	<u>524/130/257</u>	<u>most@3.75m and 60m</u>	<u>most@1e4</u>	<u>most@0°</u>
e355	<u>417/0/107</u>	<u>0/516/0</u>	<u>most@60m</u>	<u>most@1e4</u>	<u>most@0°</u>
b532	<u>229/199/385</u>	<u>335/296/174</u>	<u>most@3.75m, then 7.5m, 15m, 60m</u>	<u>most@1e4</u>	<u>most@0°</u>
e532	<u>409/0/94</u>	<u>0/496/0</u>	<u>most@60m</u>	<u>most@1e4</u>	<u>most@0°</u>
b1064	<u>222/608/0</u>	<u>683/139/0</u>	<u>most@3.75m, then 15m and 60m</u>	<u>most@1e4</u>	<u>most@0°</u>

5

10

15

20

### **3 Calculation of the aerosol layers boundaries**

The following approach was considered to calculate the boundaries of the aerosol layers. The order of selecting the optical profile to determine the boundaries of the aerosol layers is the following:  $\beta p1064$ ,  $\beta p532$ ,  $\beta p355$ ,  $\kappa p532$ ,  $\kappa p355$ . In other words, when available, use  $\beta p1064$ . When  $\beta p1064$  is not available, use  $\beta p532$ . If the latter is not available either, use  $\beta p355$  and so on. Note that for the times when none of the profiles showed a pollution layer, all profiles for that specific time were excluded.

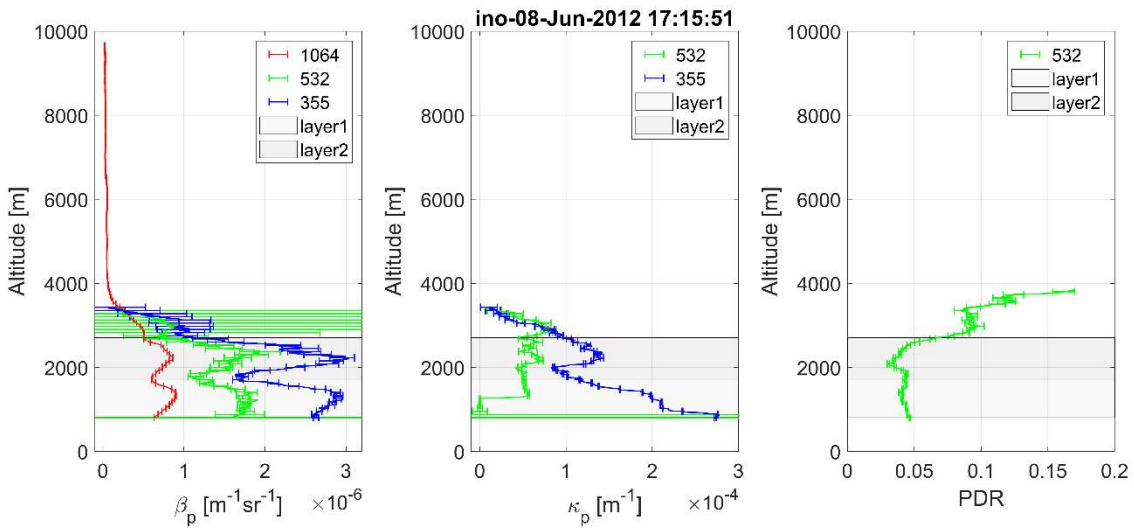
Once the optical profile (including the associated error profile) and the corresponding altitude profile are available, the algorithm developed to determine the aerosol layers boundaries is run. The steps of the algorithm are the following:

- Perform a smoothing of the optical profile. The number of bins used for smoothing depends on the input resolution. Thus, for a resolution of 3.75 m, we applied moving average over 23 bins. For a resolution of 7.5 m, 15 m, 30 m, 60 m, we used 11 bins, 9 bins, 7 bins and 3 bins, respectively. For the particular cases of “ca” and “oh” systems, we applied a number of bins of 15 and 19, respectively (as the signals were very noisy). The corresponding errors were propagated.
- Employ the function *findpeaks* from Matlab ([www.mathworks.com](http://www.mathworks.com), last access 20191126) to find the maxima, with the following options: the minimum distance between peaks is 300 m (*MinPeakDistance*) and the minimum peak height (*MinPeakHeight*) is as follows: 1e-7 for  $\beta p1064$ , 1.5e-7 for  $\beta p532$ , 3e-7 for  $\beta p355$ , 1e-6 for  $\kappa p532$  and 3e-6 for  $\kappa p355$ . The value of the minimum distance between peaks was chosen as in Nicolae et al. (2018). If no peaks are found, the routine returns the message no layers with maximum above *MinPeakHeight*.
- Employ the function *findpeaks* to find the minima, with the following option: the minimum distance between peaks is 300 m (*MinPeakDistance*)
- eliminate adjacent maxima if the “prominence width” (<https://www.mathworks.com/help/signal/ug/prominence.html>, last access 20191126) overpasses the position of the adjacent maxima
- eliminate small maxima / minima peaks which are smaller than 10% of the maximum / minimum peak
- a maximum peak should be bordered by two minima (which defines the layer boundaries); when the first or the last minimum is missing, a criterion is used to add the missing minimum; thus, the minimum is chosen at a location ( $\geq 300$  m from the first or the last maximum peak) where the optical property has the minimum value

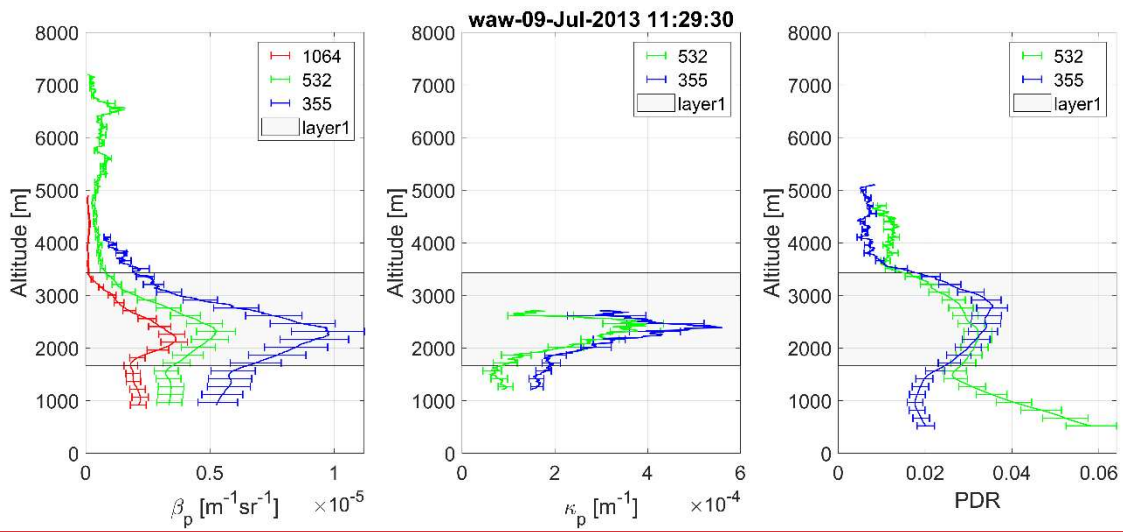
Following the criteria discussed, there can be cases when it is not possible to find any aerosol layer. Consequently, those profiles were dismissed. Additionally, a manual check was performed and for the cases with non-accurate estimation of the boundaries, the boundaries were manually corrected ( $\sim 40$  % of the cases) and sometimes, we added layers which had a maximum below the threshold of the minimum peak height. Thus, we cope with a semi-automatic algorithm. Table 3 shows the number of time stamps when it was possible to determine a layer and at least one optical property could be calculated (column 3). Recall that many profiles were dismissed manually through quality check before we apply the algorithm for layer boundary evaluation and this explain most of the “missed” cases (difference between second and third columns). The initial

total number of layers, with at least one optical property (column 4) is greater than the time series (column 3) as most of the times we have more than one layer within a profile. The other columns are discussed in the next section. Overall, we were able to determine 1901 layers for 960 time stamps (out of 1138 in total).

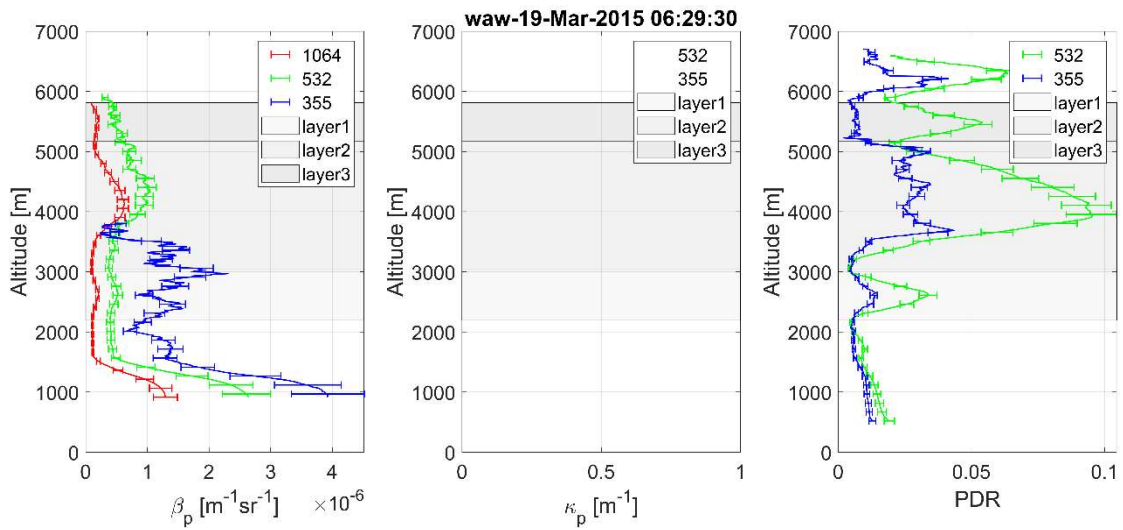
Various authors use different criteria to estimate the layer boundaries. In most of the papers examined, the authors do not 5 describe how they determined the boundaries of the layers. However, the boundaries can be easily identified visually (a common practice when investigating one or few cases). In a few studies it is mentioned the gradient method (Giannakaki et al., 2015; Mattis et al., 2008; Ortiz-Amescua et al., 2017; Preißler et al., 2013). When intensive parameters are available (e.g. 10 EAE or LR), one can determine the boundaries based on intensive parameters being nearly constant in the layer (e.g. Samaras et al., 2015) or based on the ratio of elastic to Raman profiles (Vaughan et al., 2018). In situations when a few layers are visible, one can choose them as a single large layer (e.g. Ansmann et al., 2009). Our approach provides the layers boundaries in line with those shown by Ansmann et al. (2009), Janicka et al. (2017), Hu et al. (2018), Veselovskii et al. (2018).



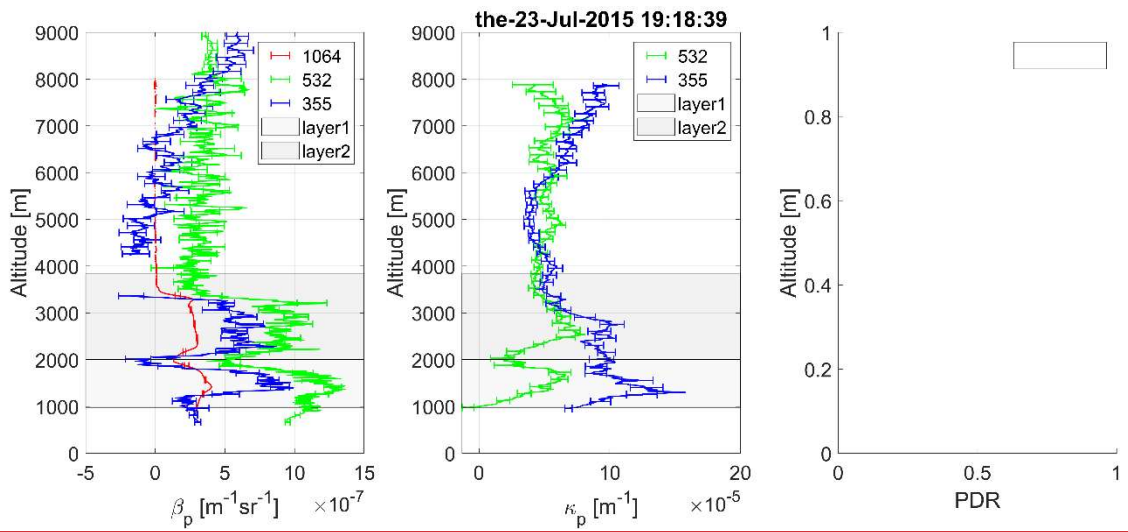
a) Two layers automatically selected based on  $\beta_{1064}$  signal. Layers' boundaries are: [802 1717] m and [1717 2707] m.



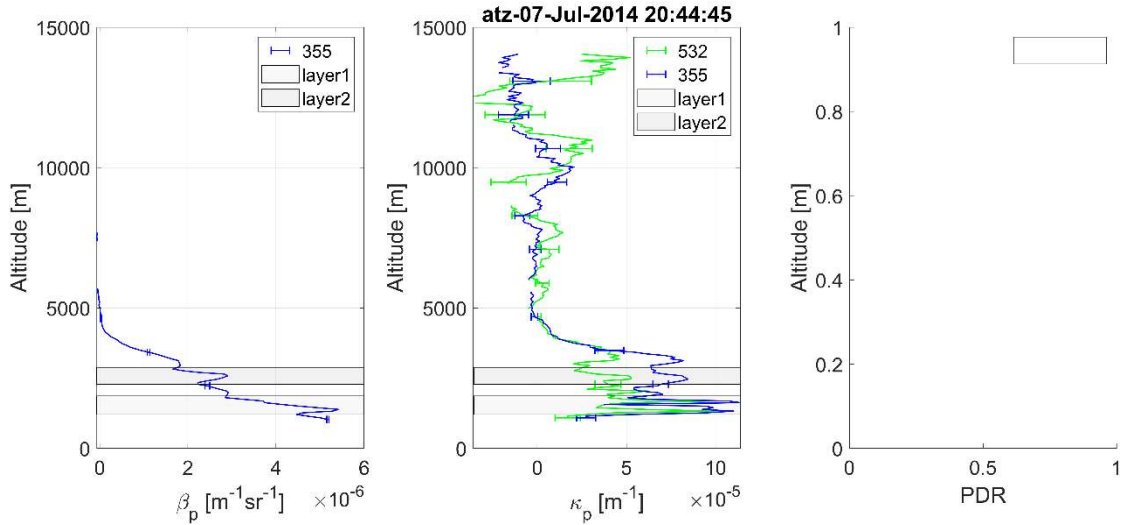
b) One layer automatically selected based on  $\beta_{1064}$  signal. Layer' boundaries are [1670 3426] m.



c) Three layers automatically selected based on  $\beta_{1064}$  signal. Layers' boundaries are [2193 3037] m, [3037 5166] m and [5166 5809] m.

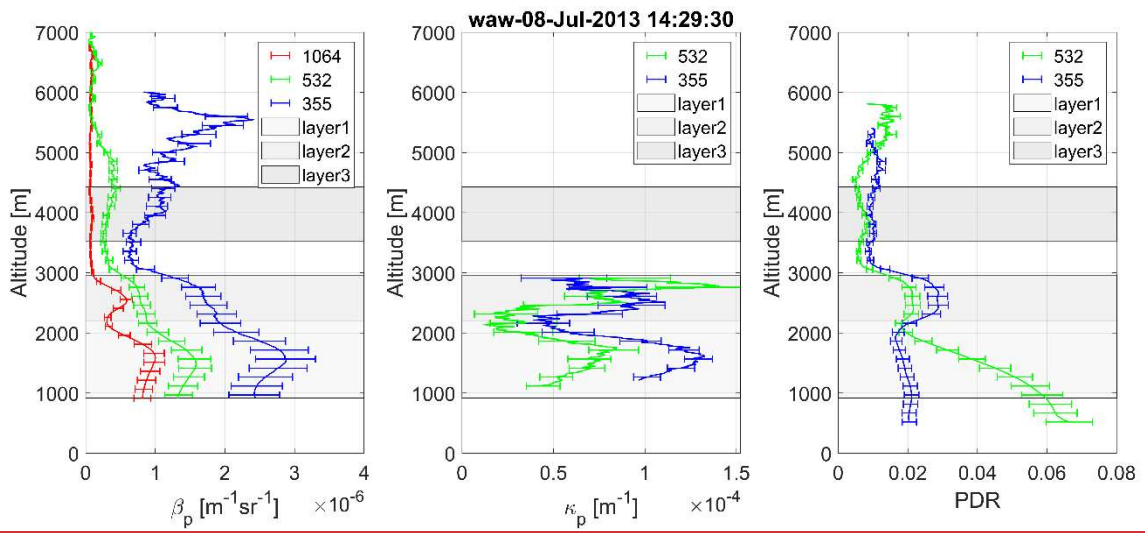


d) Two layers automatically selected based on  $\beta_{1064}$  signal. Layers' boundaries are [968 2002] m and [2002 3847] m.

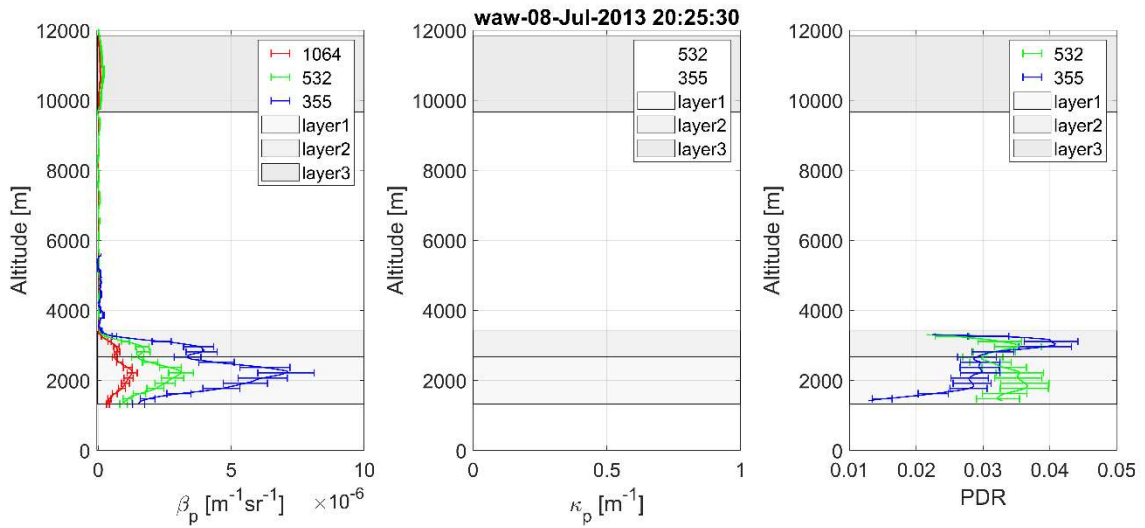


5

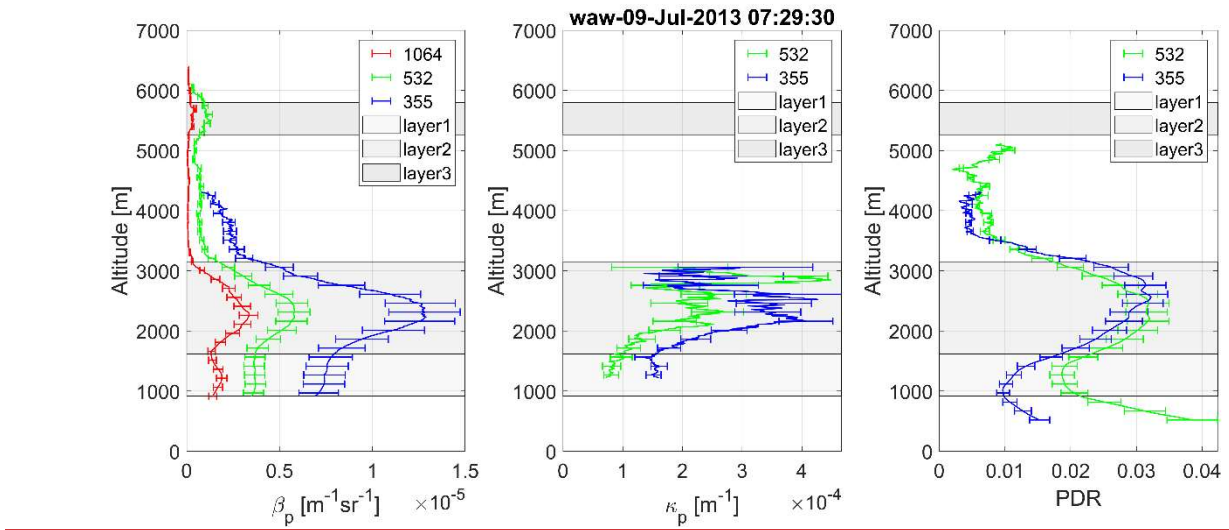
e) Two layers automatically selected, based on  $\beta_{355}$  signal. Layers' boundaries are [1202 1862] m and [2282 2882] m.



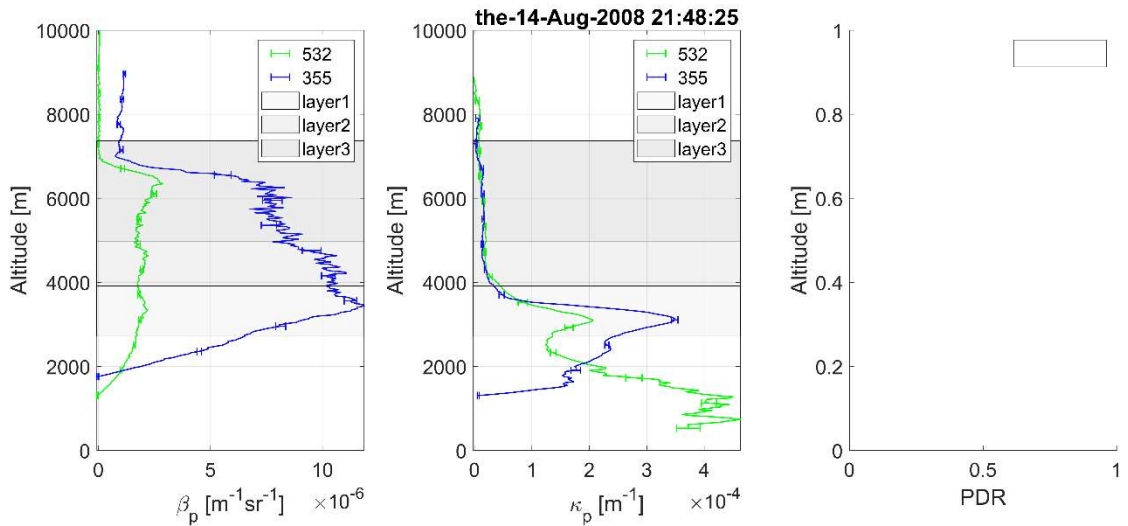
f) Three layers selected based on  $\beta_{1064}$  signal. Layers' boundaries are [915 2193] m, [2193 2962] m and [3530 4427] m. The top of the second layer was manually changed from 3530 m to 2962 m. A fourth layer around 6500m was dismissed.



5 g) Three layers selected based on  $\beta_{1064}$  signal. Layers' boundaries are [1319 2678] m, [2678 3411] m and [9664 11846] m. The third layer was added manually. The top of the second layer was modified from 4061 m to 3411 m.



**h) Three layers detected based on  $\beta_{1064}$  signal with the boundaries [915 1617] m, [1617 3142] m and [5264 5801] m. The top of the second layer was manually modified from 3612 m to 3142 m.**



5

**i) Three layers selected, based on  $\beta_{532}$  signal. Layers' boundaries are [2715 3915] m, [3915 4965] m and [4965 7365] m. The bottom of the second and third layers were manually changed from 4485 m to 3915m and from 5295 m to 4965m.**

Figure S1. Examples of layers selection, based on  $\beta_{1064}$  signal (a-d, f-h),  $\beta_{532}$  signal (i) and  $\beta_{355}$  signal (e). Layers are shown by grey areas. All available optical properties are shown (particles backscatter coefficients  $\beta_p$  on the left, particles extinction coefficients  $\kappa_p$  in the middle and particles linear depolarization PDR on the right). The boundaries shown in a-e plots are the automatic output of the algorithm. In the f-i plots, one or more boundaries retrieved by the algorithm were manually adjusted.

## 2. Example number of layers selected and corresponding optical parameters available for each layer

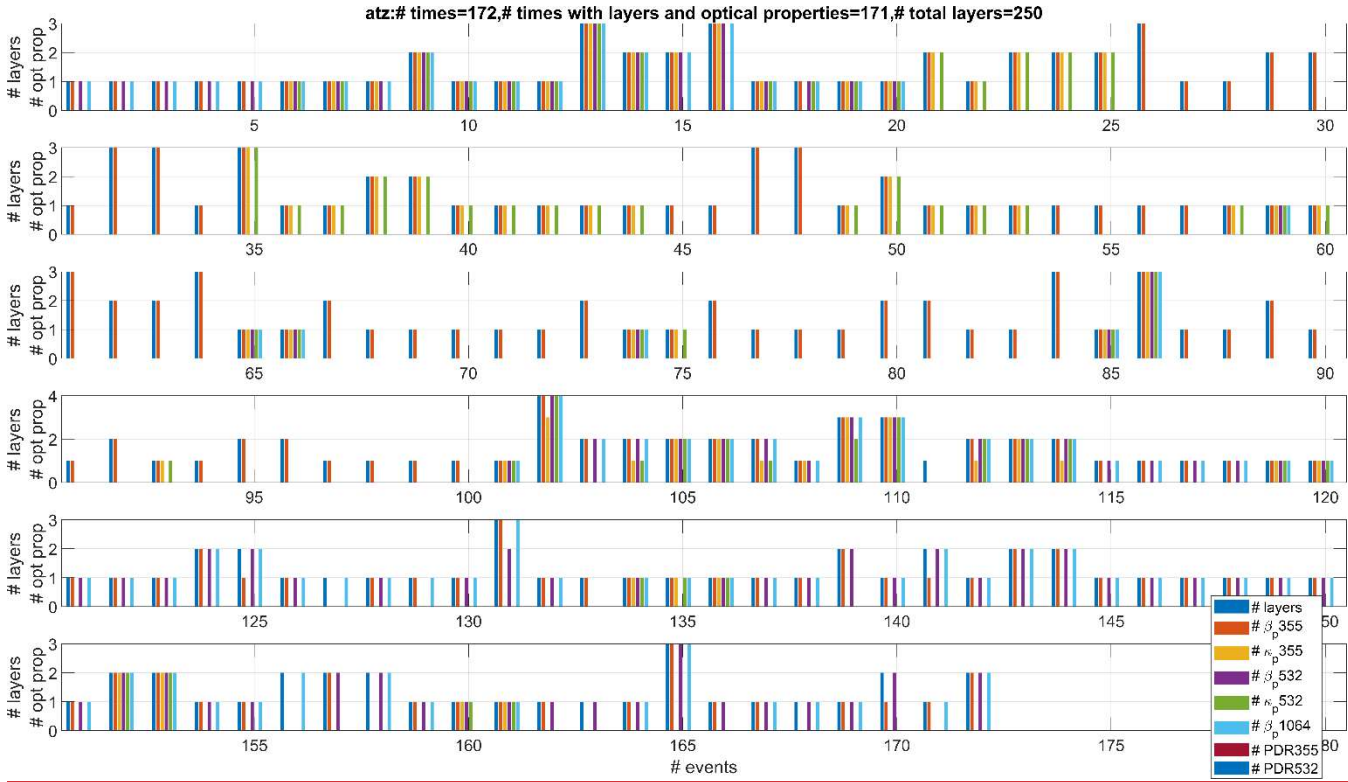


**Figure S2.** The number of times (events) when the layers were evaluated and the corresponding number of optical properties available in the layer. Example for the Athens station (“atz”). Layers have a biomass burning origin (fire source). For event 111 it was not feasible to determine any optical property.

### 34. Intensive parameters in literature

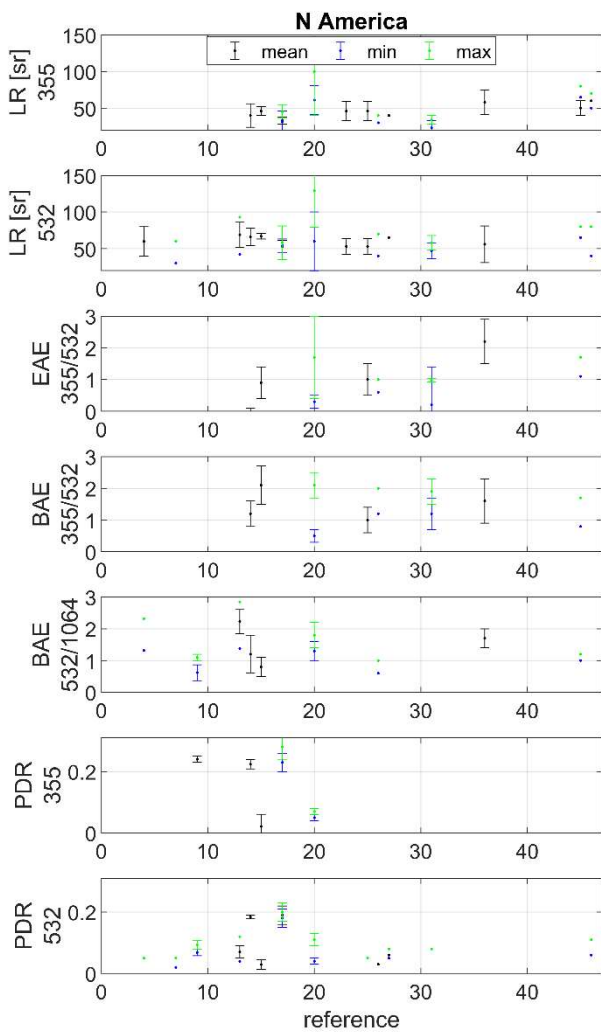
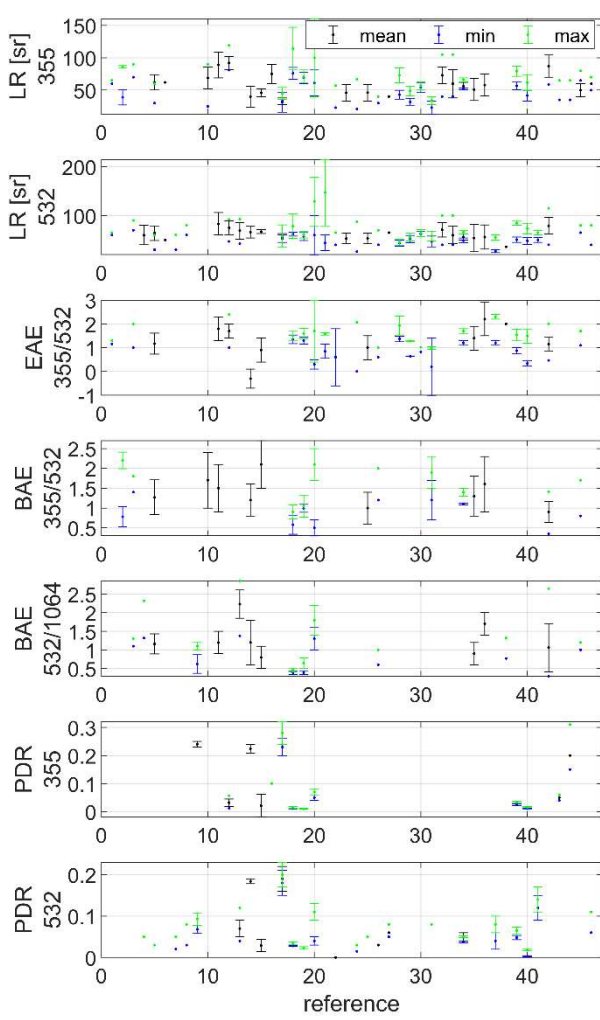


**Figure S34.** Intensive parameters for biomass burning, as reported in literature. The reference number corresponds to the references in Table S42.

**Table S34.** Values of the intensive parameters found in literature for biomass burning.

variable/ref	1	2	3	4	5	6	7	8	9	10	11	12	13	14	15	16	17	18	19	20	21	22	23	24	25	26	27	28	29	30	31	32	33	34	35	36	37	38	39	40	41	42	43	44	45	46	
LB355																																															
mean	62	62																																													
mearter		12																																													
min	60	39	70	30																																											
max	65	86	90	60																																											
maxter		2																																													
LB52																																															
mean	60	64	50																																												
mearter		20	15																																												
min	60	70	30	60																																											
max	65	90	60	60																																											
maxter																																															
EAE																																															
mean	1.17																																														
mearter		0.44																																													
min	1.16	1																																													
minter																																															
max	1.3	2																																													
maxter																																															
BAE32/355																																															
mean	1.27																																														
mearter		0.44																																													
min	0.78	14																																													
minter		0.25																																													
max	2.2	18																																													
maxter		0.21																																													
BAE094/52																																															
mean	1.16																																														
mearter		0.27																																													
min	1.1	132																																													
minter																																															
max	1.3	232																																													
maxter																																															
PDR355																																															
mean	24																																														
mearter		1																																													
min		12																																													
minter																																															
max	5.7																																														
maxter																																															
PDR32																																															
mean																																															
mearter																																															
min	2	3	68																																												
minter			1																																												
max	5	3	893																																												
maxter			15																																												
fresh (V/V <sub>2500</sub> )	0	1	0	1	1	1	0	1	1	1	1	1	1	1	1	1	1	1	1	1	1	1	1	1	1	1	1	1	1	1	1	1	1	1	1	1	1	1	1	1	1	1	1	1	1	1	1

**Table S42. References for biomass burning intensive parameters**

1. Alados-Arboledas, L., D. Müller, J. L. Guerrero-Rascado, F. Navas-Guzmán, D. Pérez-Ramírez, and F. J. Olmo, Optical and microphysical properties of fresh biomass burning aerosol retrieved by Raman lidar, and star-and sun-photometry, *Geophys. Res. Lett.*, 38, L01807, doi:10.1029/2010GL045999, 2011.
- 5 2. Amiridis, V., D. S. Balis, E. Giannakaki, A. Stohl, S. Kazadzis, M. E. Koukouli, and P. Zanis, Optical characteristics of biomass burning aerosols over Southeastern Europe determined from UV-Raman lidar measurements, *Atmos. Chem. Phys.*, 9, 2431–2440, 2009, [www.atmos-chem-phys.net/9/2431/2009/](http://www.atmos-chem-phys.net/9/2431/2009/).
- 10 3. Amiridis, V., C. Zerefos, S. Kazadzis, E. Gerasopoulos, K. Eleftheratos, M. Vrekoussis, A. Stohl, R.E. Mamouri, P. Kokkalis, A. Papayannis, K. Eleftheriadis, E. Diapouli, I. Keramitsoglou, C. Kontoes, V. Kotroni, K. Lagouvardos, E. Marinou, E. Giannakaki, E. Kostopoulou, C. Giannakopoulos, A. Richter, J.P. Burrows, N. Mihalopoulos, Impact of the 2009 Attica wild fires on the air quality in urban Athens, *Atmos. Environ.*, 46, 536-544, doi:10.1016/j.atmosenv.2011.07.056, 2012.
- 15 4. Ancellet, G., J. Pelon, J. Totems, P. Chazette, A. Bazzueau, M. Sicard, T. Di Iorio, F. Dulac, and M. Mallet, Long-range transport and mixing of aerosol sources during the 2013 North American biomass burning episode: analysis of multiple lidar observations in the western Mediterranean basin, *Atmos. Chem. Phys.*, 16, 4725–4742, doi:10.5194/acp-16-4725-2016, 2016.
- 5 5. Baars, H., A. Ansmann, D. Althausen, R. Engelmann, B. Heese, D. Müller, P. Artaxo, M. Paixao, T. Pauliquevis, and R. Souza, Aerosol profiling with lidar in the Amazon Basin during the wet and dry season, *J. Geophys. Res.*, 117, D21201, doi:10.1029/2012JD018338, 2012.
- 20 6. Balis, D. S., V. Amiridis, C. Zerefos, E. Gerasopoulos, M. Andreae, P. Zanis, A. Kazantzidis, S. Kazadzis, A. Papayannis, Raman lidar and sunphotometric measurements of aerosol optical properties over Thessaloniki, Greece during a biomass burning episode, *Atmos. Environ.*, 37, 4529-4538, doi:10.1016/S1352-2310(03)00581-8, 2003.
- 25 7. Burton, S. P., R. A. Ferrare, C. A. Hostetler, J. W. Hair, R. R. Rogers, M. D. Obland, C. F. Butler, A. L. Cook, D. B. Harper, and K. D. Froyd, Aerosol classification using airborne High Spectral Resolution Lidar measurements – methodology and examples, *Atmos. Meas. Tech.*, 5, 73–98, doi:10.5194/amt-5-73-2012, 2012.
8. Burton, S. P., R. A. Ferrare, C. A. Hostetler, J. W. Hair, R. R. Rogers, M. D. Obland, C. F. Butler, A. L. Cook, D. B. Harper, and K. D. Froyd, Aerosol classification using airborne High Spectral Resolution Lidar measurements – methodology and examples, *Atmos. Meas. Tech.*, 5, 73–98, doi:10.5194/amt-5-73-2012, 2012.
- 30 9. Burton, S. P., J. W. Hair, M. Kahnert, R. A. Ferrare, C. A. Hostetler, A. L. Cook, D. B. Harper, T. A. Berkoff, S. T. Seaman, J. E. Collins, M. A. Fenn, and R. R. Rogers, Observations of the spectral dependence of linear particle depolarization ratio of aerosols using NASA Langley airborne High Spectral Resolution Lidar, *Atmos. Chem. Phys.*, 15, 13453–13473, doi:10.5194/acp-15-13453-2015, 2015.

10. Giannakaki, E., D. S. Balis, V. Amiridis, and C. Zerefos, Optical properties of different aerosol types: seven years of combined Raman-elastic backscatter lidar measurements in Thessaloniki, Greece, *Atmos. Meas. Tech.*, 3, 569–578, doi:10.5194/amt-3-569-2010, 2010.

5 11. Giannakaki, E., A. Pfüller, K. Korhonen, T. Mielonen, L. Laakso, V. Vakkari, H. Baars, R. Engelmann, J. P. Beukes, P. G. Van Zyl, M. Josipovic, P. Tiitta, K. Chiloane, S. Piketh, H. Lihavainen, K. E. J. Lehtinen, and M. Komppula, One year of Raman lidar observations of free-tropospheric aerosol layers over South Africa, *Atmos. Chem. Phys.*, 15, 5429–5442, doi:10.5194/acp-15-5429-2015, 2015.

10 12. Giannakaki, E., P. G. van Zyl, D. Müller, D. Balis, and M. Komppula, Optical and microphysical characterization of aerosol layers over South Africa by means of multi-wavelength depolarization and Raman lidar measurements, *Atmos. Chem. Phys.*, 16, 8109–8123, doi:10.5194/acp-16-8109-2016, 2016.

15 13. Groß, S., M. Esselborn, B. Weinzierl, M. Wirth, A. Fix, and A. Petzold, Aerosol classification by airborne high spectral resolution lidar Observations, *Atmos. Chem. Phys.*, 13, 2487–2505, doi:10.5194/acp-13-2487-2013, 2013.

14. Haarig, M., Ansmann, A., Baars, H., Jimenez, C., Veselovskii, I., Engelmann, R., and Althausen, D.: Depolarization and lidar ratios at 355, 532, and 1064 nm and microphysical properties of aged tropospheric and stratospheric Canadian wildfire smoke, *Atmos. Chem. Phys.*, 18, 11847–11861, <https://doi.org/10.5194/acp-18-11847-2018>, 2018.

15 15. Haarig, M., Ansmann, A., Baars, H., Jimenez, C., Veselovskii, I., Engelmann, R., and Althausen, D.: Depolarization and lidar ratios at 355, 532, and 1064 nm and microphysical properties of aged tropospheric and stratospheric Canadian wildfire smoke, *Atmos. Chem. Phys.*, 18, 11847–11861, <https://doi.org/10.5194/acp-18-11847-2018>, 2018.

20 16. Heese, B., and M. Wiegner, Vertical aerosol profiles from Raman polarization lidar observations during the dry season AMMA field campaign, *J. Geophys. Res.*, 113, D00C11, doi:10.1029/2007JD009487, 2008.

17. Hu, Q., P. Goloub, I. Veselovskii, J.-A. Bravo Aranda, I. Popovici, T. Podvin, M. Haeffelin, A. Lopatin, C. Pietras, X. Huang, B. Torres, and C. Chen, A study of long-range transported smoke aerosols in the Upper Troposphere/Lower Stratosphere, *Atmos. Chem. Phys. Discuss.*, <https://doi.org/10.5194/acp-2018-655>, 2018.

25 18. Janicka, L., I. S. Stachlewska, Properties of biomass burning aerosol mixtures derived at fine temporal and spatial scales from Raman lidar measurements: Part I optical properties, *Atmos. Chem. Phys. Discuss.*, <https://doi.org/10.5194/acp-2019-207>, 2019.

19. Janicka, L., I. S. Stachlewska, Properties of biomass burning aerosol mixtures derived at fine temporal and spatial scales from Raman lidar measurements: Part I optical properties, *Atmos. Chem. Phys. Discuss.*, <https://doi.org/10.5194/acp-2019-207>, 2019.

30 20. Janicka, L., I. S. Stachlewska, I. Veselovskii, H. Baars, Temporal variations in optical and microphysical properties of mineral dust and biomass burning aerosol derived from daytime Raman lidar observations over Warsaw, Poland, *Atmos. Environ.*, 169, 162–174, <http://dx.doi.org/10.1016/j.atmosenv.2017.09.022>, 2017.

21. Mariano, G.L., F.J.S. Lopes, M.P.P.M. Jorge, E. Landulfo, Assessment of biomass burnings activity with the synergy of sunphotometric and LIDAR measurements in São Paulo, Brazil, *Atmos. Res.*, 98, 486-499, doi:[10.1016/j.atmosres.2010.08.025](https://doi.org/10.1016/j.atmosres.2010.08.025), 2010.

5 22. Mattis, I., A. Ansmann, U. Wandinger, and D. Müller, Unexpectedly high aerosol load in the free troposphere over central Europe in spring//summer 2003, *G.R.L.*, 30, 2178, doi:[10.1029/2003GL018442](https://doi.org/10.1029/2003GL018442), 2003.

10 23. Mattis, I., D. Müller, A. Ansmann, U. Wandinger, J. Preißler, P. Seifert, and M. Tesche, Ten years of multiwavelength Raman lidar observations of free-tropospheric aerosol layers over central Europe: Geometrical properties and annual cycle, *J. Geophys. Res.*, 113, D20202, doi:[10.1029/2007JD009636](https://doi.org/10.1029/2007JD009636), 2008.

15 24. Müller, D., I. Mattis, U. Wandinger, A. Ansmann, D. Althausen, and A. Stohl, Raman lidar observations of aged Siberian and Canadian forest fire smoke in the free troposphere over Germany in 2003: Microphysical particle characterization, *J. Geophys. Res.*, 110, D17201, doi:[10.1029/2004JD005756](https://doi.org/10.1029/2004JD005756), 2005.

25 25. Müller, D., A. Ansmann, I. Mattis, M. Tesche, U. Wandinger, D. Althausen, and G. Pisani, Aerosol-type-dependent lidar ratios observed with Raman lidar, *J. Geophys. Res.*, 112, D16202, doi:[10.1029/2006JD008292](https://doi.org/10.1029/2006JD008292), 2007.

30 26. Müller, D., A. Kolgotin, I. Mattis, A. Petzold, and A. Stohl, Vertical profiles of microphysical particle properties derived from inversion with two-dimensional regularization of multiwavelength Raman lidar data: experiment, *Appl. Opt.*, 50, 2069-2079, 2011.

27. Murayama, T., D. Müller, K. Wada, A. Shimizu, M. Sekiguchi, and T. Tsukamoto, Characterization of Asian dust and Siberian smoke with multiwavelength Raman lidar over Tokyo, Japan in spring 2003, *Geophys. Res. Lett.*, 31, L23103, doi:[10.1029/2004GL021105](https://doi.org/10.1029/2004GL021105), 2004.

28. Nicolae, D., A. Nemuc, D. Müller, C. Talianu, J. Vasilescu, L. Belegante, and A. Kolgotin, Characterization of fresh and aged biomass burning events using multiwavelength Raman lidar and mass spectrometry, *J. Geophys. Res. Atmos.*, 118, 2956–2965, doi:[10.1002/jgrd.50324](https://doi.org/10.1002/jgrd.50324), 2013.

29. Nicolae, D., A. Nemuc, D. Müller, C. Talianu, J. Vasilescu, L. Belegante, and A. Kolgotin, Characterization of fresh and aged biomass burning events using multiwavelength Raman lidar and mass spectrometry, *J. Geophys. Res. Atmos.*, 118, 2956–2965, doi:[10.1002/jgrd.50324](https://doi.org/10.1002/jgrd.50324), 2013.

30. Noh, Y. M., D. Müller, D. H. Shin, H. Lee, J. S. Jung, K. H. Lee, M. Cribb, Z. Li, Y. J. Kim, Optical and microphysical properties of severe haze and smoke aerosol measured by integrated remote sensing techniques in Gwangju, Korea, *Atmos. Environ.*, 879–888, doi:[10.1016/j.atmosenv.2008.10.058](https://doi.org/10.1016/j.atmosenv.2008.10.058), 2009.

31. Ortiz-Amezcua, P., J. L. Guerrero-Rascado, M. J. Granados-Muñoz, J. A. Benavent-Oltra, C. Böckmann, S. Samaras, I. S. Stachlewska, Ł. Janicka, H. Baars, S. Bohlmann, and L. Alados-Arboledas, Microphysical characterization of long-range transported biomass burning particles from North America at three EARLINET stations, *Atmos. Chem. Phys.*, 17, 5931–5946, doi:[10.5194/acp-17-5931-2017](https://doi.org/10.5194/acp-17-5931-2017), 2017.

32. Mylonaki, M., A. Papayannis, R. Mamouri, A. Argyrouli, P. Kokkalis, G. Tsaknakis and O. Soupiona, Aerosol optical properties variability during biomass burning events observed by the EOLE-AIAS depolarization lidars over Athens, Greece (2007-2016), 28<sup>th</sup> ILRC, Bucharest, Romania (2017).

5 33. Mylonaki, M., A. Papayannis, R. Mamouri, A. Argyrouli, P. Kokkalis, G. Tsaknakis and O. Soupiona, Aerosol optical properties variability during biomass burning events observed by the EOLE-AIAS depolarization lidars over Athens, Greece (2007-2016), 28<sup>th</sup> ILRC, Bucharest, Romania (2017).

10 34. Nepomuceno Pereira, S., J. Preißler, J. L. Guerrero-Rascado, A. M. Silva, and F. Wagner, Forest Fire Smoke Layers Observed in the Free Troposphere over Portugal with a Multiwavelength Raman Lidar: Optical and Microphysical Properties, *Scientific World, Journal*, 2014, Article ID 421838, 11 pages, <http://dx.doi.org/10.1155/2014/421838>. 2014.

35. Preißler, J., F. Wagner, J. L. Guerrero-Rascado, and A. M. Silva, Two years of free-tropospheric aerosol layers observed over Portugal by lidar, *J. GEOPHYS. RES.*, 118, 3676–3686, doi:10.1002/jgrd.50350, 2013.

15 36. Preißler, J., F. Wagner, J. L. Guerrero-Rascado, and A. M. Silva, Two years of free-tropospheric aerosol layers observed over Portugal by lidar, *J. GEOPHYS. RES.*, 118, 3676–3686, doi:10.1002/jgrd.50350, 2013.

37. Samaras, S., D. Nicolae, C. Böckmann, J. Vasilescu, I. Binietoglou, L. Labzovskii, F. Toanca, A. Papayannis, Using Raman-lidar-based regularized microphysical retrievals and Aerosol Mass Spectrometer measurements for the characterization of biomass burning aerosols, *Journal of Computational Physics* 299, 156–174, <http://dx.doi.org/10.1016/j.jcp.2015.0>, 2015.

20 38. Sicard, M., M Mallet, D. Garc'ia-Vizca'ino, A Comer'on, F Rocadenbosch, P Dubuisson and C Mu'noz-Porcar, Intense dust and extremely fresh biomass burning outbreak in Barcelona, Spain: characterization of their optical properties and estimation of their direct radiative forcing, *Environ. Res. Lett.* 7, 034016 (6pp), doi:10.1088/1748-9326/7/3/034016, 2012.

25 39. Stachlewska, I. S., O. Zawadzka and R. Engelmann, Effect of HeatWave Conditions on Aerosol Optical Properties Derived from Satellite and Ground-Based Remote Sensing over Poland, *Remote Sens.*, 9, 1199; doi:10.3390/rs9111199, 2017.

40. Stachlewska, I. S., M. Samson, O. Zawadzka , K. M. Harenda, L. Janicka, P. Poczta, D. Szczepanik, B. Heese, D. Wang, K. Borek, E. Tetoni, E. Proestakis, N. Siomos, A. Nemuc, B. H. Chojnicki, K. M. Markowicz, A. Pietruczuk, A. Szkop, D. Althausen, k. Stebel , D. Schuettemeyer and C. Zehner, Modification of Local Urban Aerosol Properties by Long-Range Transport of Biomass Burning Aerosol, *Remote Sens.*, 10, 412; doi:10.3390/rs10030412, 2018.

30 41. Sugimoto, N., B. Tatarov, A. Shimizu, I. Matsui, and T. Nishizawa, Optical Characteristics of Forest-Fire Smoke Observed with Two-Wavelength Mie-Scattering Lidars and a High-Spectral-Resolution Lidar over Japan, *SOLA*, 6, 093–096, doi:10.2151/sola.2010-024, 2010.

42. Tesche, M., D. Müller, S. Gross, A. Ansmann, D. Althausen, V. Freudenthaler, B. Weinzierl, A. Veira and A. Petzold, Optical and microphysical properties of smoke over Cape Verde inferred from multiwavelength lidar measurements, *Tellus*, 63B, 677–694, DOI: 10.1111/j.1600-0889.2011.00549.x, 2011.

5 43. Vaughan, G., A. P. Draude, H. M. A. Ricketts, D. M. Schultz, M. Adam, J. Sugier, and D. P. Wareing, Transport of Canadian forest fire smoke over the UK as observed by lidar, *Atmos. Chem. Phys.*, 18, 11375–11388, <https://doi.org/10.5194/acp-18-11375-2018>, 2018.

10 44. Vaughan, G., A. P. Draude, H. M. A. Ricketts, D. M. Schultz, M. Adam, J. Sugier, and D. P. Wareing, Transport of Canadian forest fire smoke over the UK as observed by lidar, *Atmos. Chem. Phys.*, 18, 11375–11388, <https://doi.org/10.5194/acp-18-11375-2018>, 2018.

45. Veselovskii, I., D. N Whiteman, M. Korenskiy, A. Suvorina, A. Kolgotin, A. Lyapustin, Y. Wang, M. Chin, H. Bian, T. L. Kucsera, D. Pérez-Ramírez, and B. Holben, Characterization of forest fire smoke event near Washington, DC in summer 2013 with multi-wavelength lidar, *Atmos. Chem. Phys.*, 15, 1647–1660, doi:10.5194/acp-15-1647-2015, 2015.

15 46. Wandinger, U., D. Müller, C. Bo"ckmann, D. Althausen, V. Matthias, J. Bo"senberg, V. Weiß, M. Fiebig, M. Wendisch, A. Stohl, and A. Ansmann, Optical and microphysical characterization of biomassburning and industrial-pollution aerosols from multiwavelength lidar and aircraft measurements, *J. Geophys. Res.*, 107, NO. D21, 8125, doi:10.1029/2000JD000202, 2002.

20

25

30

35

**4 Example number of layers selected and corresponding intensive optical parameters available for each layer**

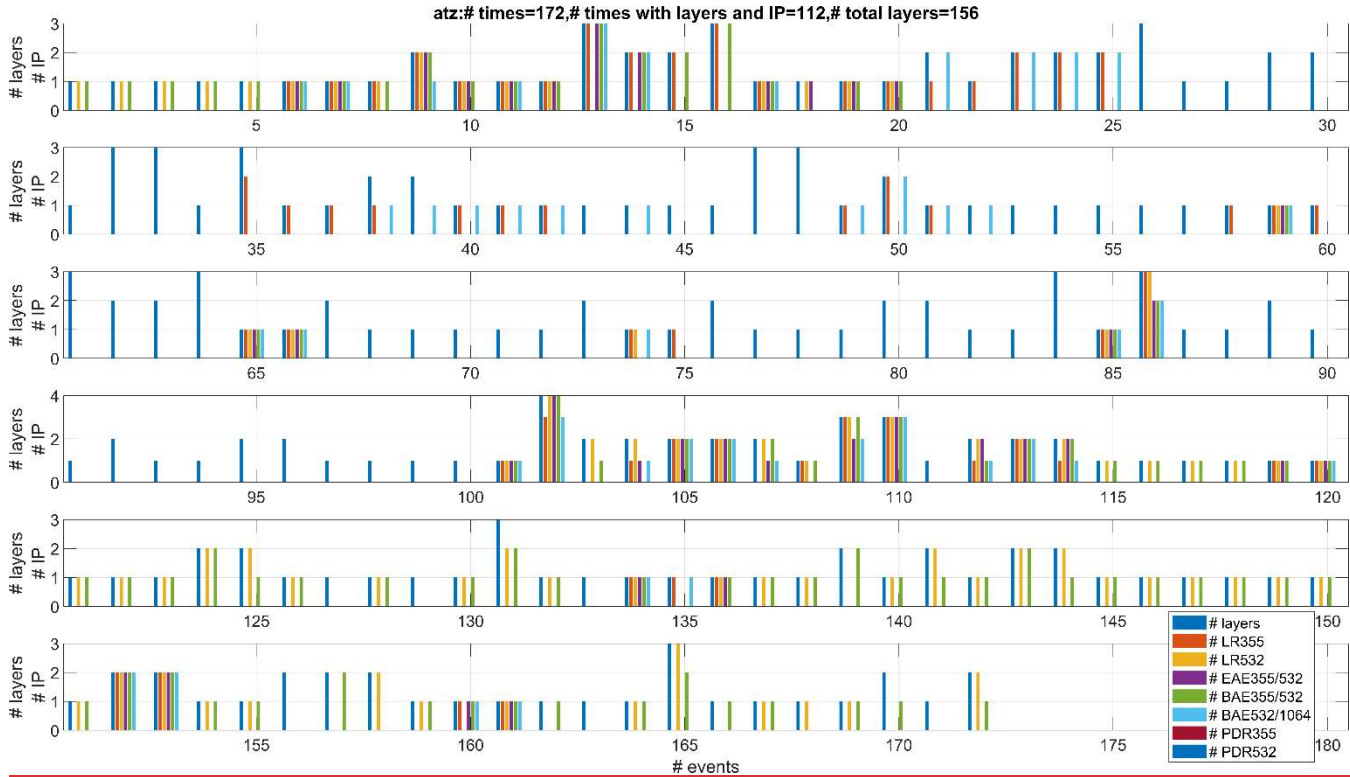


Figure S4. The number of times (events) when the layers were evaluated and the corresponding number of intensive parameters available in the layer. Example for Athens station (“atz”). Layers have a biomass burning origin (fire source).

5

10

15

17